Numerical Studies of Plasma Turbulence for Comparison With Measurements at TJ-K

Dissertation zur Erlangung des Doktorgrades
der Mathematisch-Naturwissenschaftlichen Fakultät
der Christian-Albrechts-Universität
zu Kiel

vorgelegt von
Sven Niedner

Kiel
2002

Referent/-in:	Prof. Dr. U. Stroth
Koreferent/-in:	Prof. Dr. T. Klinger
Tag der mündlichen Prüfung:	16. Juli 2002
Zum Druck genehmigt:	Kiel, den 6. Januar 2003

Der Dekan

Zusammenfassung

Turbulenz ist eines der großen ungelösten Probleme der modernen Physik. Außer in Flüssigkeiten treten turbulente Fluktuationen auch in Plasmen auf; in Fusionexperimenten sind sie für den größten Teil der Teilchen- und Energieverluste verantwortlich. Die Theorie der Plasmaturbulenz hat durch die Fusionsforschung in den letzten Jahren große Fortschritte gemacht. Parallel arbeitende Supercomputer bieten darüber hinaus die Möglichkeit, Plasmaturbulenz unter realistischen Bedingungen zu simulieren. Ein systematischer Vergleich dieser Simulationsrechnungen mit experimentellen Befunden ist nun notwendig. Mit der vorliegenden Arbeit soll eine erste Grundlage für einen solchen Vergleich geschaffen werden. Hierzu wurde ein für Fusionsplasmen entwickelter Turbulenzcode an die Verhältnisse des Niedertemperaturplasmas im Kieler Torsatron TJ-K angepasst. Die Simulation enthält die im vorliegenden Parameterbereich dominierenden Instabilitäten, die Driftinstabilität und die MHD-Austauschinstabilität. Die relative Wichtigkeit der beiden Instabilitäten für das vorliegende Plasma wurde numerisch untersucht. Zur Reduktion der umfangreichen raum-zeitlichen Daten wurden statistische Methoden entwickelt, die in dieser Form auch auf experimentelle Daten anwendbar sind. Anhand dieser Methoden wurden die charakteristischen Merkmale der beiden Instabilitäten herausgearbeitet. Die radiale Strukturgröße, die Kreuzphase zwischen Dichte und Potential sowie die Transportspektren erwiesen sich als am besten geeignet zur Bestimmung der Intensität der einzelnen Instabilitäten. Durch Variation der Plasmaparameter wurde das Skalierungsverhalten dieser Merkmale untersucht. Nach diesen Untersuchungen ist für den Parameterbereich, in dem TJ-K betrieben wird, Driftwellenturbulenz zu erwarten. Es wurden konkrete Messungen vorgeschlagen, die zu einer Überprüfung der Vorhersagen und der zugrundeliegenden Modelle durchgeführt werden können.

Contents

1 Introduction

Turbulence has been a challenging topic in science for several hundred years. As early as around 1500 Leonardo formulated his observation of turbulent flows. Since then much work has been put into the understanding of turbulence, mainly in fluids. The Kolmogorov-41 theory [20] on self similarity properties of the fluctuations is one of the few analytical turbulence theories.

In plasma physics, the investigation of turbulence is motivated by the interest in nuclear fusion as an energy source. The most promising approach to nuclear fusion in a laboratory is the magnetic confinement of a high-temperature plasma. In such a plasma, turbulent transport is one of the major mechanisms for energy losses [68, 65]. The understanding of the underlying turbulence is therefore of great importance. However, the dynamic of the ionized gases is more complex than that of a neutral fluid. As the electron and ion fluids move, their mobility is restrained by the magnetic field, and their fluctuations give rise to fluctuations in the electric and magnetic fields, which in return affect the turbulent flows. The analytical treatment of the plasma turbulence is only possible in extremely simplified cases [75]. The numerical solution of the fluid equations is the most promising approach to the understanding of plasma turbulence. Due to improved computer performance, numerical simulations have undergone significant progress over the last years. The simulation of turbulence in large plasma volumes [45] and in realistic magnetic geometry [33] has become possible. Testing the physical models behind the simulation requires a comparison of the microscopic structure of the resulting turbulence with experimental measurements. This work addresses the numerical part of such a comparison and computes turbulence properties for the torsatron TJ-K. For the numerical simulation, the DALF3 simulation code is used [60].

In fusion plasmas, the experimental diagnostic of the fluctuating quantities is handicapped by high temperatures. Measurements have are mostly restricted to the scrape-off layer beyond the last closed flux surface [6, 44, 74]. A low temperature laboratory plasma confined in a magnetic field comparable to fusion experiments provides a good starting point for detailed turbulence measurements and comparison to numerical results. The torsatron TJ-K [38], operated by our group in Kiel, is such an experiment. In contrast to the situation in fusion devices, in this experiment the entire plasma is accessible for Langmuir probes, which are the main diagnostics in our case. This makes TJ-K the ideal tool for the study of the spatial structure of turbulent fluctuations. Aim of this work is to investigate

how the low temperature laboratory plasma compares to a fusion device. This is done by analyzing the normalized parameters that characterize the turbulence in the analytical equations. These equations are solved numerically in the simulation. As the normalized parameters appear to be of similar magnitude in the edge of a fusion plasma and in TJ-K, these two experimental situations are expected to show similar turbulent fluctuations.

Low temperature plasmas can be used as a testing bed for the precision of simulation codes. If the simulation correctly predicts the turbulence in TJ-K, the results can be transferred to fusion edge turbulence. The main goal of this work within comparison of theory and experiment is to obtain numerical predictions from the simulation code that can be verified in the experiment.

In the examined parameter regime the turbulence is driven by two micro-instabilities. The *MHD interchange instability* is the plasma physics analogon of the Rayleigh-Bénard instability in fluid dynamics. It is driven by a background pressure gradient and activated by magnetic field curvature. The *drift instability* is a result of the anisotropic dynamics of charged particles in magnetic fields. Decreased mobility of the charges in the direction of the magnetic field leads to the drift instability. A two fluid model for the plasma fluctuations in a three dimensional geometry is presented [61].

TJ-K is a torsatron, belonging to the stellarator family, with pronounced local shear [2] in its magnetic field configuration. It has been shown [70] that local shear leads to a damping of the turbulent fluctuations. In order to analyze the impact of local magnetic shear on the turbulence, the code was extended to include these effects.

The stochastic nature of the turbulence restricts data analysis to statistical properties of the turbulent fluctuations. The common approach to statistical properties is by doing time series analysis. Allowing for spatially resolved measurements, TJ-K greatly enhances the diagnostic possibilities. Various statistical space-time properties are assessed with respect to their applicability to TJ-K and their capability to detect signatures of the micro-instabilities in the turbulent fluctuations.

The statistical properties of the plasma turbulence strongly depend on the (normalized) parameter set. However, a reliable predetermination of these parameters is not possible for the experiment. A solution to this problem is to study parameter ranges. Scalings of the turbulence properties provide a more reliable indication for the accuracy of the theoretical predications. Since the normalized parameters determine the importance of the micro-instabilities, a sweep can isolate . Based on the simulation results at different normalized parameters, changes in the turbulence micro-structure are investigated. In the experiment, similar parameter sweeps can be realized by the careful adjustment of the physical plasma parameters.

The thesis is organized as follows: After this short outline, the second chapter

gives a brief introduction into the concept of magnetic plasma confinement and explains the possible origins of turbulent transport. In the third chapter, a model for the plasma dynamics is developed and a normalized equation set for turbulence simulation is derived. In chapter four, the experimental setup of the torsatron TJ-K is outlined, and the preconditions of a successful simulation of the plasma are discussed. A separate section is dedicated to the modeling of local magnetic shear. General turbulence theories on fluid and plasma dynamics are discussed in chapter five. Chapter six describes various data analysis tools, suitable for experiment–theory comparison, and their ability to detect the signatures of the micro-instabilities. In chapter seven the impact of the normalized parameters on the turbulent fluctuations is investigated by means of scaling studies. Chapter eight summarizes the most important findings obtained in this work.

2 Transport in magnetized plasmas

The goal of this chapter is an introduction to magnetic plasma confinement, and to the problems that arise from transport phenomena. Turbulent fluctuations are presented as a source of radial transport and experimental and theoretical findings are briefly discussed.

2.1 Magnetic confinement

Good magnetic confinement is the biggest challenge for nuclear fusion in a laboratory. As temperatures in a fusion plasma reach up to several keV, the direct contact of the plasma with the vessel must be avoided. Usually a magnetic field is used for the confinement. The charged particles (ions and electrons) gyrate around the field lines and can only move along $\mathbf{B}$. So closed field lines are necessary for magnetic confinement.

2.1.1 Simple magnetized torus

A purely toroidal configuration fulfills this requirement (Fig. 2.1, left). It can be characterized by the major radius R and the minor radius a. The minor radius a and the angles θ and ϕ are used to refer to positions in the torus. The toroidal angle ϕ is associated with the major radius and the poloidal angle θ with the minor radius (see Fig. 2.1). Due to the gyration of the electrons and ions, they react to forces by drifts of the respective guiding center. One example is the curvature drift, resulting from magnetic field curvature, defined by the curvature radius $\mathbf{R}_\kappa$,

$$\mathbf{v}_\kappa = (2E_\parallel + E_\perp)\frac{\mathbf{R}_\kappa \times \mathbf{B}}{qR_\kappa^2 B^2} \tag{2.1}$$

Here, $E_\parallel$ and $E_\perp$ are the parallel and perpendicular kinetic energy, and q is the particle charge. The curvature drift is charge-separating, i. e., it transports ions and electrons in opposite directions. Its consequence is illustrated in Fig. 2.1: the ions drift upwards, and the electrons drift down, generating a vertical electric field. The $\mathbf{E}$ field is the source of another drift, the $\mathbf{E} \times \mathbf{B}$ drift,

$$\mathbf{v}_E = \frac{\mathbf{E} \times \mathbf{B}}{B^2}\,. \tag{2.2}$$

This drift transports electrons and ions equally in the $\mathbf{E} \times \mathbf{B}$ direction, which is to the outside of the torus in Fig. 2.1. An example of an experiment with

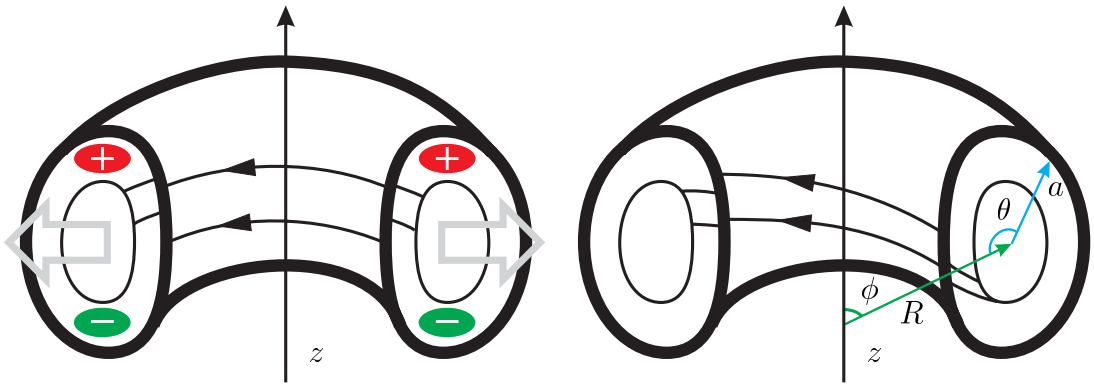

Figure 2.1 In a simple magnetized torus (left) the curvature drift produces a vertical electric field, leading to plasma loss. A toroidal twist of the field lines (right) can compensate this effect.

such a magnetic field structure is the TEDDI device in Kiel [23]. Its field setup is called *simple magnetized torus* (SMT). In this geometry, the $\mathbf{E} \times \mathbf{B}$ drift leads to a continuous loss of plasma and prevents an equilibrium state. A twist (rotational transform) of the magnetic field (see Fig. 2.1, right) allows for a reduction of the charges via Pfirsch-Schlüter currents along the magnetic field lines. It stabilizes the plasma and is the most common field geometry for magnetic confinement.

Once a stable magnetic field configuration is achieved, flux surfaces can be defined. They are determined by field lines that include a constant magnetic flux. On a flux surface, the value of the magnetic field $|\mathbf{B}|$ varies with $1/R$. The part of the flux surface that lies on the inside of the torus is the high-field side (HFS), and the outer side is the low field side (LFS). The isobars of the confined plasma fall on the magnetic flux surface. This state is in the MHD equilibrium. There are various approaches to generate twisted toroidal magnetic field lines with an MHD stable plasma.

2.1.2 The tokamak

In a tokamak, external coils produce only a toroidal magnetic field, like in a SMT. Since the toroidal field alone does not provide a stable confinement, the twisting of the field line (called safety factor q) is generated by a circular plasma current in the toroidal direction. It is driven by an ohmic transformer. A horizontal coil compensates the vertical magnetic field generated by the plasma current. A disadvantage of this setup is that a tokamak can only be operated in pulses during which the current in the transformer is continuously increased. When no further increase is possible, the operation has to be interrupted and restarted. For more details on tokamaks see Ref. [71].

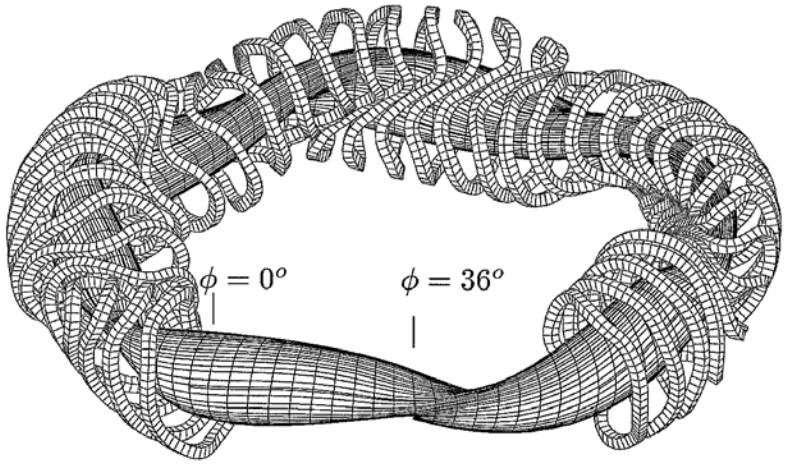

Figure 2.2 Coil arrangement for the stellarator Wendelstein 7X (Greifswald) [51]; it has a five period toroidal symmetry. Inside the coils a flux surface is shown [66].

2.1.3 The stellarator

In a stellarator, the toroidally twisted magnetic field is generated by a complex arrangement of magnetical coils [63, 64]. As an example of a modern device, Fig. 2.2 shows the coil arrangement for the Wendelstein 7X stellarator. The rotational transform is about $\iota = 1/q = 0.8...1.2$, and the magnetic field is about 2.5 Tesla. As an externally driven, toroidal current is not required to obtain magnetic confinement, steady-state operation is possible for stellarators. This is a major advantage for a fusion power plant. The field structure of the stellarator is very complicated compared to the tokamak field and lacks its symmetry. This leads to additional "neoclassical" effects (see next section) and makes the analytical treatment of the geometry more complicated. Stellarators are discussed in detail in Ref. [69].

2.1.4 The torsatron TJ-K

The flux surface structure of TJ-K is shown in Fig. 2.3. TJ-K is a torsatron and is part of the stellarator family, so no toroidal current is needed. It has one helical coil that winds around the vessel six times in the poloidal direction. Horizontal coils compensate the vertical magnetic field generated by the helical current. The resulting $\mathbf{B}$ field is very "bumpy" and inhomogeneous compared to e. g. Wendelstein 7X (Fig. 2.2). The geometry of the magnetic field in TJ-K can be varied via the ratio of the currents in the coils [38].

Typical parameters for several typical fusion experiments are compiled in Tab. 2.1.

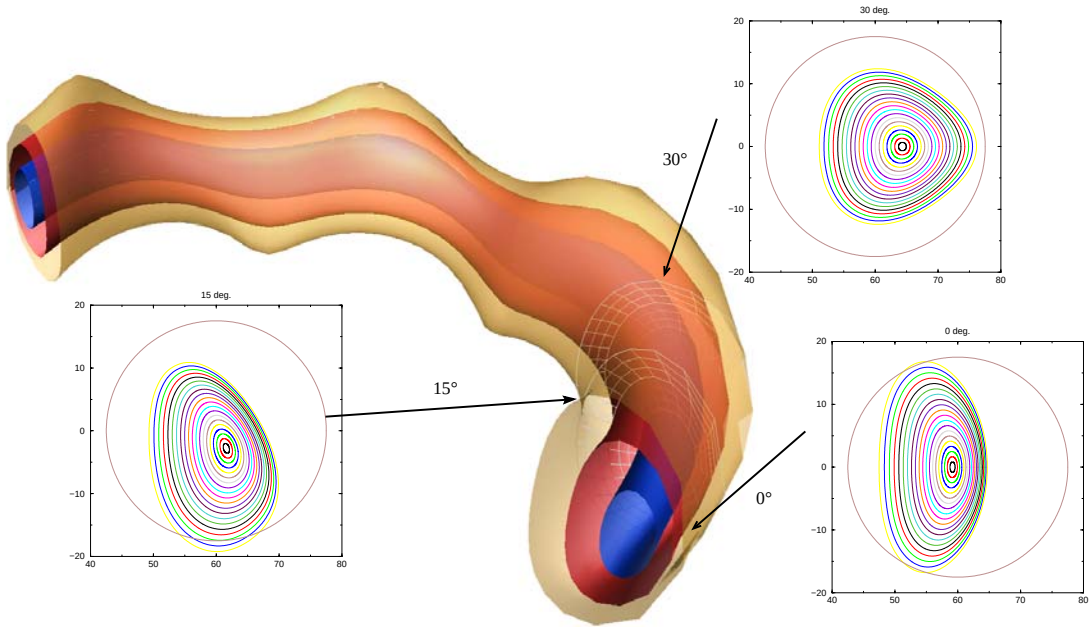

Figure 2.3 Flux surfaces of TJ-K; it has a sixfold toroidal symmetry and the rotational transform is $\iota = 0.2 - 0.3$. The poloidal structure of the flux surfaces is shown for the toroidal angles $\phi = 0°, 15°, 30°$.

Table 2.1 Typical parameters from different experiments with toroidally confined plasmas. Traditionally, the twist of the field line is given by the safety factor q for tokamaks and as the rotational transform ι for stellarators.

Experiment	R	a	Rot. transf.	B_0	T	P
ASDEX-U, core (IPP)	1.5 m	0.4 m	$q = 3$	3.9 T	10 keV	27 MW
Wendelstein 7AS (IPP)	2 m	0.2 m	$\iota = 0.3$	3.0 T	5 keV	5 MW
Wendelstein 7X (IPP)	5.5 m	0.5 m	$\iota = 1$	3.0 T	10 keV	20 MW
TJ-K (CIEMAT)	0.6 m	0.1 m	$\iota = 0.3$	0.6 T	1 keV	1 MW
TJ1-U (Kiel)	0.6 m	0.1 m	$\iota = 0.3$	0.3 T	30 eV	3 kW

Traditionally, the rotational transform is given in q for tokamaks and as ι for stellarators. The fusion-oriented experiments are all operated at high magnetic field B_0 and high plasma temperatures T. The plasma heating is done by microwaves at the electron or ion cyclotron resonance, by neutral particle injection or by ohmic heating with the current drive (in the tokamak). TJ-K in Kiel is operated with a low-temperature laboratory plasma. The plasma generation is done using a radio frequency (RF) heating, exciting a Helicon wave in the plasma [38]. The low temperature regime of the TJ-K plasma is advantageous for the diagnostics. In chapter 4 it is be shown that under certain conditions the measurements in TJ-K are nonetheless representative for fusion experiments.

2.2 Radial transport

The previous section gave a brief outline of the problems concerning the global stability of a plasma setup. Once closed flux surfaces have been achieved, there are still micro-instabilities left that cause serious problems for the confinement. The subsequently listed effects lead to radial transport of particles and energy:

2.2.1 Classical transport

The thermal motion of the plasma particles leads to collisions with frequency $1/\tau_c$. At each collision, a displacement of the colliding particles takes place. The average length of this displacement can be estimated by the Larmor radius of the particle, ϱ_i or ϱ_e, respectively. From the theory of random walk, one obtains a diffusion coefficient $D = \varrho^2/2\tau_c$. The related transport is referred to as *classical transport*. In a toroidal plasma, the classical transport is enhanced by the Pfirsch-Schlüter factor, $D_{PS} = (1+q^2)D$ [66]. At a typical value of $q = 3$ this factor enhances the transport by one order of magnitude.

2.2.2 Neoclassical transport

The magnetic field strength $|\mathbf{B}|$ varies along a magnetic field line. A charged, gyrating particle has a magnetic moment $\mu = mv_\perp^2/2B$ interacting with the magnetic field. Some particles moving along a magnetic field line are reflected because of conservation of the associated adiabatic invariant. Such a field configuration is called a *magnetic mirror*. As a consequence, the ratio of trapped to passing particles is

$$\frac{n_t}{n_p} = \sqrt{\frac{2a}{R}}\,. \tag{2.3}$$

In TJ-K, 66 % of the particles are trapped in magnetic mirrors. For the trapped particles the curvature drifts do not cancel out and their trajectories eventually

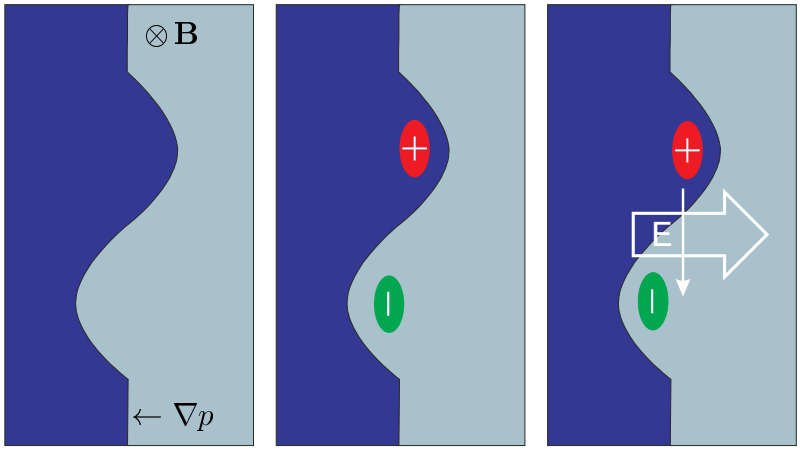

Figure 2.4 To a density perturbation, the electron fluid reacts in the direction parallel to the magnetic field (out of the figure) and leaves behind a positive charge excess. As a result, the $\mathbf{E} \times \mathbf{B}$ drift propagates the wave downward in the electron diamagnetic direction. When the parallel electron motion is hindered, the drift wave becomes unstable.

end outside the plasma. This results in a loss of particles via this trajectories. The transport which is due to this phenomenon is called the *neoclassical* transport.

2.2.3 Turbulent transport

In a magnetized plasma, the experimentally determined transport exceeds the theoretical predictions from classical and neoclassical theories [68, 65]. Furthermore, fluctuations of the plasma parameters have been observed [44] since the early years of fusion research. These are due to micro-instabilities: The plasma reacts to gradients with turbulent fluctuations. The energy source for these fluctuations is the pressure (density or temperature) gradient, and from the fluctuations results radial transport. The transport that is due to turbulent fluctuations is called *anomalous transport*. The anomalous transport that is observed in the experiments exceeds the neoclassical transport by two orders of magnitude [68]. The understanding of the turbulence is therefore an important step towards improved plasma confinement.

The present work focuses on the dynamics of turbulence. In the next section, we will outline two basic mechanisms behind the turbulent transport.

2.2.4 Drift instability

The drift wave is a perturbation in the plasma density, traveling along an isobar with diamagnetic velocity. A profound discussion of linear drift wave theory can

be found in Ref. [13]. The main feature of the drift wave is its three dimensional structure; it requires the direction along the magnetic field line for its dynamics. The left part of Fig. 2.4 shows a density perturbation in the plasma. High density plasma is on the left-hand-side of the figure, and the magnetic field points into it. Under the assumption that T = const., a density perturbation is always a pressure perturbation. We assume a pressure perturbation that is localized in the radial, poloidal and in the parallel direction. The reaction of the plasma to the resulting gradient ∇p is an acceleration of the particles. As the movement perpendicular to the magnetic field lines is restrained, the plasma can only respond to the gradient parallel to $\mathbf{B}$. The parallel dynamics of the drift wave is illustrated in Fig. 2.5. However, electrons and ions do not travel at the same speed: due to their smaller mass, the electrons move faster than the ions. When the electrons stream out of an density excess, they leave a positive space charge behind. In return, electrons filling up a density minimum bring in negative charges. Density and potential perturbation are in phase. The potential perturbation results in an electric field along $\mathbf{B}$, leading to an $\mathbf{E} \times \mathbf{B}$ drift (2.2). This drift is maximal where the density perturbation is zero, and it is zero where the density perturbation (and the potential perturbation as well) are extreme. Consequently, the $\mathbf{E} \times \mathbf{B}$ motion of the plasma results in a displacement of the perturbation along the isobar, but not in radial transport: The amount of density transported down the gradient is exactly compensated by the opposite effect on the other side of the maximum. In this simple linear picture, the drift wave is marginally stable and propagates

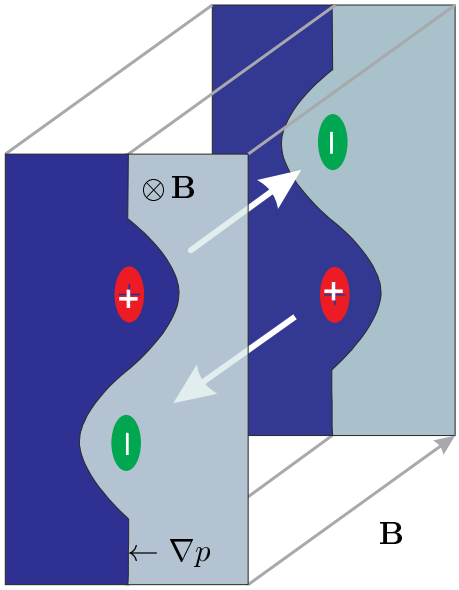

Figure 2.5 The parallel dynamics of the drift wave is due to currents along the magnetic field lines. This leads to a finite $k_{||}$ along $\mathbf{B}$.

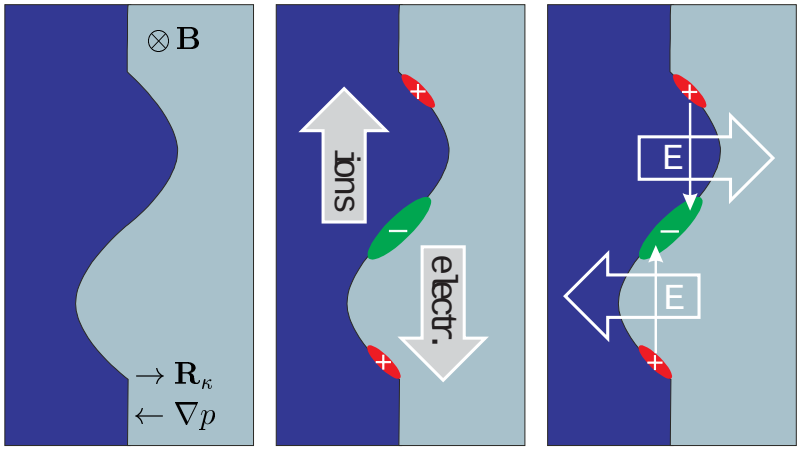

Figure 2.6 A density perturbation is subjected to the charge-separating curvature drift. An electric field is created, leading to $\mathbf{E} \times \mathbf{B}$ convection of the density. The situation is shown for the low-field side of the plasma; on the high-field side the $\mathbf{E} \times \mathbf{B}$ drift is stabilizing.

downwards with the electron diamagnetic velocity.

The hidden assumption in this simplified picture is that the electrons can react infinitely fast to the density perturbation, a situation which is referred to as "adiabatic electrons". When the electrons cannot move freely in the parallel direction, density and potential perturbations get out of phase. The net transport is no longer zero, and the drift wave becomes unstable as it extracts energy from the background gradient. The amplitude growth of the perturbation gives rise to nonlinear effects such as mode interactions and leads to turbulent fluctuations. Simple model equations for the study of drift wave turbulence are the Hasegawa-Mima equation [27] for adiabatic electron dynamics, and the Hasegawa-Wakatani equations [28] for resistive drift waves.

2.2.5 The MHD interchange instability

MHD stands for magneto-hydrodynamics, already suggesting that this instability has an equivalent in fluid dynamics. In a plasma it is only active in the presence of field line curvature. The working of the instability is sketched in Fig. 2.6. The density gradient is in the horizontal direction, and the magnetic field points into the figure. Additionally the curvature radius $\mathbf{R}_\kappa$ is shown in the direction of the gradient. The curvature of the magnetic field lines results from the toroidal field geometry and varies with the poloidal position. Here we show a plasma element at the low field side. As the density perturbation is subjected to the curvature drift (2.1), the ions stream up and the electrons stream down. The density perturbation now becomes a potential perturbation in the formerly neutral plasma: Since more

electrons move in from the high pressure region into the low pressure region than electrons move out of the low pressure region into the high pressure region, a (negative) charge excess is created. Half a wavelength away, a positive space charge is created in a respective way. The charges lead to an $\mathbf{E}$ field and an $\mathbf{E} \times \mathbf{B}$ drift. In contrast to the drift wave, the phase shift between density and potential perturbation is $\pi/2$, and the extrema of the initial density perturbation are convected most. The perturbation is unstable and grows. The fluid analogon of the MHD interchange instability is the Rayleigh-Bénard instability of a fluid with a mass density gradient subjected to a gravitational force. In the MHD interchange instability the role of the gravity is replaced by the effect of the curvature.

Since the curvature radius $\mathbf{R}_\kappa$ has parallel directions with respect to ∇p on the high field side of a toroidal experiment, the resulting $\mathbf{E} \times \mathbf{B}$ movement goes in the opposite direction and stabilizes the initial density perturbation. Although the curvature is the reason for the MHD instability, it cannot act as an energy source. In fact, the fluctuation energy comes from the background gradient, and the curvature drift deforms the density and potential fluctuations in a way that ∇p can act as an energy source. In contrast to drift waves, which have a parallel wave number $k_{||} \neq 0$ in the presence of a parallel resistivity, the MHD mode has $k_{||} = 0$ as the model does not include the parallel dynamics. The growth rates for MHD interchange modes differ for the HFS and the LFS, and in a realistic setup one expects different fluctuation amplitudes on the HFS and LFS. This effect is referred to as a "ballooning structure", and the modes are called ballooning modes. The interaction of the MHD interchange instability and the drift wave is called *resistive ballooning mode* (RBM) turbulence [25].

The simple pictures in this chapter are useful for understanding of the mechanisms behind the plasma instabilities. In the plasmas that are subject to this study, however, they cannot be observed in these simple linear forms. The fluctuation amplitudes reach a level where nonlinear effects become most important. This means that in addition to the stability of modes the nonlinear energy transfer between them has to be considered. This is not possible in simple pictures or analytical calculations. The simulation of the model equations on a computer has proven an important tool for the research in plasma turbulence. In the next chapter, the dynamical mechanisms described here are used to set up model equations.

3 Modeling the dynamics

This chapter describes the construction of the model equations that DALF3 uses for the simulation of plasma turbulence. It is not a derivation from first principles or from a well-known set of equations (for such an approach see [62]). The model will be constructed describing the dynamics of an electron fluid and an ion fluid in interaction. For the applicability of a fluid model, the energy distribution has to be Maxwellian with only small perturbations. This is generally justified in a collisional plasma. The characteristic length scale of the fluctuations has to be larger than the ion gyro radius.

3.1 Drift Ordering

The plasma is confined in a magnetic field. We choose our coordinate grid to follow the magnetic field lines in the z-direction. We assume a constant background pressure gradient ∇p_0 in the $-x$ direction. The detailed setup of the flux tube coordinate system is subject to the next chapter. Pressure fluctuations $\tilde{p}$ are small compared to the background gradient,

$$\frac{\tilde{n}}{n} \approx \frac{e\tilde{\phi}}{T} \approx \frac{\tilde{p}}{p} \ll 1 \tag{3.1}$$

but their gradient is comparable to the background gradient, $\nabla\tilde{p} \approx \nabla p_0$. This is called the "mixing level argument". The assumption of small fluctuation amplitudes and comparable gradients leads to fluctuations with a typical length $L_{fl.}$ that is small compared to the background gradient length $L_\perp = p/\nabla p$,

$$\frac{L_{fl.}}{L_\perp} \ll 1\,. \tag{3.2}$$

To allow a separation between parallel and perpendicular scales, drift ordering is introduced. The perpendicular wave numbers of the fluctuations are large compared to the parallel wave numbers, i. e. $k_\perp \gg k_\parallel$. The same holds for the gradients in the wave picture, $\nabla_\perp \gg \nabla_\parallel$.[1] The typical perpendicular length scale of the fluctuation is given by the drift scale ϱ_s,

$$\varrho_s = c\sqrt{M_i T_e}/eB = \frac{c_s}{\omega_{ci}}\,. \tag{3.3}$$

1 The direct comparison of operators is not defined. When we use this formulation we refer to the results of these operators.

In this equation, T_e denotes the electron temperature, M_i the ion mass and c is the speed of light. Formally, this is equivalent to the ion gyro radius at electron temperature. The sound speed is denoted by c_s in this equation.

$$c_s = c\sqrt{\frac{T_e}{M_i}} \tag{3.4}$$

Since we assumed fluctuations smaller than the typical gradient length, we demand that $\varrho_s \ll L_\perp$. From the definition of the drift scale follows that the fluctuation frequency is low compared to the ion cyclotron frequency ω_{ci}. We define the parameter $\delta = \varrho_s / L_\perp$, and it is

$$\delta = \frac{\varrho_s}{L_\perp} \approx \frac{\omega}{\omega_{ci}} \approx \frac{\tilde{n}}{n_0} \approx \frac{e\tilde{\phi}}{T_e} \ll 1\,. \tag{3.5}$$

This is called the "drift ordering". It will enter the normalization performed in section 3.4. From the drift ordering results the separation of the parallel and perpendicular dynamics, the electrostatic limit of the perpendicular electric field and that perturbations of the electric field are only in the perpendicular direction [62].

3.2 Main model

The plasma turbulence model can be described in three equations. The conservation of particles (written in terms of the density, n) is

$$D_t = (\partial_t + \mathbf{v}\cdot\nabla)n \;\; = \;\; 0\,, \tag{3.6}$$

and the conservation of charge is

$$\nabla\cdot\mathbf{J} \;\; = \;\; 0\,, \tag{3.7}$$

marked by the fact that the electric current $\mathbf{J}$ is divergence-free. By fixing these two conservation laws, the model explicitly excludes effects due to the generation (by ionization) and the loss (by recombination) of particles and charge. The third equation is the momentum balance for the electrons. Due to the presence of the magnetic field, we assume that the electron movement in the perpendicular direction is due to drifts only, and hence focus on the parallel component of the electron momentum,

$$\nabla_\parallel(nT) - ne\nabla_\parallel\phi - \frac{ne}{c}\partial_t A_\parallel - nm_e\nu_e(v_\parallel - u_\parallel) = nm_e D_t v_\parallel\,. \tag{3.8}$$

The forces in this equations are due to a pressure gradient $\nabla_\parallel(nT)$, electrostatic $(\nabla_\parallel\phi)$ and electromagnetic forces $(\partial_t A_\parallel)$. The latter denotes the time derivative

of the parallel component of the vector potential, describing magnetic induction. The next term is the electric resistivity due to collisions, with ν_e being the collision rate. The variables $v_\parallel$ and $u_\parallel$ are the parallel components of the electron and ion velocity, respectively. The last term is the acceleration in the comoving reference frame. The symbol $D_t = (\partial_t + \mathbf{v}_E \cdot \nabla)$ is used as a first order approximation for the convective derivative. Velocities other than the $\mathbf{E} \times \mathbf{B}$ velocity are dropped.

The collision rate ν_e is computed as

$$\nu_e = 8\pi \ln\Lambda \frac{n_e e^2 c}{3\sqrt{3 m_e T_e^3}} \tag{3.9}$$

Here, e, T_e and m_e are the electron charge, temperature and mass and $\ln\Lambda \approx 17$ is the Coulomb logarithm.

3.2.1 Perpendicular dynamics

In the next steps the drift motion is obtained from Eqs. (3.6, 3.7) by separating the parallel and perpendicular directions of motion. For this we rewrite the divergence of the current as

$$\nabla_\parallel J_\parallel + \nabla_\perp ne\mathbf{v}_\perp = 0\,. \tag{3.10}$$

We express the parallel current by the electron motion only (thus neglecting the parallel ion motion, which is much slower than the electron motion). Next, we assume that the perpendicular dynamics is drift-only, and set it to the sum of the $\mathbf{E} \times \mathbf{B}$ drift, the polarization drift and the diamagnetic drift, $\mathbf{v} = \mathbf{v}_E + \mathbf{v}_{pol} + \mathbf{v}_*$. Since the $\mathbf{E} \times \mathbf{B}$ drift moves ions and electrons equally and does not transport charge, it is dropped. Therefore, only $\mathbf{v}_{pol}$ and $\mathbf{v}_*$ are taken into account:

$$\nabla_\parallel J_\parallel + \nabla_\perp ne(\mathbf{v}_{pol} + \mathbf{v}_*) = 0\,. \tag{3.11}$$

Inserting the drifts

$$\mathbf{v}_{pol} = \frac{M_i c^2}{eB^2}(\partial_t + \mathbf{v}_E \cdot \nabla)\nabla_\perp \phi \tag{3.12}$$

$$\mathbf{v}_* = -\frac{cT}{neB^2}\mathbf{B} \times \nabla_\perp n \tag{3.13}$$

yields

$$-\frac{M_i c^2}{eB^2}\nabla_\perp ne(\partial_t + \mathbf{v}_E \cdot \nabla)\nabla_\perp \phi + \frac{cT}{neB^2}\nabla_\perp ne\mathbf{B} \times \nabla_\perp n = \nabla_\parallel J_\parallel\,. \tag{3.14}$$

All variables not acted on by a operator are now treated as constants. This allows to rearrange the differential operators

$$-ne\frac{M_i c^2}{eB^2}(\partial_t + \mathbf{v}_E \cdot \nabla)\nabla_\perp^2 \phi + \frac{c}{B^2}\nabla_\perp \mathbf{B} \times \nabla_\perp p = \nabla_\parallel J_\parallel\,. \tag{3.15}$$

Additionally, $p = nT$ has been used. Eq. 3.15 is the first of the simulation equations. Now we separate Eq. (3.6) into parallel and perpendicular components and set the $\mathbf{E} \times \mathbf{B}$ velocity $\mathbf{v}_E$ as the perpendicular velocity,

$$\partial_t n + \nabla_\perp n \mathbf{v}_E + \gamma \nabla_\parallel n v_\parallel = 0\,, \tag{3.16}$$

with γ as the adiabaticity coefficient. We now expand the perpendicular part into $n\nabla_\perp \mathbf{v}_E + \mathbf{v}_E \nabla_\perp n$. The second term is the diamagnetic drift. Under the assumption of cold ions, $T_i \ll T_e$, the diamagnetic term is much smaller than the $\mathbf{E} \times \mathbf{B}$ drift. For the mass transport, it is dropped, neglecting the electron mass. It is kept for the transport of charge, however, because the $\mathbf{E} \times \mathbf{B}$ drift does not transport charge and the diamagnetic drift remains as the only mechanism to move charge around. The resulting equation reduces to

$$(\partial_t + \mathbf{v}_E \cdot \nabla_\perp) n + \gamma \nabla_\parallel n v_\parallel = 0\,. \tag{3.17}$$

3.2.2 Parallel dynamics

We now express $v_\parallel$ by the parallel current, because $J_\parallel = ne(u_\parallel - v_\parallel)$, and obtain

$$(\partial_t + \mathbf{v}_E \cdot \nabla_\perp) n + \gamma \nabla_\parallel u - \gamma \frac{1}{ne} J_\parallel = 0\,. \tag{3.18}$$

This is the second of the three equations that are used for the simulation; it describes the time evolution of the density. The third and last one is parallel momentum balance (3.8),

$$\nabla_\parallel p - ne\nabla_\parallel \phi - \frac{ne}{c}\partial_t A_\parallel - n m_e \nu_e (v_\parallel - u_\parallel) - n m_e D_t v_\parallel - = 0. \tag{3.19}$$

For an actual computation, these equation do not suffice. A relation between electric and magnetic fluctuations is needed. Such relations can be derived from the Maxwell equations,

$$E_\parallel = -\frac{\partial A_\parallel}{\partial t} - \nabla_\parallel \phi\,, \tag{3.20}$$

$$E_\perp = -\nabla_\perp \phi\,, \tag{3.21}$$

$$-\nabla^2 A_\parallel = \frac{4\pi}{c} J_\parallel\,. \tag{3.22}$$

Together with the Maxwell equations, Eqs. (3.15, 3.18, 3.22) form the system that is numerically solved and whose results are analyzed in the present work. However, for the actual numerical solution it is advantageous to transform the variables in a normalized form, and hereby reducing the number of numerical factors to a minimum. Before this step is discussed, we will briefly outline the dynamics of the resulting system.

3.3 Turbulence dynamics

The model that has been build around the conservation laws and the anisotropy resulting from the magnetic field has some interesting properties. Its further discussion is helpful for the understanding of plasma turbulence. The most prominent point is the drastic difference between the motion in the parallel and perpendicular direction. In the parallel direction, the system is able to respond to gradients along the magnetic field lines. This leads to a fast compensation of parallel inhomgenieties in the fluctuations, and consequently the structures that form in the turbulence are elongated in the parallel direction. Using a wave picture, one would say that only low $k_{\|}$-modes are present.

The perpendicular dynamics is different in that gradients cannot be compensated. The plasma reacts with drifts: A potential gradient in the perpendicular plane convects density around with $\mathbf{v}_E$, and a density gradient transports charge via the diamagnetic drift $\mathbf{v}_*$. The direction of the drift is perpendicular to the gradient. Linear drift wave theory (see section 2.2.4) teaches us that the parallel mobility of the electrons is a precondition for the stability of the plasma against density perturbations. Unhindered parallel electron motion leads to adiabaticity of density and potential fluctuations. When these fluctuations are in phase no plasma is transported down the gradient and the fluctuations cannot grow. However, from the parallel momentum equation (3.8) one can see that the parallel current can be hindered by electric resistivity (due to collisions) and magnetic induction. Consequently, it is expected that an increase in these two factors leads to more violent turbulence, since it provides a coupling that allows the turbulence to extract energy from the background.

The role of the polarization drift in Eq. (3.15) (which is due to time-evolving electric fields) becomes clear by looking at the characteristic time evolution of a density perturbation: When a density perturbation is created by the fluctuations, parallel currents flow. These currents are carried by the electrons (the ions are too heavy to respond sufficiently fast). The result is that the density perturbation is overlayed by a positive excess charge. On its creation, the ions act via the polarization drift and leave the density perturbation in a spiraling motion. This is shown in Fig. 3.1.

Not only the drift instability is present in the code, but also the MHD interchange instability. In the initial discussion of the MHD interchange instability in section 2.2.5, the curvature drift has been presented as the destabilizing agent. However, the curvature drift is a particle drift which vanishes when one passes to a fluid picture. In the fluid dynamics context, the role of the curvature drift is taken over by the diamagnetic drift. This coupling is contained in Eq. (3.15) in the form $\nabla_\perp \mathbf{B} \times \nabla_\perp p$, yielding different results for different locations along a magnetic field line. The effect either attracts or repulses charge ($\nabla_\perp^2 \phi$) at the places where the density perturbation changes sign ($\nabla_\perp n \propto \nabla_\perp p$ is maximal). In

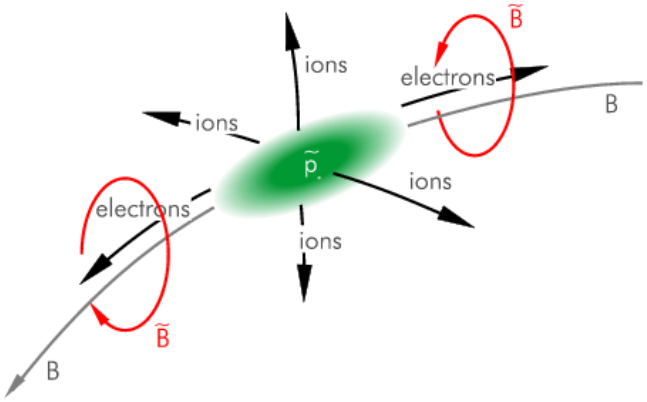

Figure 3.1 As a reaction to a pressure perturbation, electrons stream out along the **B** field, exciting a torsional Alfvén wave. The changing electric field then degrades the density perturbation by moving the ions out in a spiraling motion.

a wave picture, this is the case where the charge fluctuation crosses the zero line, leading to the characteristic phase shift of $\pi/2$ for MHD interchange turbulence.

An important feature of the equation system is the coupling between the drift wave and fluctuations of the magnetic field via the parallel currents. Electromagnetic waves are excited that propagate along the magnetic field lines, providing a strong coupling between density and potential fluctuations. These Alfvén waves propagate with the Alfvén speed $v_A = B/(4\pi n M_i)^{1/2}$ which is higher than the typical velocities in the turbulence given by the sound speed c_s (c. f. Eq. (3.4)).

In TJ-K, the sound speed is 2.2×10^4 m/s, the Alfvén speed is 1.3×10^6 m/s. Fig. 3.1 illustrates how the parallel Alfvén wave and the polarization drift result from a density perturbation [57].

Although much of the argumentation in this section is based on linear theory, it is important to note that the turbulent results from the code are essentially due to nonlinear effects. Linear stability considerations can be used as a guideline, but in the nonlinear regime the energy flux between wave numbers due to three-mode interactions becomes much more important. The result is that the fluctuation energy is distributed over the wave numbers not according to their linear stability properties, but via nonlinear energy transfer. The consequences of such an energy transfer are discussed in section 5.1. The main result is a power spectrum that exhibits a self similar scaling law.

3.3.1 Resistive ballooning

The model behind the simulation includes both resistive effects (drift waves) and curvature driven MHD interchange modes. The interaction of resistive effects and interchange turbulence is often referred to as "resistive ballooning" [76, 77]. Such

Table 3.1 Definition of normalized parameters in DALF3. The drift parameter $\delta = \varrho_s/L_\perp$ is folded into the normalizations.

	Variable		Normalization
Potential	$\tilde{\phi}$ [V]	$\leftarrow$	$\delta^{-1}\, e\phi/T$
Density	$\tilde{n}$ [m^{-3}]	$\leftarrow$	$\delta^{-1}\, n/n_0$
Current	$J_\parallel$ [A]	$\leftarrow$	$\delta^{-1}\, nec_s qR/L_\perp \cdot J_\parallel$
Length	l [m]	$\leftarrow$	l/ρ_s
Length $\parallel\mathbf{B}$	z [m]	$\leftarrow$	z/qR
Time	t [s]	$\leftarrow$	$t \cdot c_s/L_\perp$

a mode grows with a larger amplitude on the low field than on the high field side of the plasma due to magnetic field curvature. It generates a pressure gradient along the field line in the parallel direction. The parallel electron dynamics, including resistivity, couples this mode to a drift wave-like potential perturbation.

3.4 Normalized parameters

For the simulation of the plasma, a transition is performed to dimensionless, normalized variables. Tab. 3.1 shows a translation from physical into normalized variables. Under the normalization, the differential operators are also rewritten, $\nabla_\perp \to \varrho_s \nabla_\perp$, $\nabla_\parallel \to qR\nabla_\parallel$ and $\partial_t \to (L_\perp/c_s)\partial_t$. As the temperature is constant, $\tilde{p} = T\tilde{n}$. With these normalizations, the equations (3.15, 3.18, 3.22) read

$$D_t \nabla_\perp^2 \tilde{\phi} = \nabla_\parallel \tilde{J}_\parallel \tag{3.23}$$

$$\hat{\beta}\partial_t \tilde{A}_\parallel + \hat{\mu} D_t \tilde{J}_\parallel = \nabla_\parallel(\tilde{p} - \tilde{\phi}) - \hat{\mu}\hat{\nu}\tilde{J}_\parallel \tag{3.24}$$

$$D_t \tilde{p} = \gamma \nabla_\parallel \tilde{J}_\parallel - \gamma \nabla_\parallel u_\parallel \tag{3.25}$$

$$\tilde{J}_\parallel = -\nabla_\perp^2 \tilde{A}_\parallel \,. \tag{3.26}$$

The dynamics of the normalized variables is determined by the normalized parameters, $(\hat{\beta}, \hat{\nu}, \hat{\mu})$. The normalization yields:

$$\hat{\beta} = \frac{4\pi p_e}{B^2}\left(\frac{qR}{L_\perp}\right)^2 \tag{3.27}$$

$$\hat{\nu} = \nu_e \frac{L_\perp}{c_s} \tag{3.28}$$

$$\hat{\mu} = \frac{m_e}{m_i}\left(\frac{qR}{L_\perp}\right)^2 \tag{3.29}$$

$$\varepsilon_s = \left(\frac{qR}{L_\perp}\right) \tag{3.30}$$

The parameter $\hat{\nu}$ is the collision frequency ν_e (3.9), normalized to the sound speed c_s (3.4) and the perpendicular gradient length $L_\perp$. As we will see later, its main effect is introducing anadiabadicity in the parallel electron dynamics. $\hat{\beta}$ is the plasma beta $\beta_e = 4\pi p_e/B^2$ normalized to the geometrical properties, $(qR/L_\perp)^2$. Here, q is the safety factor, and R is the major radius of the torus. The ratio of the length scales appears here because the drift parameter δ was included in the normalization. The parameter $\hat{\mu}$ and ε_s describe ion and electron inertia in normalized units. Another important parameter for the turbulence is the drift scale (3.3). It is different from the parameters discussed above because it is not a free parameter which can be adjusted independently from the other. It acts as a scaling parameter for the size of the turbulent fluctuations. Alternatively, it can be determined by the ratio of the sound speed and the ion cyclotron frequency (3.3). As such, it indicates the distance a density perturbation typically propagates during one ion cyclotron period. An average turbulence eddie is of the size of several ϱ_s.

3.4.1 Scalings of the parameters

An important consequence of these normalizations is that the resulting turbulence obeys certain scaling laws. Most evident is the variation with the drift scale; it enters as a length scale. With some experimental efforts, it is possible to keep the normalized parameters constant, and only vary ϱ_s. That this is indeed possible will be shown in chapter 4. As a consequence, the turbulence appears "magnified" by the scaling factor ϱ_s, without changing other dynamical properties. It is evident that this prediction can nicely be compared to experimental results, but other scaling studies can also be carried out: By carefully adjusting the experimental, i. e. unnormalized plasma parameters, sweeps in one of the normalized parameters can be realized, keeping the others constant. Section 4.3.1 discusses how these experiments can be carried out in TJ-K. Such experiments are of relevance for fusion experiments, too, as it can been shown that the normalized parameters fall in the same range in TJ-K and in the edge of a fusion plasma.

The self consistency of the gradient with the fluctuation level cannot be assured as the background gradient for the turbulence is prescribed in the model. Consequently, a unrealistic short $L_\perp$ for a parameter regime leads to an overestimation of the fluctuation amplitudes. Such a systematic overestimation of the fluctuations amplitudes was also observed in a similar study [5].

3.5 Further instabilities

The DALF3 turbulence model contains a limited number of plasma instabilities, the drift instability and the MHD interchange instability. The parallel dynamics is described by sound and Alfvén waves, with electrical resistivity and magnetic

induction included. Depending on the parameter regime, however, there are several other instabilities that are not covered in the code. A recent review on the different turbulence driving mechanisms can be found in Ref. [75].

3.5.1 Temperature driven modes

A radial temperature gradient, similar to a pressure gradient, can lead to instabilities. Two mechanisms are distinguished, electron temperature gradient (ETG) and ion temperature gradient (ITG) modes. Both modes are candidates for the core of a fusion plasma, where ion and electron temperature reach up to several keV with steeper gradients. Neither the scrape-off layer nor a laboratory plasma provide sufficiently high temperature gradients.

ITG turbulence The ITG mode becomes unstable once a certain ion temperature gradient is exceeded. The mechanism that drives the ITG mode is similar to the MHD interchange instability: In a perturbation like the one in Fig. 2.6, the curvature drift (2.1) is depending on the temperature T_i. Ions in hot fluid elements experience a faster drift than in a cold one [76]. From this results the same mechanism as for the density gradient in the interchange mode. Hence again, a potential fluctuation is created, and the phase between the temperature fluctuation and the potential fluctuation is $\pi/2$. The hot fluid elements are then convected down the temperature gradient in a convective cell. This leads to a heat transfer, and energy loss in the plasma core. Since this instability is due to variations in the temperature, it can still exist when the density fluctuations are adiabatic. The coupling to the temperature gradient is provided by the curvature drift, hence the fluctuations have a ballooning structure. This means that the amplitudes are higher on the low field side of the torus.

Characteristic perpendicular length scales of the fluctuations are of the order of the ion gyro radius, $k_\perp \varrho_i \approx 1$. A discussion of ion temperature modes is found in Ref. [17].

ETG turbulence The electron temperature gradient mode has the same underlying physics. The potential perturbation is created by the temperature depending drift velocity of the electrons. The electrons move on much smaller scales, and the typical perpendicular length scales of ETG turbulence is in the order of $k_\perp \varrho_e \approx 1$.

The temperature driven instabilities only contribute significantly to the energy transport when ∇T is larger than the density gradient. Neither ITG nor ETG modes play an important role in the fusion edge and in low temperature laboratory plasma. The assumptions of cold ions and constant electron temperature that were made for the derivation of the DALF3 lead to the consequence that both

instabilities are not covered in the code. This is a reasonable assumption for the simulation of the TJ-K plasma.

3.5.2 Other effects

The DALF3 model neither includes the gyro motion of the charged particles in the magnetic field, nor kinetic effects.

Finite Larmor radius (FLR) effects The fluid approximation demands that $\varrho_i, \varrho_e \ll \varrho_s$. This is necessary to assure that the time evolution of ϕ is not smeared out by particles that do excursions out of the fluid element due to their gyration.

A special kind of simulation codes, the gyro-fluid codes, have been developed to cover these effects. In this codes, the particle orbits are represented by guiding centers [18, 4].

Kinetic effects The fluid approach is an approximation, where an infinitesimal volume element is described by the statistical properties of the particles in it. The modeling of the fluid equations requires a Maxwellian energy distribution. However, particles of different energy react differently to the magnetic field geometry, e. g. as trapped particles. Plasma heating introduces particles of higher energy into the volume element and perturbs the energy distribution. The influence of these effects cannot be covered by a fluid code, but needs a kinetic description of the plasma, where the trajectories of individual particles are computed. The statistical properties are then deduced from the particle dynamics. This sort of simulation is extremely expensive in terms of computing power and therefore rarely used. Results from such a simulation are presented in Ref. [29].

In section 4.1, the validity of the assumptions behind the neglection of these effects is discussed for the different operating regimes of TJ-K as well as for the fusion scrape-off layer.

4 The torsatron TJ-K

In this chapter, we compare two different experimental situations. It is the torsatron TJ-K, operated by our group in Kiel, and the scrape-off layer of a fusion tokamak. Albeit these two experiments have little in common, it is explained that the situations are very similar with respect to turbulence simulations. This allows one to take the measurements done at TJ-K as a benchmark for the simulation of fusion plasmas. The second part of the chapter discusses the field geometry of a stellarator, and how the local magnetic shear can be implemented in DALF3.

4.1 The scrape-off layer of a fusion experiment

The scrape-off layer (SOL) of a fusion device consists of open field lines outside the last closed flux surface. As an example we take ASDEX-upgrade at IPP, Garching, for which DALF3 was originally developed. The experiment has a major radius of $R = 1.54\,\mathrm{m}$ and a minor radius $a = 0.4\,\mathrm{m}$. The magnetic field lines are toroidally closed. In the tokamak edge, the safety factor $q = 1/\iota$ is about three. In the SOL, typical electron and ion temperatures are 150 eV, at densities $n_e = 2 \times 10^{19}\,\mathrm{m}^{-3}$. The values are much lower than the densities and temperatures in the core of the plasma. The magnetic field is about 2 T, and the device is operated with hydrogen ions. The normalized plasma parameters resulting from this setup are $\hat{\nu} = 1$, $\hat{\beta} = 0.9$ and $\hat{\mu} = 1.2$. The drift scale $\varrho_s = 0.1\,\mathrm{cm}$ is well below the gradient length $L_\perp = 5\,\mathrm{cm}$.

Turbulence diagnostic is difficult in fusion experiments because of the high temperatures and the small structures. Measurements using Langmuir probes have been possible outside the last closed flux surface [19, 6]. The difficulty of turbulence measurements beyond the last closed flux surface makes the comparison between experiment and numerical predictions a hard task.

4.2 The torsatron TJ-K

The torsatron TJ-K is a stellarator device for the magnetic confinement of a plasma in a toroidal field. It is the former TJ1-U that was build at CIEMAT, Spain. TJ1-U was operated at electron temperatures $T_e = 500\,\mathrm{eV}$, and magnetic fields up to 0.6 T. After its transfer to Kiel, it has been converted to a low-temperature laboratory plasma experiment with the fusion-oriented magnetic field geometry of

Table 4.1 Physical and normalized parameter sets for situation typical for TJ-K and the edge of fusion devices. The connection length $L_{\|}$ is 15 m, and the perpendicular gradient length $L_{\perp}$ is 5 cm. $\hat{\mu}$ is 1.2 for Hydrogen, 0.3 for Helium and 0.03 for Argon [50].

n_e/m^{-3}	T_e/eV	B_0/T	Gas	$\hat{\nu}$	$\hat{\beta}$	ϱ_s/cm	Comment
2.0×10^{19}	150	2.0	H	1	0.9	0.1	Fusion Plasma Edge
1.7×10^{18}	15	0.13	H	4	0.7	0.5	Hydrogen Reference
2.5×10^{18}	21	0.20	He	4	0.7	0.5	Helium Reference
3.6×10^{18}	25	0.20	He	4	1.0	0.5	$\hat{\beta}$-scan
2.5×10^{18}	21	0.20	He	4	0.7	0.5	
1.8×10^{18}	18	0.17	He	4	0.5	0.5	
1.1×10^{18}	14	0.15	He	4	0.3	0.3	
7.2×10^{17}	11	0.13	He	4	0.2	0.5	
3.6×10^{17}	8.0	0.11	He	4	0.1	0.5	
6.3×10^{17}	21	0.10	He	1	0.7	1.0	$\hat{\nu}$-scan
6.3×10^{17}	15	0.07	He	2	0.7	1.0	
1.3×10^{18}	18	0.12	He	3	0.7	0.7	
2.5×10^{18}	21	0.20	He	4	0.7	0.5	
1.7×10^{18}	11	0.11	H	5	0.7	0.3	
1.7×10^{18}	10	0.11	H	6	0.7	0.3	
1.7×10^{18}	8.0	0.10	H	10	0.7	0.3	
3.9×10^{18}	18	0.22	H	4	0.7	0.2	ϱ_s-scan
9.8×10^{17}	9.5	0.07	H	4	0.7	0.4	
1.7×10^{18}	18	0.14	He	4	0.7	0.6	
9.8×10^{17}	13	0.1	He	4	0.7	0.8	
6.3×10^{17}	11	0.06	He	4	0.7	1.0	
7.0×10^{17}	20	0.1	Ar	4	0.7	3.0	
2.5×10^{17}	12	0.04	Ar	4	0.7	5.0	

a torsatron. A detailed overview of technical properties of the TJ1-U experiment can be found in Ref. [1, 2]. Its operation in Kiel is described in Ref. [38, 37, 67].

The device is constructed as follows: A helical coil winds six times around a toroidal vacuum vessel with major radius $R = 60\,\mathrm{cm}$, generating a toroidal and vertical magnetic field. Horizontal coils at the top and the bottom of the vessel compensate the vertical field component and allow to shift the plasma inward and outward. Two small additional horizontal coils are available for plasma shaping. The coil geometry of TJ-K is shown in Fig. 4.1. By variation of the currents in the coils, different magnetic configurations can be achieved. The magnetic field ranges up to 0.3 T. A helicon wave heating system with $P = 3.5\,\mathrm{kW}$ is used for plasma generation. An equilibrium density profile is shown in Fig. 4.2. The isolines of the density are in good agreement with the structure of the computed flux surface. The plasma in TJ-K is hence in the state of MHD equilibrium. This is a requirement for the use of the DALF3 simulation code. TJ-K can be operated using different ion species, namely Argon, Helium and Hydrogen. Densities up to $6 \cdot 10^{18}\,\mathrm{m}^{-3}$ are achieved, and electron temperatures up to 30 eV. The ions are cold.

The data analysis techniques that are presented in chapter 6 have been designed to match the capabilities of TJ-K, where turbulence diagnostics is done by Langmuir probes. This is a major boon of operating the plasma in a low-temperature

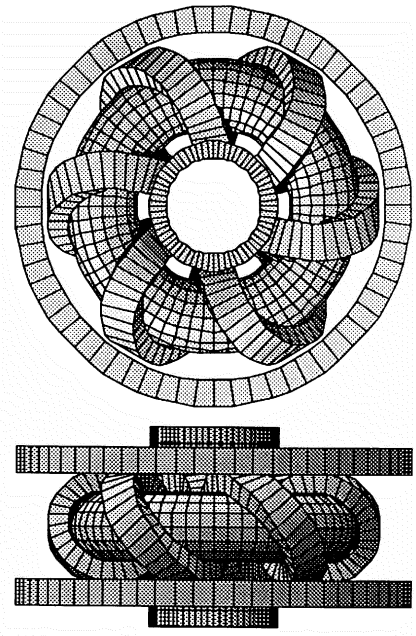

Figure 4.1 The torsatron TJ-K. Shown are the toroidal vacuum vessel, the helical and the vertical field coils.

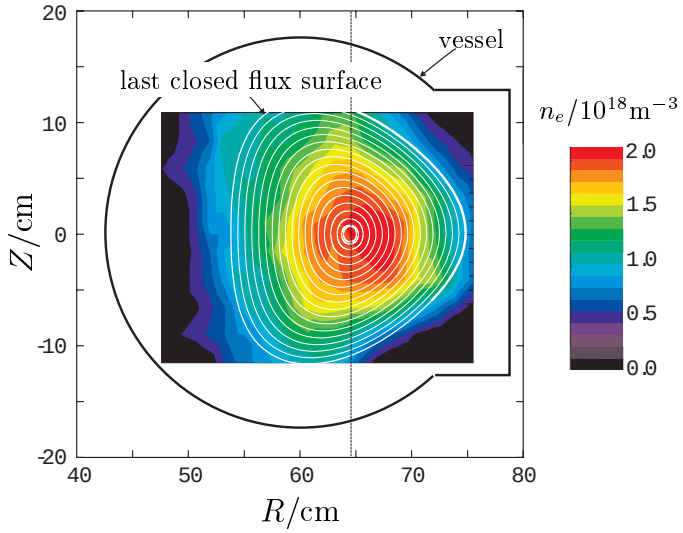

Figure 4.2 Density profile (measured by the ion saturation current) in the poloidal plane of TJ-K. The calculated flux surface structure is overlayed [41].

regime, since the measurement of the fluctuating variables is possible everywhere in the plasma. It allows for detailed comparisons between experimental findings and numerical simulations. A movable probe is used in conjunction with a fixed probe to obtain cross correlations in the poloidal plane (see section 6.3.2 for corresponding numerical results). A 1D probe array following the flux surface is under construction (see section 6.4.1 for numerical results), as well as a 2D probe array for the poloidal plane.

4.3 Applicability of DALF3 to TJ-K

In the construction of the DALF3 model equations, a number of assumptions have been made. The drift ordering demands that the drift scale ϱ_s is small against the perpendicular gradient length $L_\perp$. From the density profile, a perpendicular gradient length of 5 cm is estimated. Consequently, the condition $\varrho_s \ll L_\perp$ is fulfilled in TJ-K, with exception of very low magnetic fields below 0.05 T or Argon ions.

The poloidal circumference of the TJ-K plasma is 65 cm on average. Over this distance, the geometrical properties of the magnetic field vary strongly. It is impossible to take this into account using the flux tube metric which is used in DALF3 (cf. section 4.5). The situation in the flux tube is only representative along one particular magnetic field line, and the flux tube is assumed to be homogeneous in the perpendicular direction. Thus, turbulence features from the simulation that depend on averaged geometrical parameters, like global curvature and shear,

have to be interpreted with care. In the actual experiment, the local geometry variations will probably dominate the global ones. Turbulence features that do not rely on geometry are expected to be more robust. This problem does not arise in simulations of the tokamak plasma (cf. section 4.1) because the smaller drift scale reduces the size of the simulation area, and the larger minor radius prevents strong variations of the metric elements on these scales.

Another feature particular to stellarators has to be taken care of when DALF3 simulation results are compared to experimental measurements. It is the complicated structure of the magnetic field, where $|\mathbf{B}|$, the curvature and the local magnetic shear vary in both toroidal and poloidal direction. The effect of magnetic shear and curvature in TJ-K will be modeled in section 4.5. The variation of $|\mathbf{B}|$ leads to 66 % of the particles being "trapped" in magnetic mirrors along the field line. Other than in a tokamak, the length of the mirrors in TJ-K are not at the scale of a connection length $L_\parallel$, but between the passages of the field line at the coils. With $\iota = 1/3$ and the sixfold toroidal symmetry, the mirror length is $\iota L_\parallel/6$. The trapped particles do not contribute to the parallel conductivity of the plasma. The resistivity in the experiment will consequently be higher than the value for $\hat{\nu}$ that is computed from the normalizations.

4.3.1 TJ-K plasma parameters

Estimated optimal plasma parameters for TJ-K operated with helium gas are $n_e = 2.5 \times 10^{18}\,\mathrm{m}^{-3}$, $T_e = 21\,\mathrm{eV}$ and $B = 0.2\,\mathrm{T}$ with a drift scale $\varrho_s = 0.5\,\mathrm{cm}$. This results in normalized parameters $\hat{\beta} = 0.7$, $\hat{\nu} = 4.0$ and $\hat{\mu} = 1.2$. These values fall in the same range as the normalized parameters for the scrape-off layer in a fusion experiment, and therefore justify the use of DALF3 for the simulation of the plasma in TJ-K. The physical plasma parameters in TJ-K can be varied such that parameter sweeps in the normalized parameters are possible. Examples for parameter sweeps are shown in Tab. 4.1. The physical parameters that can be varied in the experiment are the magnetic field strength, the neutral gas pressure and the RF heating power [43]. Different ion species result in different values for $\hat{\mu}$. Argon ions, however, do not fulfill the requirement for the simulation by DALF3 because the drift scale falls in the range of the perpendicular gradient length.

In the $\hat{\beta}$ scan, the normalized plasma beta can be varied from 1.0 to 0.1. The $\hat{\nu}$ scan allows to vary the normalized parallel resistivity from 1.0 to 10.0. The turbulence in this parameter regime is dominated by the drift instability, as it can be seen from the numerical results of the simulation. Section 7.2 discusses the changes in the turbulence as the normalized parameters vary. The third parameter in Tab. 4.1 is the drift scale ϱ_s. From the normalization described in section 3.4, it is predicted that all length scales in the turbulence scale with ϱ_s.

Consequently, the plasma dynamics in TJ-K is well covered by the DALF3 turbulence equations. The requirements for a successful simulation are fulfilled. The

small size of the experiment and the stellarator field geometry impose only small restrictions on the comparability of simulation results with experimental measurements. In chapter 6 numerous data analysis techniques will be described and evaluated that can serve for this comparison. The experimental measurements are actually done at Kiel and are subject to a different thesis [40].

4.4 Magnetic field geometry

The field geometry for the toroidal confinement of a plasma has been roughly described in section 2.1. The twist of the field lines is measured by the safety factor q. On a field line, the twist is not a constant, and q gives the flux surface average. The change of q with the minor radius is called global shear

$$\hat{S} = aq'/q\,. \tag{4.1}$$

In a stellarator, however, the shearing of the field lines varies along the $\mathbf{B}$ field much stronger than in a tokamak, which is related to the pitch of the field line, $\iota = B_\phi/B_\theta$.

Because the dynamics of the plasma is different in the directions parallel and perpendicular to the magnetic field, it is advantageous for a numerical solution to use a coordinate grid where the coordinate axes are aligned to the magnetic field, the radial pressure gradient and the flux surface. Such a flux tube coordinate system can be defined from the magnetic field structure with the help of Hamada coordinates.

4.4.1 Straight field line coordinates

In Hamada coordinates (χ, θ, ζ) [14, 15], the magnetic field lines are straight. The coordinate $\chi \in [0, 1]$ points in direction of the minor radius and is defined by the flux comprised by the flux surface. $\theta \in [0, 2\pi]$ is the poloidal coordinate, and $\zeta \in [0, 2\pi]$ is the toroidal coordinate. Additionally we introduce a coordinate $\xi = \zeta - q\theta$ such that the magnetic field in the (χ, θ, ξ) coordinates can be written as

$$\mathbf{B} = \nabla\xi \times \nabla\chi\,. \tag{4.2}$$

The $\nabla\xi$ and $\nabla\chi$ are the contravariant base vectors. A transformation from Hamada into cylinder coordinates (R, Φ, Z) can be expressed by a Fourier series,

$$R = \sum_{n,l} R_{nl}(\chi)\cos(n\theta - l\zeta) \tag{4.3}$$

$$\Phi = \frac{\zeta}{N_f} + \frac{1}{N_f}\sum_{n,l} \Phi_{nl}\sin(n\phi - l\zeta) \tag{4.4}$$

$$Z = \sum_{n,l} Z_{nl}(\chi)\sin(n\theta - l\zeta)\,. \tag{4.5}$$

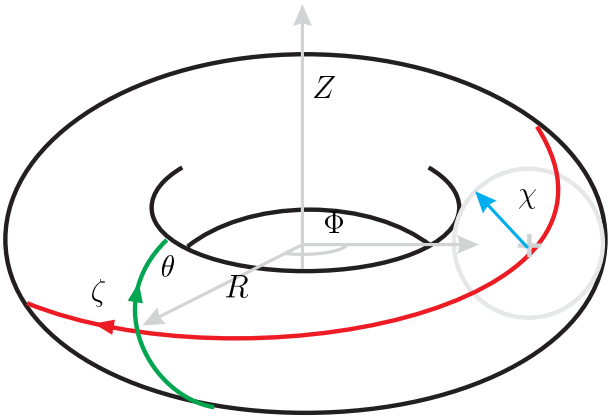

Figure 4.3 Hamada coordinates (χ, θ, ζ) (colored) and cylinder coordinates (R, Φ, Z) (grey). The ζ coordinate line follows a magnetic field line, χ is the flux surface label.

N_f is the number of periods of the magnetic field. In TJ-K, it is $N_f = 6$. The spatial structure of the two coordinate systems are illustrated in Fig. 4.3. The magnetic flux surface is labeled by the χ coordinate (in the direction of the minor radius); the θ and ζ coordinate axis lie in this flux surface. The Fourier coefficients for the expansion (4.3, 4.5, 4.5) are computed from the magnetic coil geometry by a computer program, the GOURDON code [34]. Its algorithm follows the magnetic field lines by integration and returns $R_{nl}(\chi)$, Φ_{nl} and $Z_{nl}(\chi)$. From this results, the flux surface structure is obtained with Eqs. 4.3, 4.5 and 4.5 by fixing χ at a constant value. Fig. 2.3 shows the structure of the flux surfaces in TJ-K. Measurements of the magnetic flux surfaces show a good agreement with the theoretical computations [72].

4.4.2 Flux tube coordinates

From the Hamada coordinates [14], a flux tube coordinate system (x, y, z) can be constructed [61, 59], where $\mathbf{e}_x$ points in the opposite direction of the pressure gradient (in the radial direction), $\mathbf{e}_y$ is parallel to an isobar (i. e. it points in the poloidal direction), and $\mathbf{e}_z$ is along the magnetic field. The flux tube is illustrated in Fig. 4.4: Due to the rotational transform of the magnetic field, a field line falls back onto itself after several revolutions in the toroidal direction. The number of the revolutions is given by the safety factor $q = 1/\iota$. Periodicity is assumed in the z direction. During its revolution, the z axis of the flux tube passes the high and the low field side. Different poloidal positions in the plasma are mapped onto different parallel coordinates. The y coordinate is periodic as well.

The metric of any curvilinear coordinate system is described by the elements of the metric tensor, $g^{\mu\nu} = \nabla\mu \cdot \nabla\nu$. For the flux tube coordinate system (x, y, z),

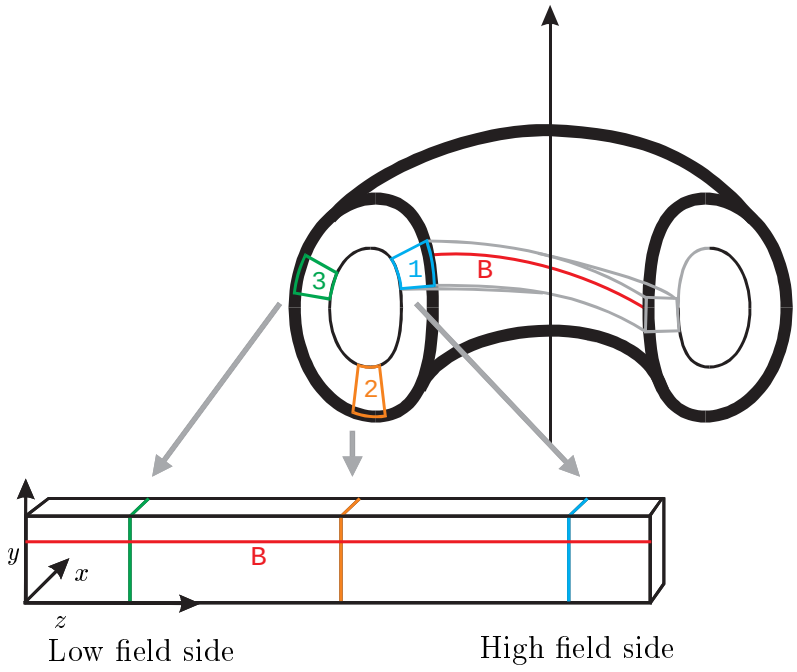

Figure 4.4 Setup of the flux tube coordinate system in toroidal magnetic field geometry.

those are g^{xx}, g^{yy} and $g^{xy} = g^{yx}$. For a simplified tokamak metric, approximating analytical expressions for the $g^{\mu\nu}$ and the other geometrical parameters can be found. For a realistic geometry, these metric coefficients are computed from the R_{nl}, Φ_{nl} and Z_{nl} using the TABTUBE program [31].

There is a common conflict about the definition of poloidal and toroidal directions between experimentalists and theorists. An experimentalist looks at the flux surfaces as a torus, hence in torus coordinates. One of the angular coordinates describes the toroidal angle (associated with the major radius), the other the poloidal angle (associated with the minor radius). When we talk about "poloidal" and "toroidal" directions, we refer to the torus coordinate system of the experimentalists. From the theorists point of view, both toroidal and poloidal coordinates lie in the same flux surface marked by $\chi = \text{const}$. A displacement in either of the coordinates results in a variation of both the (experimental) toroidal and poloidal coordinate. The variation of the geometry is modeled along a magnetic field line. Since in a tokamak, the poloidal coordinate fixes the metric properties, the direction along the magnetic field is named "poloidal" by the theorists. To avoid confusion, we will use the notation "parallel" and "perpendicular" to denote the axes of the flux tube coordinate system. In the perpendicular plane, the radial direction is anti-parallel to the density gradient; the other direction in the perpendicular plane called the drift direction. The actual difference between a poloidal

plane and a perpendicular plane is that the perpendicular plane is inclined by the rotational transform. This inclination is usually small, and together with the fast parallel dynamics of the fluctuations, one can well compare experimental results from a poloidal cross-section with numerical computations for a perpendicular plane.

4.4.3 Magnetic shear

The global shear $\hat{S}$ is defined in terms of Hamada coordinates [32]

$$\hat{S} = \frac{2\chi}{q}\frac{\partial q}{\partial \chi} = -\frac{2\chi}{\iota}\frac{\partial \iota}{\partial \chi}\,. \tag{4.6}$$

Here, χ is the radial Hamada coordinate. The total local shear is defined as

$$\Sigma \;=\; \mathbf{B}\cdot\nabla\left(\frac{g^{\chi\xi}}{g^{\chi\chi}}\right)\,. \tag{4.7}$$

The shearing of the coordinate lines is given by $g^{\chi\xi}/g^{\chi\chi}$. A variation of this quantity is indicated by its gradient. The scalar product with $\mathbf{B}$ projects this change onto the field line, yielding the local shearing. This concept is picked up in the definition of the shifted metric later. The average of the total local shear over a flux surface is $\langle\Sigma\rangle = \hat{S}$. In the following, we will split the total local shear into global $\hat{S}$ and local $\hat{s}$ components according to

$$\hat{S} \;=\; \langle\Sigma\rangle \tag{4.8}$$

$$\hat{s} \;=\; \Sigma - \hat{S}\,. \tag{4.9}$$

In the DALF3 code, the metric elements vary in the direction along the magnetic field lines [61]. Variations in the perpendicular direction, as it would be necessary for the simulation of a whole flux surface, are not allowed. This is due to the numerical scheme that solves the differential equations by Fourier transforming and which cannot treat inhomogeneites in the perpendicular directions. Consequently the dynamics in the flux tube reflects the geometric properties of a single field lines, and inhomogeneities in the metric other than in the parallel direction are not taken into account.

4.5 Model metrics

In this section, we will present the metric used for our studies. It models a simple tokamak with the global parameters of the torsatron TJ-K. However, in TJ-K the local shear dominates the global shear. Therefore, we will discuss how local shear can be included in the DALF3 simulation code.

Table 4.2 List of metric element and their variable names in DALF3. The variables are defined in `main/metric.f90` in the code. Some variables exist for half nodes as well; these variables are marked by a suffix of 2 (e. g. `gxy2`).

Metric element	Variable	Meaning
$(\|\mathbf{B}\|/B_0)^2$	`bbs2`	Magnetic field
g^{xx}	`gxx`	Metric coefficients
g^{yy}	`gyy`	
g^{xy}	`gxy`	$= 0$ for shifted metric
$\mathcal{K}_o$	`wcv`	Curvature terms
$\mathcal{K}_x$	`wcvx`	
$\mathcal{K}_y$	`wcvy`	
α'	`alphap`	shear shift

In Ref. [32] the complete metric properties of a stellarator (Wendelstein 7X) are transformed into flux tube coordinates and used for simulation. This ideal approach failed for the simulation of the plasma in TJ-K because of the very different features of the magnetic field geometry. Wendelstein 7X is an optimized stellarator, with smooth variations in the field geometry and only little local shear when compared to TJ-K. In TJ-K the magnetic field is dominated by strong variations in all metric coefficients. Each time the field line passes a coil, a strong local shearing is observed. These strong variations lead to numerical instabilities. A direct simulation of the real TJ-K geometry using DALF3 is therefore not yet possible. The model metric described in the following is designed to study the influence of the local shear on turbulence.

4.5.1 Simple tokamak metric

The simple tokamak metric takes into account only the first order terms of the Fourier expansion in Eqs. 4.3, 4.5 and 4.5. The simplified transformation from Hamada coordinates (χ, θ, ζ) into a flux tube coordinate system (x, y, z) reads

$$x = \chi - a \tag{4.10}$$

$$y = \frac{a}{q_a}(q\theta - \zeta) = -\frac{a}{q_a}\xi \tag{4.11}$$

$$z = q_a R\theta \tag{4.12}$$

with R and a being the major and minor radius, respectively. The units match as χ is a distance and ζ and θ are angles. In the normalized units of the turbulence equations (cf. Tab. 3.1) the coordinates are dimensionless and $z \in [-\pi, \pi]$ [61, 58]. The x coordinate is antiparallel to the pressure gradient, the y coordinate is in the

drift direction and the z coordinate is parallel to the magnetic field. We find that $g^{\chi\chi} \to g^{xx}$, $g^{\xi\xi} \to g^{yy}$ and $g^{\chi\xi} \to g^{xy}$. The safety factor q at radius a is denoted by q_a. The coordinate system (x, y, z) has the magnetic field lines along z. The elements of the metric tensor are modeled by

$$\frac{\mathbf{B}^2}{B_0^2} = \frac{R}{a}\cos z \tag{4.13}$$
$$g^{xx} = 1 \tag{4.14}$$
$$g^{yy} = 1 \tag{4.15}$$
$$g^{xy} = \hat{S}z \tag{4.16}$$
$$\mathcal{K}_x = \mathcal{K}_0\, g^{xx} \sin z \tag{4.17}$$
$$\mathcal{K}_y = \mathcal{K}_0\,(g^{yy}\cos z + g^{xy}\sin z)\,, \tag{4.18}$$

and vary only in the direction of z. The curvature $\mathcal{K}_0$ is computed as

$$\mathcal{K}_0 = 2\frac{L_\perp}{R}\,. \tag{4.19}$$

Shifted metric The simulation code uses a modified version of this coordinate system to ensure a correct representation of the parallel periodicity [61] in the presence of local shear. From the Fourier representation of the field geometry, a new poloidal coordinate y' is introduced as

$$y_k = y - \alpha'_k\,, \tag{4.20}$$

where $\alpha'_k = g^{xy}/g^{xx}$ is a function of x and z. It is chosen such that $g_k^{xy} = 0$ in the new coordinate system. This means that the new coordinate system is unsheared and the periodicity $(x, y_k, z) \to (x, y_k, z + 2\pi)$ in the parallel direction correctly reflects the shear of the field lines. From the parallel derivative of α' the total shear Σ is computed as $\Sigma = \partial\alpha'/\partial z$. Not only y_k, but also the the $g^{\mu\nu}$ and the curvature terms undergo a transformation when passing to shifted metric [61].

4.5.2 Modeling local shear

The local shearing of the magnetic field is expressed by the metric element g^{xy}. Its implementation in the code uses the shifted metric and transforms this into α'. In the simple tokamak metric with only global shear, g^{xy} is linearly depending on the parallel coordinate, (4.16). For the inclusion of local shear $\hat{s}$, a periodic variation is added to g^{xy}. The form of this variation has been chosen as

$$\Sigma = \hat{S} + \hat{s}_0\,\cos(N_s z)\,. \tag{4.21}$$

Here, N_s is the number of variations in the local shear over one connection length. From this, the metric element g^{xy} is computed using (4.7) as

$$g_{ls}^{xy} = \hat{S}z + \hat{s}_0\,\sin(N_s z)\,. \tag{4.22}$$

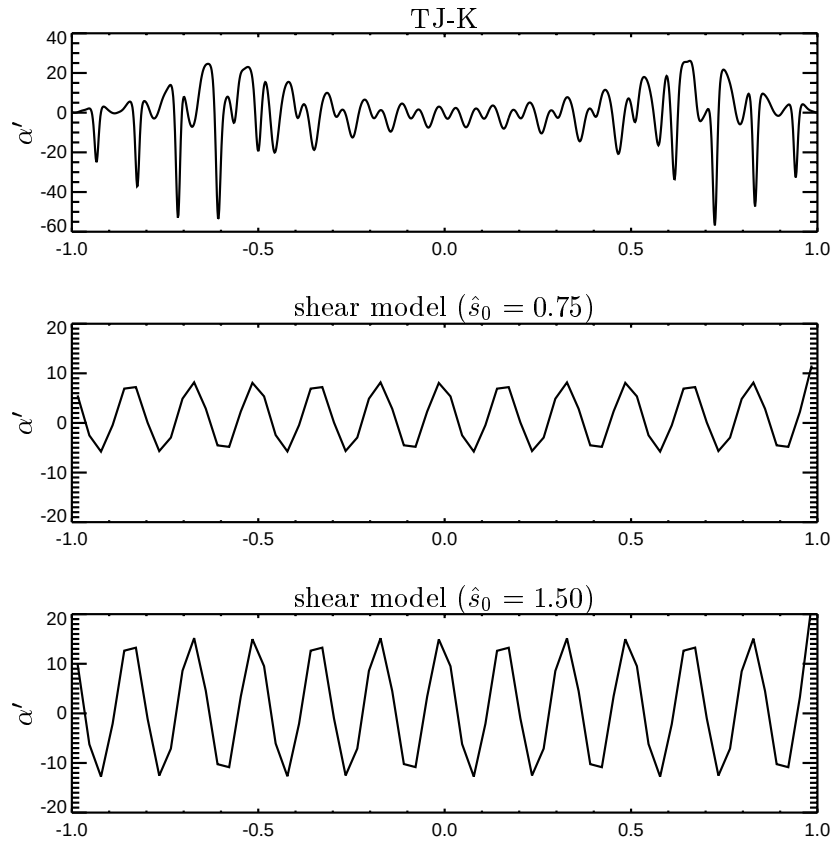

Figure 4.5 The local shear parameter α' in the simplified modeling for DALF3. The range $z \in [-\pi, \pi]$ corresponds to one poloidal revolution.

This modification does not change the global shear $\langle\Sigma\rangle$. In the flux tube coordinate system (x, y, z) it models a local shear with a maximum shearing rate $\hat{s}_0$ and periodicity N_s over one connection length. Following Eq. 4.19, this modification of g^{xy} also modifies the curvature $\mathcal{K}_y$. In the present study, we fixed $N_s = 12$ and varied $\hat{s}_0$ from zero to 1.5. To this metric, the shifting is applied, yielding $\alpha' = g^{xy}$ with a new $g_k^{xy} = 0$. The list of the metric elements used in DALF3 and the variable names is composed in Tab. 4.2. Fig. 4.5 shows α' along a magnetic field line for TJ-K and the model metrics. The results for TJ-K have been obtained for the flux surface label $\chi = 0.6$. The actual metric in TJ-K shows stronger variations with higher local shearing rates and more variations in the parallel direction. Because of the large parallel structure size in the order of the parallel connection length it is however reasonable to assume that despite these differences, the simple shear model yields the correct trends for the influence of local shear on turbulence.

Table 4.3 Geometrical parameters for TJ-K, using the reference configuration at flux surface label $\chi = 0.5$.

Variable	Value	Meaning
R	60 cm	Major radius
a	10 cm	Minor radius
$L_\perp$	5 cm	perp. scale length
$L_\parallel$	13 m	par. scale length
ι	0.26	Rotational transform
N_f	18	toroidal periodicity
$\mathcal{K}_0$	0.13	curvature
$\hat{S}$	−0.3	global shear
$\hat{s}_0$	1.5	local shear

4.5.3 Influence on turbulence

The parallel dynamic of the plasma is bound to the magnetic field lines. A typical turbulence eddy is much larger in the parallel direction than in the perpendicular plane, so that it is sheared with the field geometry. This is illustrated in Fig. 4.6. The sheared field prevents the growth of radially elongated structures by radial decorrelation. This damps the turbulence and reduces the radial transport. In the drift direction (along the y axis), the turbulence eddies are smeared out, so that an increase in the poloidal correlation is expected.

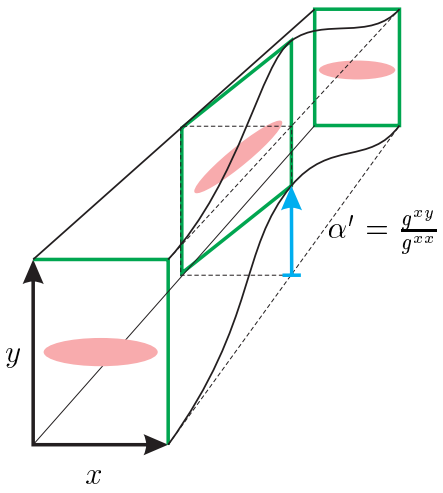

Figure 4.6 Local magnetic shear in the flux tube coordinate system. It leads to a distortion of the turbulence eddies. In the radial direction (x), the structures (red) are decorrelated, and the extend of the structures in the y direction is enlarged. The unsheared coordinate system is shown in thin lines.

The geometrical parameters for the simulation of TJ-K are composed in Tab. 4.3. Section 7.1.1 presents results from the model metrics and discusses what effect the presence of local shear has on turbulence.

5 Turbulence

In this chapter theoretical concepts with relevance to the mircrostructure of the turbulence are presented: The Kolmogorov-41 (K41) theory explains the self-similar properties of the fluctuations in Navier-Stokes turbulence. A brief overview of the K41 is given, followed by a discussion on its validity in plasma turbulence. In a separate sections, self-organized criticality, intermittency and structure formation in plasma turbulence are discussed.

5.1 The Kolmogorov-41 theory

The energy scaling with $k^{-5/3}$ is the most prominent and frequently quoted result of Kolmogorovs famous "K41" theory. It is one of the very few analytical predictions that can be obtained from turbulence equations. It is derived from the Navier-Stokes equations for fluid turbulence. In the this paragraph we will see that the energy scaling in the K41 is the result of the quadratic nonlinearity in the convective derivative $(\partial_t + \mathbf{v}\cdot\nabla)$, which is also present in the plasma equations (3.15, 3.18, 3.22). Therefore the results also give information on the inner working of plasma turbulence. We will present the assumptions and preconditions for the proof [20] of the K41. The goal is to illustrate the narrow conditions under which the theory holds rigorously. Experimental evidence [21], however, suggests that the self similarity properties that follow from the K41 are much more robust than one would expect.

The derivation of the energy scaling is rather complex and requires severals steps. Filtered variables are introduced by mode selection in Fourier space to provide a tool for scale separation. Using the filtered variables, an "energy budget by scale" is established. Kolmogorovs 4/5-law for the scaling of the structure functions follows from these assumptions in a complicated proof [20]. From the 4/5-law, the well-known energy scaling can be derived. We will restrict ourselves to the discussion of the energy budget by scale and the energy scaling law in the inertial range of the turbulence.

The Navier-Stokes equations

$$(\partial_t + \mathbf{v}\cdot\nabla)\mathbf{v} = -\nabla p - \nu\nabla^2\mathbf{v} + \mathbf{f} \tag{5.1}$$

$$\nabla\cdot\mathbf{v} = 0 \tag{5.2}$$

describe the dynamics of an incompressible fluid. Eq. (5.1) is the force balance of a fluid element, taken in the comoving reference frame. Thus, the convective

derivative $(\partial_t + \mathbf{v} \cdot \nabla)$ is applied to the velocity to obtain the acceleration. It is balanced by the pressure gradient ∇p, and friction (due to viscosity, $\nu \nabla^2 \mathbf{v}$). To drive the turbulence, external forcing $\mathbf{f}$ is applied. The velocity field (5.2) is divergence free, reflecting the incompressibility of the fluid.

By filtering the velocity fluctuations in k space, an energy balance by scale can be obtained,

$$\partial_t \mathcal{E}_K + \Pi_K = -2\nu\Omega_K + \mathcal{F}_K \,. \tag{5.3}$$

In the equation, K stands for a "scale", and refers to all fluctuations with a wave vector $|\mathbf{k}| = K$. $\mathcal{E}_K$ is the energy in scale K, $\mathcal{F}_K$ is the external forcing applied to scale K. The viscosity term acts as an energy sink, $-2\nu\Omega_K$. It is related to the vorticity Ω. The remaining term Π_K is the energy flux from scale K to neighboring scales. The energy transport from scale K to smaller scales is due to nonlinear interactions. By integrating (5.3) over all scales, an unfiltered version of the energy balance is obtained,

$$\partial_t \mathcal{E} = -2\nu\Omega + \mathcal{F} \,. \tag{5.4}$$

This equation shows that energy transport across the scales conserves the total energy as Π_K is no longer present in the integrated energy balance. For the further derivation of the scaling law, it is assumed that external forcing $\mathcal{F}$ only acts at the integral scale, i. e. at a scale similar to the system size. This is reasonable for the turbulence of fluids, but not for plasma physics where energy sources can act on any scale. The impact of this difference is discussed in the next section. The viscous dissipation $-2\nu\Omega$ takes place only at infinitesimal scales. It has a fixed dissipation rate ε per unit mass. At intermediate scales, energy is transferred between the scales by Π_K. The K41 defines different dynamical behavior at different scales, sketched in Fig. 5.1: At the integral scale, energy is injected. This is the only mechanism taken into account for this scale. At the smallest scales, energy is lost due to viscous dissipation. This range is therefore called the dissipation range. At the intermediate scales, no sources and sinks are present, and only the energy transport across scales, Π_K, is active. The energy transport in this range is local in $\mathbf{k}$ space and directed to higher wave numbers, i. e. smaller scales. The energy transfer is due to three mode interactions. This is called the energy cascade. In Fig. 5.1, the energy flux between the scales is illustrated. Energy is injected by $\mathcal{F}$ at the integral scales. It cascades down (Π_K) to successively smaller scales $r^i \ell_0$ until it is dissipated at the smallest scales. In the turbulence, structures of all sizes are space-filling. The origin of the Π_K term in Eq. 5.3 can be traced back to the quadratic nonlinearity in the convective derivative $(\partial_t + \mathbf{v} \cdot \nabla)$. A typical power spectrum of a K41 system is shown in Fig. 5.2. It shows constant fluctuations amplitudes in the injection range at large scales, and a scaling (i. e. self similar) behavior in the cascade. The dissipation

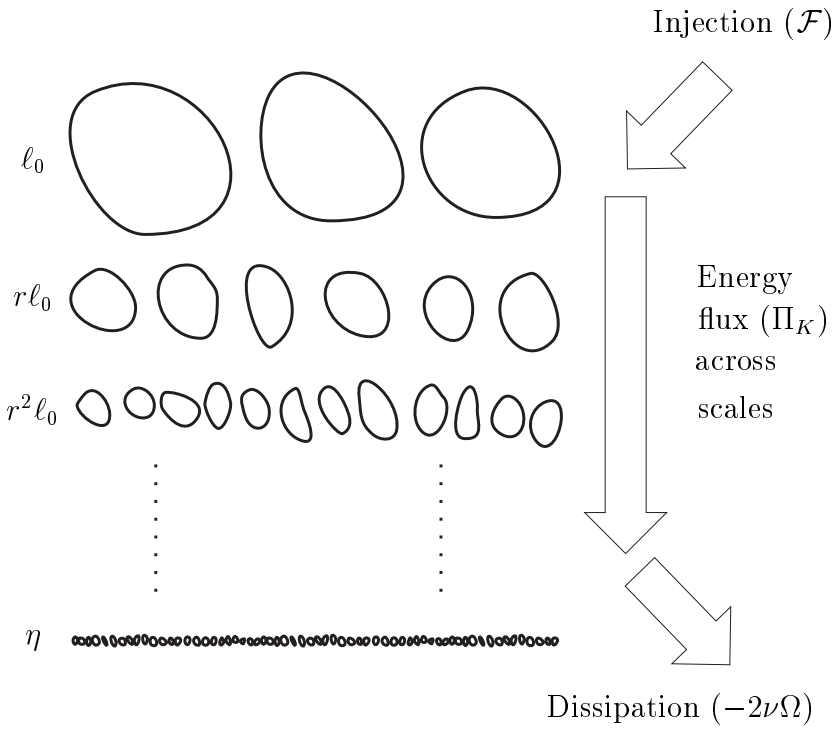

Figure 5.1 The energy cascade of the K41 theory. At all sizes, the eddies are space-filling [20]. The vertical direction is not in space, but in scales.

range is marked by a stronger decay of the fluctuation energy with the wave number.

Several preconditions are required for the derivation of a scaling law in the K41: In the limit of infinite Reynolds numbers, the symmetries of the Navier Stokes equations (rotation, translation, time invariance) must be restored in a statistical sense, for wave numbers larger than in the injection range. For these scales, the turbulent flow is self-similar. It is important to note, that self similarity enters the K41 *as an hypothesis*, and not as a result. The result is the analytically exact scaling exponent for the structure functions. From this, the energy scaling exponent $-5/3$ can be deduced. This prediction is maybe the most popular result of the K41 theory. It is frequently quoted, and self-similar spectra are referred to as "K41-like" even for different scaling exponents.

5.2 Energy scaling in magnetized plasmas

The K41 theory is based on mathematical properties of the Navier-Stokes equations that do not hold for the plasma turbulence equations. They deviate from

these assumptions in several points:

5.2.1 Sources and sinks

In the energy budget by scale (5.3), the K41 assumes energy sources $\mathcal{F}_K$ only in the injection range at the integral scale, and sinks only at the smallest scales. This allows to deduce an exact scaling for the intermediate scales where neither sources nor sinks are present, and the energy budget is entirely determined by the nonlinear energy transfer Π_K. In plasma dynamics, the energy source is the extraction of energy from the background gradient, a process that is active on all scales. A comprehensive discussion of the scale dependence of energy sources and sinks in plasma turbulence is given in Ref. [8].

Power spectra from the numerical simulation as discussed in section 6.4 show a significant deviation from the scaling exponents of the K41.

5.2.2 Anisotropy

The symmetry of the Navier-Stokes equation set (5.1, 5.2) is violated in plasma turbulence: For scales smaller than the injection scale, all spatial directions are equal in the Navier-Stokes system. In the turbulence of magnetized plasmas, the magnetic field vector and the direction of the pressure gradient introduce anisotropy in the plasma equations. This anisotropy has facilitated the derivation of the turbulence equations in chapter 3. As the parallel length scale of the turbulent fluctuations is close to the parallel integral scale, the fluctuations are

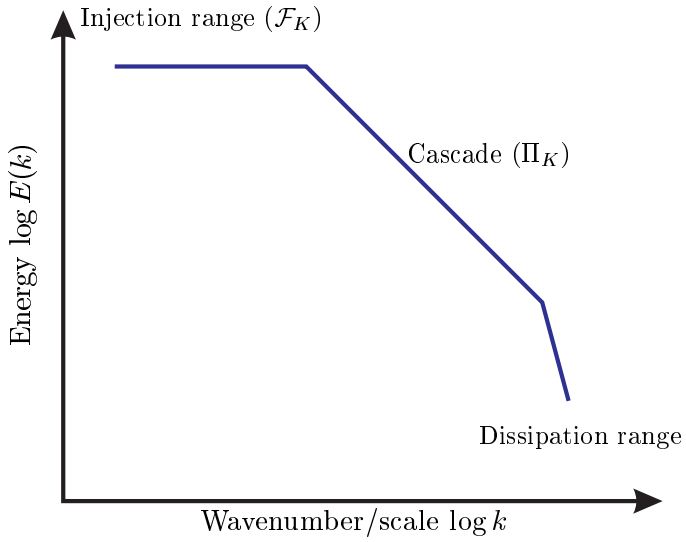

Figure 5.2 A characteristic spectrum for Navier-Stokes turbulence. In the injection range, the energy does not depend on the wavenumber.

closer to 2D than to 3D. This is a key feature of the dynamics of magnetized plasmas. It has been shown [35] that 2D and 3D turbulence have essentially different cascade behavior. Kraichnans approach will be outlined in brief. One of Kolmogorovs starting points was a constant energy flux Π_K and a finite dissipation per unit mass ε. In the other case Kraichnan assumes the conservation of the squared vorticity $\Omega^2 = 2k^2E(k)$ and a constant vorticity transfer rate η. An energy scaling with $E(k) \propto \eta^{2/3}\, k^{-3}$ is obtained from these hypotheses, instead of $E(k) \propto \varepsilon^{2/3}\, k^{-5/3}$ from the energy hypothesis.

In a two-dimensional system, the vorticity constraint results in two possible cascades, with different scaling exponents. One, the energy cascade, has a scaling exponent α of $-5/3$ and is directed towards *lower* wave numbers. It is derived from energy conservation. The second one, the enstrophy cascade, scales with $\alpha = -3$ and transports energy to *higher* wave numbers. It is obtained from the conservation of the enstrophy, which is the total squared vorticity. The energy cascade dominates the low wave number regime of the spectrum, and the enstrophy cascade is more important for high wave numbers, because the enstrophy contains a term k^2 which makes it dominant for large values of k. A cascade dynamics directed to larger scales is referred to as an *inverse cascade*. In a 2D turbulent system, both cascades can be active at the same time; this is called a *dual cascade*. This is the expected behavior for plasma turbulence.

In fluids, the different geometry of a two dimensional $\mathbf{k}$ space, compared to a three dimensional one, gives a reason for the different nature of the energy flux. The energy flux is due to three wave interactions fulfilling the conservation of energy and squared vorticity. In a 3D $\mathbf{k}$ space, local interactions $\mathbf{k}_1 + \mathbf{k}_2 = \mathbf{k}_3$ between neighboring wave numbers ($|\mathbf{k}_1| \approx |\mathbf{k}_2| \approx |\mathbf{k}_3|$) dominate, and justify the assumption of a local energy transport across scale. In a 2D system, the interactions between different wave numbers are no longer local because of the vorticity constraint, allowing the derivation of the dual cascade. Energy is transported to smaller scales, and vorticity is goes to larger scales via the inverse cascade. In a plasma, the vorticity can be expressed in terms of the potential, so the potential fluctuations should follow the inverse cascade dynamics. The same result is obtained from the two dimensional Hasegawa-Wakatani equations for drift wave turbulence [28].

The link between potential fluctuations and the vorticity can be explained in a pictorial fashion: A localized potential perturbation leads to $\nabla\phi$ pointing either into it or out of it. A circular $\mathbf{E}\times\mathbf{B}$ motion is the result. Such a circular structure forms a vortex, or eddy, with an angular momentum, i. e. a vorticity.

5.3 Self organized criticality and intermittency

The concept of self-organized criticality (SOC) originates from the analysis of a sandpile. A whole family of systems with similar dynamics [3] has been discovered since. In plasma physics SOC is discussed as a paradigm for the transport fluctuations [46]. The idea is that a sandpile possesses a critical gradient. When this gradient is exceeded by the local addition of density, an avalanche starts. Its growth is due to the domino effect: once the critical gradient is exceeded, density is transported down the sandpile. This increases the gradient at the neighboring position, which in return exceeds the critical threshold, leading to a growing perturbation. The size ℓ of an avalanche is defined as the total mass in the transport event. The size distribution $p(\ell)$ for the avalanches follows a self similar scaling with $p(\ell) \propto \ell^{-1}$. When this size distribution is compared to a Gaussian probability distribution, large deviations from the mean value a significantly more frequent in SOC systems. This phenomenon is called intermittency.

Intermittency is not particular to the avalanches in SOC. Totally different definitions for intermittency are used in the analysis of dynamical systems [55] and turbulence [20]. In the analysis of time series, a system is called intermittent if its behavior alternates between relatively long, regular phases and relatively short irregular bursts [55]. In fluid turbulence, intermittency is observed as a deviation from the analytically predicted scaling laws [20]. Sources for these deviations can be found in the non-Gaussian statistics of the fluctuations, in the self-similarity of the cascade dynamics and in effects that are specific to the dissipation range [36].

The experimental diagnostic of intermittent behavior is based on the probability distribution of the fluctuation amplitudes. The kurtosis (cf. section 6.3.1) is a measure for the relative frequency of large events. We call a fluctuating variable intermittent if large events are significantly more frequent then in a standard Gaussian distribution. Such an behavior has been observed in the transport fluctuations measured at the plasma edge of several fusion experiments [9, 54]. The intermittent nature of the transport fluctuations inspired different paradigms for the generation of these large events. Convective cells, "streamers" and avalanches have been suggested, and will be discussed in the next section. It was also shown that intermittent transport fluctuations can arise from Gaussian distributed density and potential fluctuations [10]. This will be addressed in detail in section 6.3.1 where the intermittency properties of the numerically simulated turbulence are discussed.

5.4 Structure formation

In the K41, the turbulence has been treated as a composition of Fourier modes in nonlinear interaction. The strength of a Fourier approach lies in the analysis

of linear and weakly nonlinear systems, where only a few modes couple. For the studies of fully developed turbulence these methods are of limited use, because the turbulent fluctuations do not show wave-like structures, but resemble to a gas of moving eddies. An alternative approach takes not a wave, but a "coherent structure" as the basic component of the fluctuations. A structure is called coherent, if it reoccurs in a statistical sense and can therefore be regarded as a universal structure in the turbulence. A coherent structure is not a coherent mode which is localized in $\mathbf{k}$ space at a fixed wave number. A coherent structure is localized in the real space. In plasma turbulence, different types of structures are observed in experimental and theoretical studies.

5.4.1 Radial structures

When the MHD interchange instability (cf. section 2.2.5) is active, high density fluid elements are convected down the gradient, and low density is convected up in exchange. The velocity field is circular, i. e. vortex-like, and centered around a potential fluctuation $\tilde{\phi}$. Thus the fluctuation extracts energy from the gradient, and grows. This instability is essentially 2D, as it leads to fluctuations that grow simultaneously along the magnetic field line. Consequently it follows a dual cascade dynamics, and its growth can be attributed to the inverse cascade.

It is a widespread assumption, that most of the transport in a turbulent plasma is due to a few, but large events. This is also supported by experimental evidence [9] and numerical computations [10]. There are various possible mechanisms for the generation of large events. The simplest concept is the convective cell that can be understood in the linear picture of the interchange instability. More advanced, nonlinear paradigms are streamers [30] and avalanches [12]. Both structures have in common to form radially elongated structures.

Avalanches have been discussed as a transport mechanism in the context of SOC. In ion temperature gradient driven modes (cf. section 3.5.1), a critical gradient is observed, so SOC dynamics appears to be possible in that kind of turbulence [22]. The investigations where centered around the spectral properties of the fluctuations in the plasma parameters [12] and the size distribution of transport events [11]. As a result, SOC has been suggested as the mechanism behind the stiff density profiles in fusion experiments [12] and simulations [54]. It was argued that a scaling exponent of $\alpha = -1$ and the intermittent nature of the transport fluctuations are the signatures of self-organized, critical behavior. However, it has been shown that the scaling exponent of $\alpha = -1$ can also be generated by systems with completely different dynamical properties [39]. The observation of avalanches as localized, propagating transport events would be a signature of SOC, but the experimental observations (power spectra and PDF) are not sufficient to conclude that SOC is important.

Streamers are radially elongated transport events, not unlike avalanches. In

contrast to an avalanche, a streamer forms a transport channel with a lifetime that is longer than the typical time scales of the turbulent fluctuations. Streamers have been observed in simulations of ITG and ETG turbulence, and their decay is due to the Kelvin-Helmholtz instability. In Ref. [54], the existence of streamers (again in ITG turbulence) was observed to lead to intermittent transport fluctuations. In contrast to an avalanche, a streamer is a long living, radially elongated transport channel at a fixed radius.

Neither streamers nor avalanches have yet been observed in drift wave turbulence. Since drift wave and MHD interchange dynamics do rely on a critical gradient, the existence of a SOC-like mechanism is unlikely in these systems. Radially elongated convective cells are observed, and it is difficult to tell them apart from streamers.

5.4.2 Poloidal structures

Zonal flows (ZF) have first been observed in geophysics [7]. In plasma physics, a zonal flow is a potential fluctuation with poloidal and parallel mode numbers of zero, i. e. a collective potential perturbation in the flux surface [45]. Such a perturbation induces a sheared velocity field. Fluctuation eddies entering the area of velocity shear are torn apart, and the correlation in the radial direction is reduced. This is shown in Fig. 5.3. As a result of the decorrelation the radial transport decreases. A tilted and distorted vortex has a statistical correlation

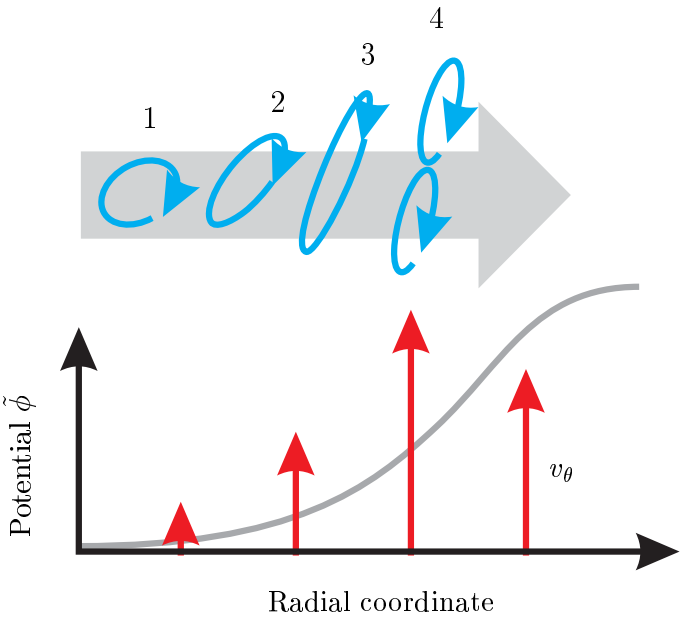

Figure 5.3 A vortex which enters the sheared velocity field of a zonal flow. It is distorted (1, 2, 3) and finally torn apart (4). This reduces the radial correlation length in the turbulence.

$\langle v_r v_\theta \rangle$ due to the shear flow. The quantity $\langle v_r v_\theta \rangle$ is called Reynolds stress. It has been used in the experimental detection of zonal flows [47].

The mechanisms behind the generation of zonal flows are currently discussed [22]. Several effects have been suggested. Rogers *et al.* [53] suggested the generation from radial transport events (streamers) via the Kelvin-Helmholtz instability in ITG turbulence. In the core-edge transitional regime, large poloidal flows have been observed and traced back to geodesic acoustic modes (GAM) [26]. A geodesic acoustic mode differs from a zonal flow in that it has $k_\parallel \approx (qR)^{-1}$. Reynolds stress is described as the generation mechanism for these flows [16]. In drift wave turbulence, zonal flow formation via Reynolds stress has been observed. The energy flux goes like [56]

$$\text{Reynolds Stress} \rightarrow \text{ZF} \rightarrow \text{GAM} \rightarrow \mathbf{E} \times \mathbf{B} \text{ nonlin.} \rightarrow \text{Turbulence}\,.$$

In drift wave turbulence, the generation of a zonal flow via Reynolds stress is a nonlinear phenomenon. According to Ref. [16], a triad interaction between different wave vectors $\mathbf{k}_1$, $\mathbf{k}_1$ and $\mathbf{k}_1$ takes place, such that $\mathbf{k}_1 = \mathbf{k} - \mathbf{z}$, $\mathbf{k}_2 = -\mathbf{k}$, $\mathbf{k}_3 = \mathbf{k}_z$. Here, $\mathbf{k}_1 \approx \mathbf{k}_2 \approx \mathbf{k}$ are wave vectors of the drift wave turbulence, and $\mathbf{k}_z = q\mathbf{e}_r$ is a zonal flow wave vector, with $|\mathbf{k}| \gg |\mathbf{k}_z|$. This in an extreme case of an non-local interaction in $\mathbf{k}$ space (cf. section 5.2) and can be seen as a mechanism of the inverse cascade. The wave vector of the zonal flow points in the direction of the gradient, its poloidal and parallel wave numbers are zero. The intensity of the three mode interaction can be measured by the bicoherence of the velocity fluctuations and the potential [16].

6 Data analysis

This section describes data analysis tools that can be applied to both experimental and numerical data. The techniques are therefore suitable for experiment-theory comparisons. In order to demonstrate their importance, the methods are applied to results from the simulation and discussed in the context of plasma turbulence. The results are from a flux tube with coordinates x, y and z for the radial (∇p), poloidal (drift) and parallel ($\mathbf{B}$) directions. Throughout this section, we follow the convention that a generic space-time variable is denoted by u; when density and potential or transport fluctuations are addressed specifically, they are denoted by $\tilde{n}$, $\tilde{\phi}$ and Γ, respectively.

This chapter is organized in several sections. The first describes the data obtained from the simulation and gives a first overview of the nature of the space-time fluctuations. The second section presents a coherent-structures approach to data analysis. It focuses on statistical properties and generating processes for events such as vortices. In the third section data is Fourier transformed and analyzed in k and ω space. Features are found that have been predicted in the framework of the K41 theory. Finally, the signatures of the turbulence driving mechanisms in the data sets are discussed.

6.1 Data formats and examples

The simulation computes the fluctuations for density $\tilde{n}$, potential $\tilde{\phi}$ and parallel vector potential $\tilde{A}_{||}$ on a three dimensional grid in the flux tube. For a standard run, the flux tube contains $n_x \times n_y \times n_z = 64 \times 128 \times 16$ points. The variables $(\tilde{n}, \tilde{\phi}, \tilde{A}_{||})$ are computed for each time step. The radial transport Γ_r is defined by

$$\Gamma_r \quad = \quad \frac{\tilde{n}\,\partial_y \tilde{\phi}}{B_0}\,. \tag{6.1}$$

Since all quantities $(\tilde{n}, \tilde{\phi}, B_0)$ in that definition are dimensionless in the simulation, Γ is a dimensionless quantity as well, and will be discussed in the dimensionless form. The fluctuating variables are stored in the form of a poloidal plane with size $n_x \times n_y$ for every time step. Two of these cutting planes have been defined, one at the high-field side, and one for the low-field side. The analysis in this chapter is restrained to data from the low-field side. Three different data sets are used to illustrate the analysis techniques: All are obtained for $\hat{\beta} = 2.75$, $\hat{\nu} = 4.0$

and $\hat{\mu} = 0.3$ (in a simplified tokamak-like metric as discussed in chapter 4). The parameter set has been chosen such that both MHD and drift wave instability are active. This will be referred to as the standard data set. Two other data sets are used to demonstrate the signatures of the different turbulence driving mechanisms. To this end, one of the driving mechanisms has been disabled at a time. In the run called "MHD", the pressure term $\nabla_{\|} p$ is dropped from the electron momentum equation (3.22) and the diamagnetic compression terms are removed from the energy equation (3.18). The resulting equation set reverts to reduced MHD and does no more contain the drift instability. In the run called "DAW", the MHD interchange instability has been disabled by setting the curvature terms $\mathcal{K}$ (4.17, 4.18, 4.19) to zero, keeping the drift-Alfvén instability active. Note that the DAW and the MHD run do not correspond to realistic physical scenarios, but serve as test cases for the demonstration of characteristic turbulence signatures.

6.2 Space-time data

The raw data for a fluctuating variable already give insight in basic properties of the turbulence. All further analysis methods in this chapter cannot add information to this. In the contrary, their goal is to *remove* information that is irrelevant in a certain context, and give a sharper look on selected properties. Thus, the visual inspection of the fluctuations can give important hints for further investigation. Turbulence dynamics does not only have a temporal, but also a spatial component. Due to the special situation in magnetized plasmas, we have chosen the perpendicular plane for the visualization of the fluctuations.

A cut trough the perpendicular (x, y) plane at an instant t_0 is shown in Fig. 6.1. The sampling was done on the low-field side of the plasma, where the turbulence is stronger due to the unfavorable curvature. Other cutting planes are possible, but not covered here. The time traces of the fluctuations are shown in Fig. 6.2. All data has been sampled from the standard run including both instabilities.

Physical interpretation and results The spatial structure of density, potential and (radial) transport fluctuations are shown in Fig. 6.1. The drift direction (also referred to as the poloidal direction) is denoted by y; it is in the isobar. The pressure gradient is to the left, and the magnetic field lines are perpendicular to the plane. The fluctuating structures move from the left to the right, down the density gradient. From the comparison of the density and potential fluctuations, one sees that the two are coupled and have similar structures as a consequence of the parallel drift dynamics. The potential fluctuations appear on a larger spatial scale than the density fluctuations.

The transport fluctuations exhibit a completely different structure. This is a feature that is robust throughout all the following analysis. Reasons for this will be given in section 6.3.1. The transport events are rather localized in the poloidal plane and more

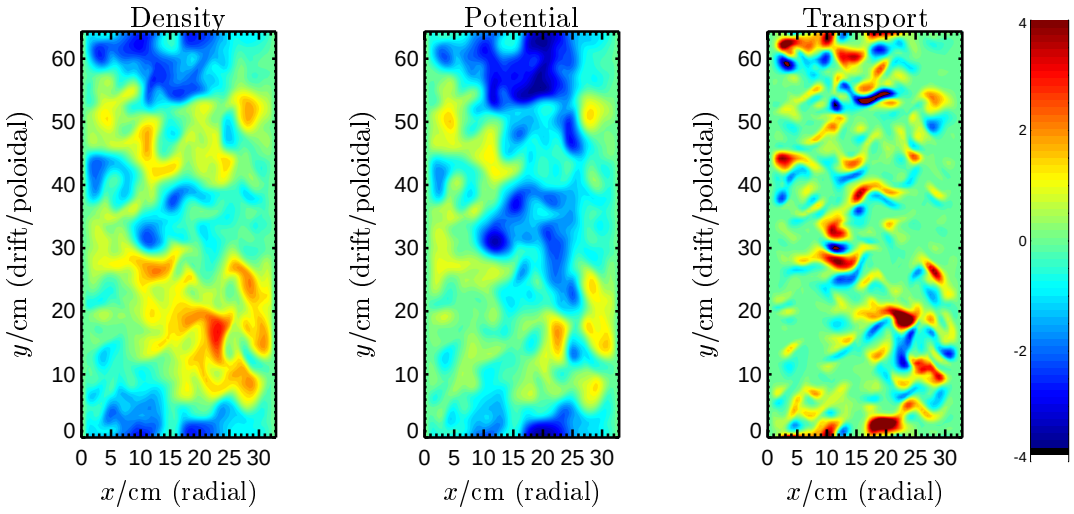

Figure 6.1 Fluctuation of density, potential and radial transport in the perpendicular plane (standard run).

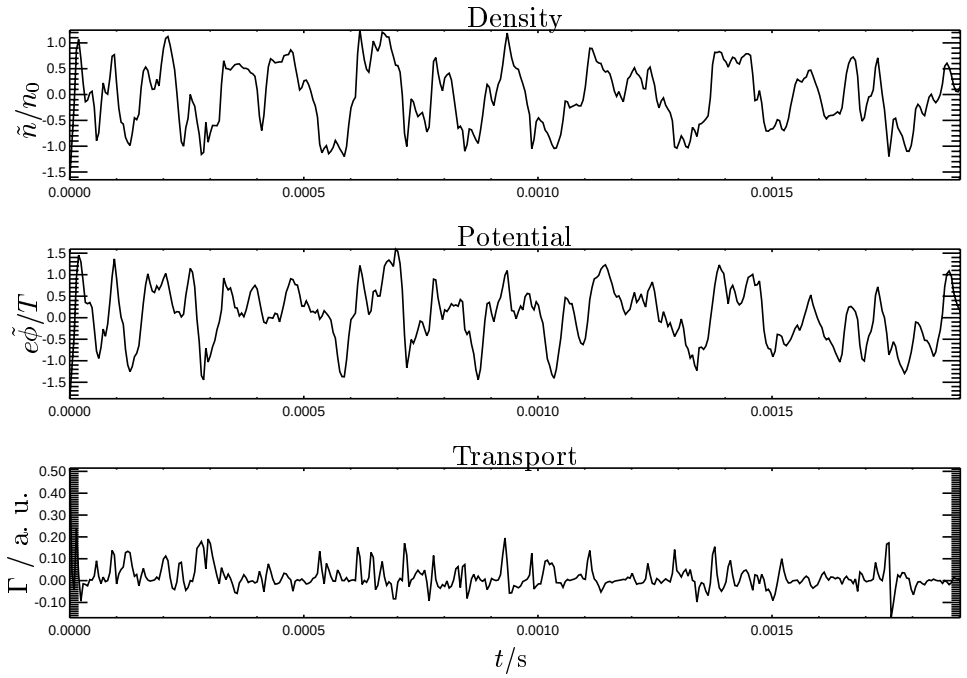

Figure 6.2 Time traces of density, potential and radial density transport fluctuations at a fixed point (standard run).

frequent. They have a characteristic size of about two centimeters in the poloidal direction, and varying lengths in the radial directions. The poloidal length scale of the potential fluctuations is much larger. The transport events always occur paired, i. e. inward and outward transport events lie close together and form a dipole-like structure. The radially extended events have the spatial structure of streamers, and a comparison with the potential structures identifies them as radially elongated convective cells. Poloidally elongated radial transport events are not observed. Fig. 6.2 shows time traces of the fluctuating variables, sampled at a fixed location in the simulation volume at the low field side. Again, density and potential fluctuations appear to be coupled since they behave similarly. A direct comparison of the time series shows that $\tilde{n}$ and $\tilde{\phi}$ are roughly in phase. While $\tilde{n}(t)$ and $\tilde{\phi}(t)$ look similar, the transport behavior is clearly different. This is a feature already familiar from the spatial data (Fig. 6.1). Low amplitude fluctuations are interrupted by rare events with high amplitudes. This is complementary to the observed spatial structure of the transport events. We will see in the next section that this is linked to the intermittency property of the transport fluctuations.

6.3 Statistical analysis

In this section, statistical properties of the space-time fluctuations are investigated. The distribution of the fluctuation amplitudes provides a first insight in the turbulence, but does not provide spatial resolution. A special use of the cross correlation is defined, yielding information on the typical fluctuation structures. The analysis of the spatial structures is completed with a discussion of conditional averaging.

6.3.1 Probability distribution function

Given a time series $u(t)$, the probability density function (PDF) is the probability for a certain value of $u(t)$ to occur. Hence it is the distribution of amplitudes in the time series. It is straightforward to compare it to a Gaussian standard distribution function,

$$P_G(u) = \frac{1}{\sqrt{2\pi}\sigma_u} \exp(-(u - \langle u \rangle)^2 / 2\sigma_u^2) \tag{6.2}$$

and to look for deviations. Here, σ_u is the standard deviation and indicates the typical fluctuation amplitude. It is defined as

$$\sigma_u^2 \;=\; \frac{1}{N-1} \sum_{j=1}^{N} (u_j - \langle u \rangle)^2 \,. \tag{6.3}$$

The moments m_k of a probability distribution are defined by [52]

$$m_k = \frac{1}{N}\sum_{j=1}^{N}\left(\frac{(u_j - \langle u\rangle)}{\sigma_u}\right)^k . \tag{6.4}$$

Here, N is the number of available points for the summation. In this general definition, $\langle u\rangle$ is the average value. The moments of the order $k = 3$ and $k = 4$ are called skewness S and flatness F of the distribution. From the flatness, the kurtosis is obtained as $K = F - 3$. For a Gaussian distribution with $\langle u\rangle = 0$ and $\sigma_u = 1$, the values are $K = 0$ ($F = 3$) and $S = 0$. Different values suggest that the time series is not generated by a Gaussian process. The *skewness* of a probability distribution quantifies its asymmetry. It indicates weather large events are more probable for positive or negative fluctuation amplitudes, thus measuring the asymetry of the PDF. The *kurtosis* measures the relative frequency of large deviations from the mean value, compared to a standard Gaussian case. A value of $K > 0$ signals that large deviations from the mean value are more frequent than in a Gaussian time series.

Under certain conditions, analytical values for the skewness and the kurtosis can be obtained. For a variable u_j that is the product of two Gaussian distributed variables ξ^1 and ξ^2,

$$u_j = \xi_j^1 \cdot \xi_j^2 , \tag{6.5}$$

values for the skewness and the kurtosis can be computed as [10]

$$S = -2\gamma\frac{3+\gamma^2}{(1+\gamma^2)^{3/2}} \tag{6.6}$$

$$K = 3\frac{3+14\gamma^2+3\gamma^4}{(1+\gamma^2)^2} , \tag{6.7}$$

where $\gamma = \langle \xi^1 \xi^2\rangle$ is the correlation between the two fluctuating variables. As γ is varied from -1 to 1, S changes from 2.83 to -2.83. The fourth order moment, the kurtosis K, varies from 9 for $\gamma = 0$ to 15 for $\gamma = \pm 1$. In all cases, the multiplication of the two statistical variables leads to a significantly higher kurtosis than for a Gaussian variables. This especially affects the kurtosis of the transport fluctuations (6.1). When $\tilde{\phi}(t)$ is Gaussian distributed, $\partial_y \tilde{\phi}(t)$ also has a Gaussian PDF [10]. Therefore the theorem (6.7) can be applied and a high kurtosis is expected for the transport fluctuations Γ.

For a comparison of the higher order moments, an experimentally or numerically obtained time series $u'(t)$ is usually normalized to be of mean value zero and of standard deviation one,

$$u(t) = \frac{u'(t) - \langle u'\rangle}{\sigma_{u'}} . \tag{6.8}$$

Table 6.1 First moments (mean value $\langle u \rangle$, standard deviation σ, skewness S, kurtosis K) for the fluctuations of density and potential, shown for the MHD-only model, the drift wave model and both instabilities in interaction.

Run	Variable	$\langle \Gamma \rangle$	σ	S	K
DAW	$\tilde{n}/n$	—	0.21	−0.12	−0.32
	$e\tilde{\phi}/T$	—	1.03	−0.49	−0.59
	Γ	0.00065	0.0091	−0.5	15.46
MHD	$\tilde{n}/n$	—	1.16	0.01	−0.36
	$e\tilde{\phi}/T$	—	0.49	−0.05	0.58
	Γ	0.058	0.097	−2.50	9.21
both	$\tilde{n}/n$	—	0.46	0.00	−0.05
	$e\tilde{\phi}/T$	—	0.65	−0.08	0.02
	Γ	0.0076	0.08	−1.30	10.60

This procedure has been carried out at for each x coordinate individually. This is necessary because zonal flows and geodesic acoustic modes would otherwise lead to distorted results.

Physical interpretation and results The first moments of the density, potential and transport fluctuations are listed in Tab. 6.1 for all three models. The transport has been computed according to Eq. (6.1). The mean value of the fluctuations is close to zero and of no interest because the absolute quantities are part of the background. The mean value of the transport Γ gives the average fluctuation induced transport through a flux surface. The transport in the MHD interchange turbulence is higher than in the drift wave-only model by nearly two orders of magnitude. The standard run, comprising both instabilities, has an intermediate transport level. The presence of the drift dynamics hence tames the transport due to MHD interchange turbulence. We will later see that the mechanism behind this is the phase coupling between $\tilde{n}$ and $\tilde{\phi}$ by the fast parallel electron dynamics.

The standard deviation σ_u is a measure for the typical amplitude. The drift wave model has the lowest fluctuation amplitudes, and MHD interchange instability alone gives the highest fluctuations. Drift wave turbulence produces higher fluctuations in $e\tilde{\phi}/T$ than density fluctuations $\tilde{n}/n_0$. The inverse is true for MHD interchange turbulence. The Boltzmann relation, $e\tilde{\phi}/T = \tilde{n}/n_0$, is roughly satisfied only in the standard run. All mean fluctuations lie above the mixing level estimate of $e\tilde{\phi}/T = \tilde{n}/n_0 \approx \varrho_s/L_\perp = 0.1$.[1] This can be an effect of the fixed background gradient in

1 Since the MHD and DAW models do not represent a real physical situation, fluctuation amplitudes larger than unity are not worrisome.

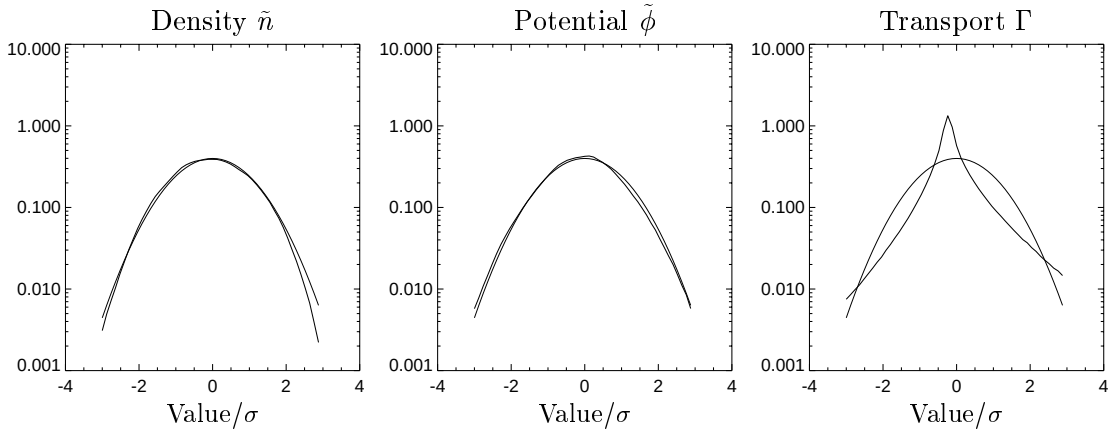

Figure 6.3 Probability distribution functions for density, potential and transport fluctuations. The thin line shows a Gaussian that has been overlayed for comparison.

the simulation. It has been shown that non-local codes like DALF3 systematically overestimate the fluctuation amplitudes [5].

For density and potential, the higher order moments skewness and kurtosis are close to Gaussian. The transport fluctuations are of a different nature. They are both asymetric and intermittent, indicated by $S = -0.5...-1.3$ and $K = 9.21...15.46$. Fig. 6.3 shows the entire distributions for $\tilde{n}$, $\tilde{\phi}$ and $\tilde{\Gamma}$ from the model with both instabilities active. The transport is positive in the outward direction. A Gaussian standard distribution has been overplotted for comparison. Potential and density follow the Gaussian distribution closely, but the transport PDF is strongly peaked. Both very low and high fluctuation amplitudes $|u| > 2\,\sigma$ are much more probable than for a Gaussian of the same standard deviation. The interpretation for this is that an important fraction of the transport is due to large events, that interrupt "laminar" phases with a smaller fluctuation level. This has already been observed in the perpendicular plane (Fig. 6.1) and the time traces (Fig. 6.2). This feature has been pointed out as an argument for self organized criticality [46], but the significance of these effects should not be overestimated, as K is within the bounds of the values predicted by Eq. 6.7. From the drift wave model, a high correlation between density and potential is expected. Under the assumption that the velocity and potential fluctuations behave similarly, this leads to a predicted kurtosis $K = 15$. For MHD interchange turbulence, density and potential fluctuations are expected to be uncorrelated. This results from the phase shift of $\pi/2$, and yields $K = 9$. Although these arguments are very rough estimates, they are in good agreement with the results from the simulation.

The asymetry of the fluctuations reflects the fact that a large transport event down the gradient is more likely than a fluctuation in the opposite direction. In Fig. 6.4, the transport PDF for the drift-wave only dynamics and the MHD interchange model are plotted. In both cases, the fluctuations are intermittent, but the pronounced skewness only appears in the MHD interchange model.

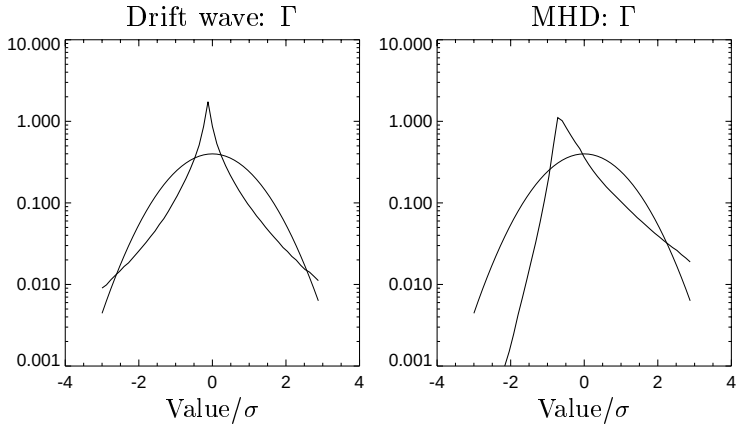

Figure 6.4 Probability distribution function for the transport fluctuations in drift wave and MHD interchange turbulence. In MHD turbulence, the transport is very asymetric.

6.3.2 Correlation functions

The autocorrelation function $C(\tau)$ is the probability that the (discrete) time series $u(t)$ at time t and time $t + \tau$ behaves identically. It is obtained from

$$C_u(\tau) = \frac{1}{N} \sum_{j=1}^{N} u(t_j)\, u(t_j + \tau) = \langle u(t)\, u(t + \tau) \rangle \ . \tag{6.9}$$

C_u is bounded between minus one and one if u has been normalized according to Eq. 6.8. For a periodic signal, the autocorrelation function has the same periodicity as the signal itself. Similar to the autocorrelation function, a cross correlation between two different variables can be defined as

$$C_{uv}(\tau) = \frac{1}{N_t} \sum_{j=1}^{N_t} u(t_j) v(t_j + \tau) = \langle u(t)\, v(t + \tau) \rangle \ . \tag{6.10}$$

In the analysis of space-time data, it is advantageous to compute the cross correlation between neighboring points [49], e. g. $u(t) = \tilde{n}(x_0, y_0, t)$ and $v(t) = \tilde{n}(x_0 + \Delta x, y_0 + \Delta y, t)$,

$$C^t_{uv}(\Delta x, \Delta y, \tau) = \frac{1}{N_t} \sum_{j=1}^{N_t} u(x_0, y_0, t_j) v(x_0 + \Delta x, y_0 + \Delta y, t_j + \tau) \, . \tag{6.11}$$

For brevity, we will refer to C^t_{uv} as C_{uv}. A value of $C_{uv} = 1$ means that the variables u and v have identical time traces, i. e. maximal correlation. A value of zero indicates the absence of any correlations between the variables, and $C_{uv} = -1$ is the result of an anti-correlation, where $u = -v$ for all time steps. Intermediate values give a measure for the coincidence of fluctuations in u and v. Using

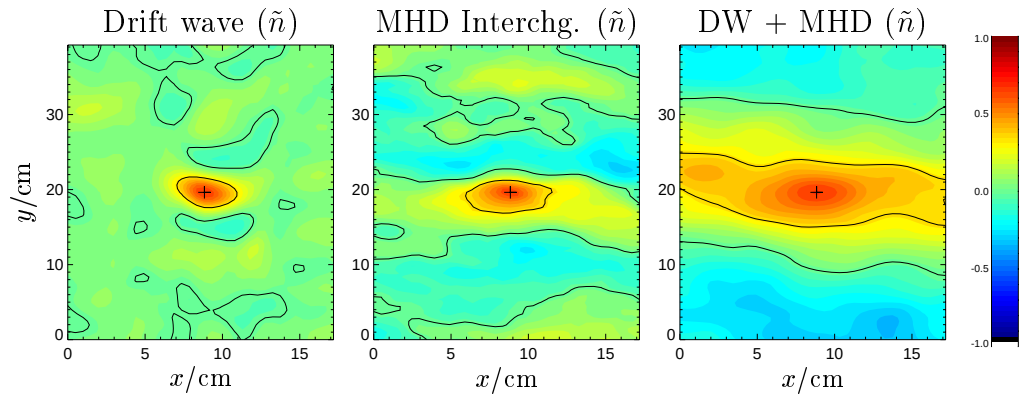

Figure 6.5 Perpendicular cross correlations for the density fluctuations for the three runs.

the definition of Eq. 6.11, $C_{uv}(\Delta x, \Delta y)$ is displayed as a color-coded plot in the $(\Delta x, \Delta y)$ plane. The figures give insight in the typical shape and size of a typical coherent structure. It is important to note that C_{uv} as defined above is not equal to the spatial autocorrelation,

$$C_{uv}^{xy}(\Delta x, \Delta y, \tau) = \frac{1}{N_y} \sum_{j=1}^{N_x} \sum_{k=1}^{N_y} u(x_j, y_k, t_0) v(x_j + \Delta x, y_k + \Delta y, t_0 + \tau)\,. \quad (6.12)$$

In C^{xy}, the sum runs over the spatial index of the space time data. In contrast to the spatial autocorrelation, the definition (6.11) yields much better statistics since we have much more points in time (typically several thousand for the simulation, and up to 10^6 for the experiment) than in space (128 in the simulation, 64 in the experiment). Mathematically, the space average of the poloidal cross correlations (6.11) is identical to the time averaged spatial correlation C^{xy} (6.12),

$$\left\langle C_{uv}^{t}(\Delta x, \Delta y, \tau) \right\rangle_t = \langle C_{uv}^{xy}(\Delta x, \Delta y, \tau) \rangle_{x,y} \quad =$$

$$\frac{1}{N_x N_y N_t} \sum_{i=1}^{N_x} \sum_{j=1}^{N_y} \sum_{k=1}^{N_t} u(x_i, y_j, t_k) v(x_i, y_j + \Delta y, t_k + \tau)\,, \quad (6.13)$$

because the sums over the spatial and temporal indices can be exchanged. For simplicity, the equation is expressed for only one spatial direction y, but the two dimensional equivalent is easy to form. In the homogeneous perpendicular plane, C^t can hence be used to approximate C^{xy}. When the correlation functions are used to measure typical scale lengths, these lengths are systematically overestimated. The cross correlation of two Gaussian structures with the width σ_1 and σ_2 yields a correlation length of $\sigma^2 = \sigma_1^2 + \sigma_2^2$ [24].

Physical interpretation and results Fig. 6.5 shows the cross correlations of the density fluctuations in the perpendicular plane, obtained from the three different mod-

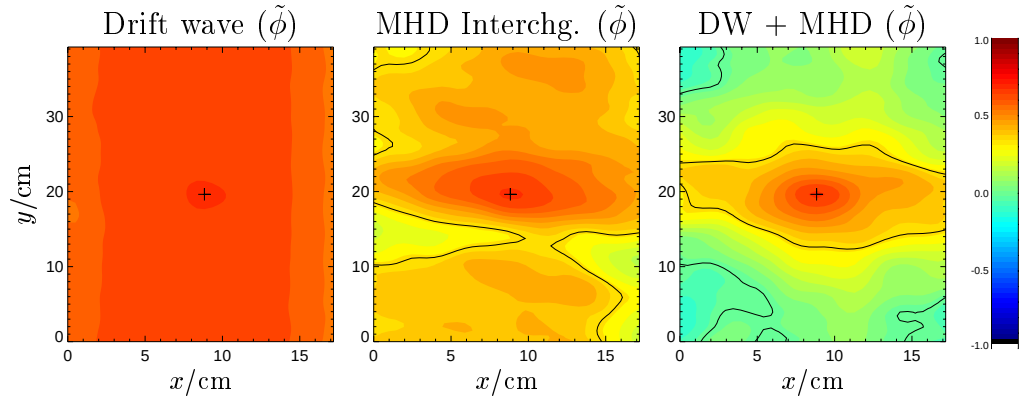

Figure 6.6 Perpendicular cross correlations for the potential fluctuations for the three runs.

els. For the delay, $\tau = 0$ has been used, and the reference point (x_0, y_0) is marked by a cross. In both MHD and drift wave turbulence, a periodic part can be observed with $\lambda_{MHD} \approx 18\,\text{cm}$ and $\lambda_{DAW} \approx 9$ cm. While the correlation length in the poloidal direction is similar for MHD and drift wave turbulence, the former has a pronounced elongation in the radial direction. These convective cells are typical for the MHD interchange instability. Together with the results from section 6.3.1, this shows that the MHD interchange dynamics is the more violent one. Larger spatial structures go hand in hand with high fluctuation amplitudes. When both instabilities are included in the model (right figure), the interaction results in even larger structures, that are now broader in the poloidal direction, too. Nonetheless, the average transport is lower in the standard case. A reason for this is given in section 6.4.2.

The same analysis has been performed for the potential fluctuations (Fig. 6.6). The results are very different: In the drift wave case, the fluctuations are dominated by poloidally extended perturbations, linked to poloidal $\mathbf{E} \times \mathbf{B}$ flows (cf. section 5.4.2). The MHD interchange case shows potential structures that closely resemble the density fluctuations, but are larger. In the standard run, the MHD interchange behavior dominates the perpendicular cross correlations.

Perpendicular cross correlations can also be obtained between different variables. Fig. 6.7 shows the correlation of the density fluctuations in the perpendicular plane with the potential fluctuations at the reference point. For the drift waves, the cross correlation does not exceed a value of 0.5. The maximum of this weak correlation is at the reference point, hence where density and potential maximum coincide. This is consistent with the linear picture of a drift wave as described in chapter 2. In MHD interchange turbulence, the existence of convective cells with a phase shift of $\pi/2$ between density and potential fluctuations can be confirmed. A potential maximum at the reference point correlates with a high density fluctuation on its upper side (convected down the gradient) and a low density fluctuation at its lower side. In the full model the coupling between drift wave and MHD interchange modes can

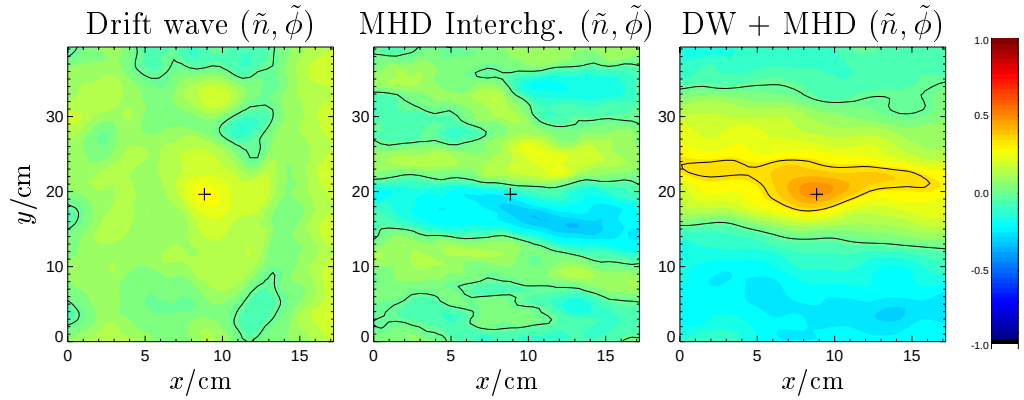

Figure 6.7 Perpendicular cross correlations for density fluctuations in the perpendicular plane with the potential fluctuations at the reference point for the three different runs.

be observed. Although the structure sizes are close to the MHD results, the cross correlations for the standard run are no longer dominated by convective cells. This is the reason why $\langle\Gamma\rangle$ and the mean fluctuation amplitudes are lower in the standard run.

6.3.3 Conditional averaging

The main goal of conditional averaging (CA) is the detection of coherent structures in space-time turbulence data. The algorithm is based on the assumption that the data consists of a coherent part x_c and a stochastic part, ξ, thus $u = u_c + \xi$. The condition $\mathcal{C}$ serves as a filter; events in u_c fulfilling the condition are taken into account, the stochastic noise vanishes in the averaging process with $\langle\xi\rangle = 0$.

$$C(x,y)^{\mathcal{C}}_{uv} = \frac{1}{N}\sum_{j=1}^{N} \mathcal{C} \cdot u(x,y,t_j) \tag{6.14}$$

The condition is expressed by $\mathcal{C}$. It is equal to one when the condition is fulfilled and zero otherwise. The simplest condition is $\mathcal{C}_1 = \delta(u(x,t) - u_0)$. To avoid counting events twice, only the ascending slope of a fluctuation is counted. This is expressed by $\mathcal{C}_2 : \Theta(\partial_t u(x,t))$, where Θ is the Heavyside step function. The full condition as used in this section reads $\mathcal{C} : \mathcal{C}_1 \cdot \mathcal{C}_2$. Throughout this section, only this kind of condition is used, and the threshold is expressed in units of the standard deviation. A value of $u_0 = 1.5\,\sigma$ has proven to be the best compromise between the statistical requirement to count a large number of events and the desire to capture only the large events [24].

In the two-field model of the turbulence simulation, the condition can be imposed on either variable. This creates an data analysis tool with phase sensitivity: The method is able to detect fixed phase relations of events at different points,

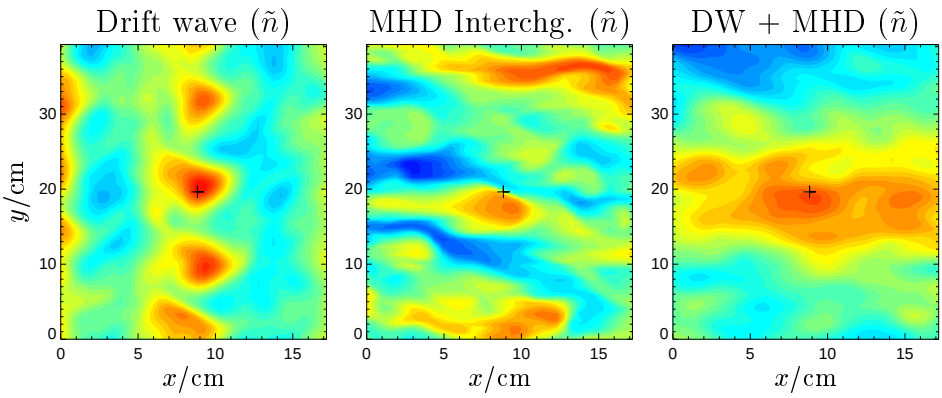

Figure 6.8 Conditional averaging for the density fluctuations in the three runs. The condition was fixed to $\tilde{n} > 1.5\,\sigma_n$ in the increasing flank of an event.

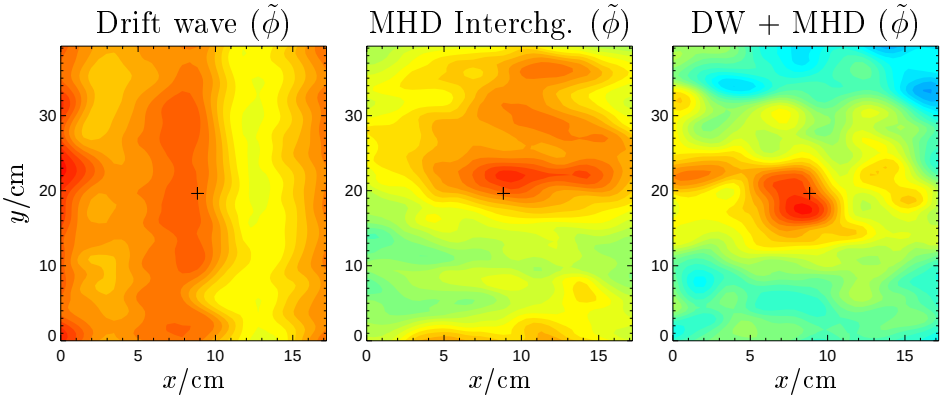

Figure 6.9 Conditional averaging for the potential fluctuations in the three runs. The condition was fixed to $\tilde{\phi} > 1.5\,\sigma_\phi$ in the increasing flank of an event.

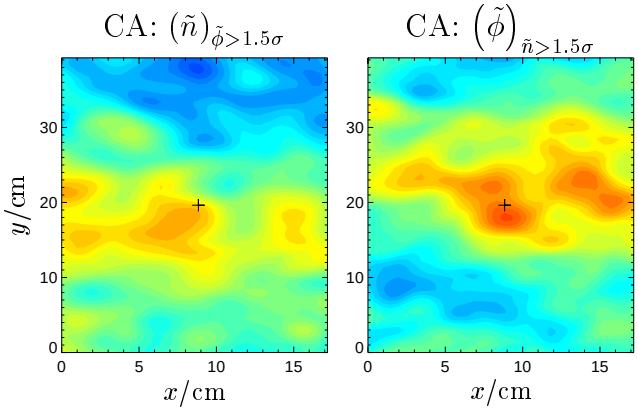

Figure 6.10 Different conditions compared for the density and potential fluctuations. The figures have been obtained from the standard run.

by fixing the condition on an density maximum and averaging over the potential structure in its surroundings.

We have seen in section 6.3.2, that the cross correlation overestimates structure sizes. Conditional averaging provides a tool that reduces this effect [24]. The downside of conditional averaging is the amount of data that is required for an analysis. The condition severely lowers the number of data points that are available in the averaging process, leading to a higher statistical uncertainty.

Physical interpretation and results Results from conditional averaging are shown in Fig. 6.8 for the density fluctuations and in Fig. 6.9 for the potential fluctuations. The reference point where the condition is checked is marked by a cross. The main features from the cross correlations are reproduced, but with smaller structures having a higher contrast. This is due to the fact that the small amplitude fluctuations do not smear out the result as it is the case for the correlation functions. In the drift wave run, a periodicity with a wavelength of $\lambda = 11\,\mathrm{cm}$ is observed in the drift direction. A similar periodicity shows up in the MHD case, with $\lambda = 15\,\mathrm{cm}$. Such waves are a feature of the linear models, and are only reproduced for the reduced equation sets. The standard run with MHD and drift wave in interaction does no longer show any periodicity in the poloidal plane. The potential structures (Fig. 6.9) obtained by CA do not provide additional information to the results from the correlation analysis (Fig. 6.5).

Fig. 6.10 demonstrates how different conditions affect the result of CA. The left figure shows the density fluctuations, with the condition placed on $\tilde{\phi}$. A small shift between density and potential fluctuations is observed in the poloidal direction. Since the averaging is done over $\tilde{n}$, the size of the structure is the same as in Fig. 6.8. The right figure shows the potential fluctuations under the condition imposed on the density. In conditional averaging, the structures of the averaged variable determine the result, regardless of the condition. When the averaging is done over the potential fluctuations, the result will have the (averaged) properties of the potential fluctuations. Consequently, the right part of Fig. 6.10 has the typical length scale of the potential fluctuations. A poloidal shift with respect to the potential maximum at the reference position (where the condition is imposed) is visible. In the right part of the figure, the averaging yields large structure of the size of the potential fluctuations. Hence, the shift is not as clearly resolved. Nonetheless, the center of the fluctuation structure lies over the reference point. These two observations are consistent as they both show an average shift between the two fluctuating quantities. This indicates a (weak) average phase shift between density and potential fluctuations in the standard run.

6.4 Fourier methods

Fourier methods are very common tools for data analysis [73, 48]. Although the Fourier transform of a signal is rigorously defined, the results from Fourier analysis have to be regarded as statistical properties. To obtain meaningful results, an statistical ensemble of data has to be regarded. In practice, this is rather difficult since complete statistical independence between these ensembles is required. To generate an ensemble from space-time data, it is common practice to use time series sampled at different locations, or spatially resolved variables at different time steps. These are, however, not statistically independent. The short correlation time (or length), compared to the size of the simulation volume, however, justifies this approach. Throughout this section we will come back to the concepts of the K41 theory (cf. section 5.1).

6.4.1 Fourier transform and power spectrum

Power spectra describe how energy is distributed over waves with different frequencies $f = \omega/2\pi$ or wave numbers k. The power spectrum is obtained as the modulus of the Fourier transform of the signal; it can be calculated for wave numbers, frequencies and as a 2D power spectrum. The power spectrum $P(k)$ of a signal $u(x)$ is defined as the absolute square of its (complex) Fourier transform,

$$\hat{u}(k) = \mathrm{FT}(u(x)) = \int_X u(x) \cdot \exp(ikx)\,\mathrm{d}x \tag{6.15}$$

$$P(k) = |\hat{u}(k)|^2 . \tag{6.16}$$

The hat marks a Fourier transformed variable. Experimental data is discrete in time and space, hence a discrete Fourier transform algorithm has to be used. The numerical algorithm used is the very efficient *Fast Fourier Transform* (FFT) [52]. A consequence of discrete data is a finite resolution in frequency [52]. Frequencies higher than the Nyquist frequency $f_{Ny} = 1/(2\Delta t)$, where Δt is the time between two subsequent samples, cannot be resolved. A similar limit $k_{Ny} = 1/(2\Delta x)$ exists for k spectra. Frequencies beyond the Nyquist limit are mirrored back in frequencies below f_{Ny}. This effect is called "aliasing".

An important perquisite for a Fourier transform is that the data is periodic. (The simulation data is periodic in the y direction, but not in t, see section 4.4.2). When applied to aperiodic data, the Fourier transform introduces artifacts. This can be prevented by a process called windowing, where the data is point wise multiplied by a function that goes to zero at both ends of the window. The Hamming window [52] is used for the time depended fluctuations. In the y direction, the simulation results are periodic and no windowing is needed. To enhance the statistical significance of the results, the ω spectra are averaged over the points in the perpendicular plane, and the k_y spectra are averaged over the time steps.

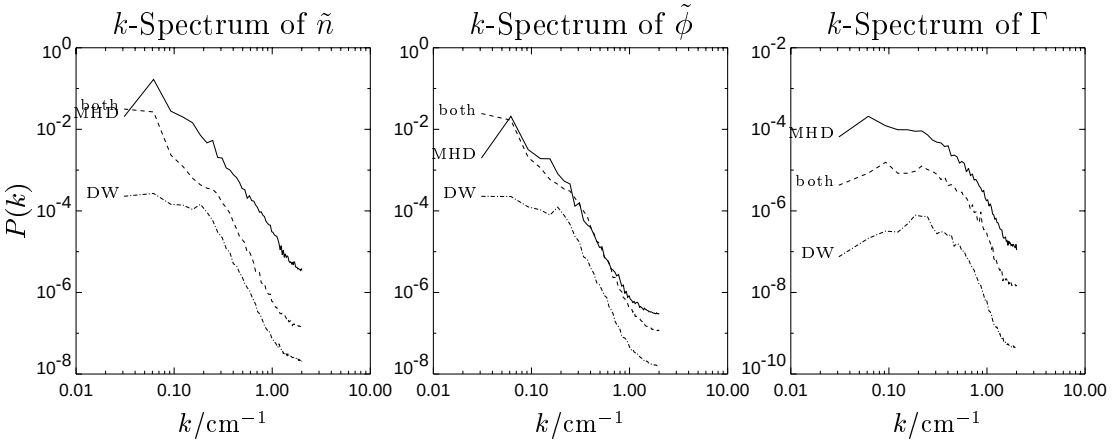

Figure 6.11 Power spectra for the density, potential and transport fluctuations for the three different simulations.

The Wiener-Khinchine theorem The power spectrum $P(k)$ and the autocorrelation function $C(\Delta x)$ contain the same information and are linked by the Wiener-Khinchine theorem [73],

$$C(\Delta x) = \frac{1}{2\pi} \int_X P(k) \cdot \exp(ik\Delta x)\, \mathrm{d}k\,. \tag{6.17}$$

This means that the autocorrelation function and the power spectrum are their mutual Fourier transforms.

Physical interpretation and results The k spectra from a spatial Fourier transform of the potential, density and transport fluctuations are shown in Fig. 6.11. The density spectra for MHD interchange turbulence scales with $\alpha = -3.9$, the drift wave run has $\alpha = -5.1$ in the high-k_y region. The standard run reproduces the drift wave scaling in the small structures, but with a continuing cascade towards larger structures. The overall fluctuation amplitudes behave according to the standard deviation as shown in Tab. 6.1: While the drift wave turbulence has the lowest amplitudes, the MHD interchange instability produces the most violent fluctuations. The standard system is placed in between the two. An exception is given by the potential fluctuations, where the standard system attains the fluctuation level of the MHD-only run.

For larger scales with $k_y < 0.2\,\mathrm{cm}^{-1}$, the spectra differ qualitatively. This is most evident in the density fluctuations: For drift wave turbulence, the fluctuation amplitudes at low wave numbers are almost constant, reminding of a "injection range" as it was defined in the K41. For MHD interchange turbulence, the scaling extends to lower wave numbers, which have a higher (relative) amplitude. Since the MHD interchange instability corresponds to a 2D system, this is a result of the inverse cascade dynamics, transporting energy to the larger scales. This behavior is also found in the transport spectra: The maximum transport for the drift wave is in the intermediate scales,

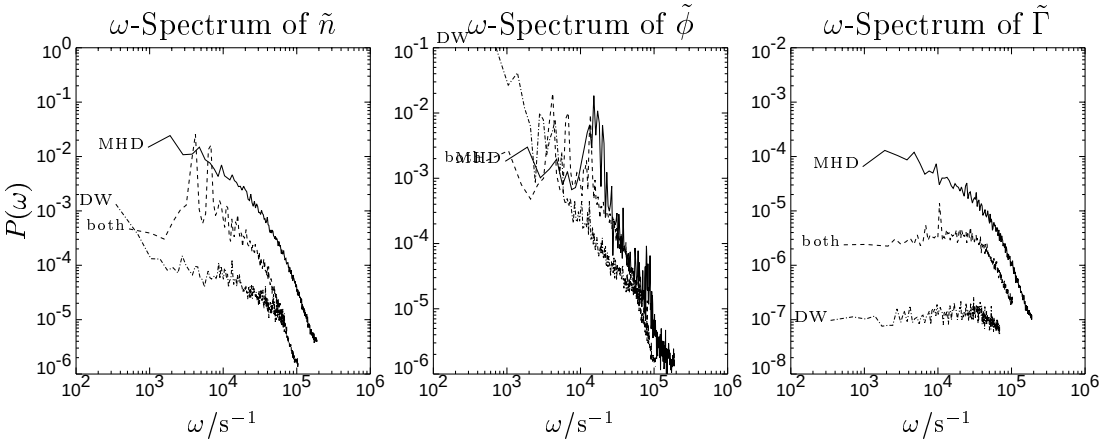

Figure 6.12 Power spectra in ω for the density, potential and transport fluctuations for the three different simulations.

where it is at the maximum scales for MHD interchange turbulence. On all scales, the standard system exhibits an intermediate fluctuation amplitudes, with a density and potential spectrum that is more like MHD, and a transport spectrum closer to the drift wave case.

Fig. 6.12 shows the ω spectra for density and potential fluctuations. Again, the variation of the fluctuation amplitudes applies to all frequencies. The drift wave $\tilde{\phi}$ spectrum shows a peak for low frequencies $\omega \to 0\,\mathrm{Hz}$. This peak is associated with long-living poloidal structures that have been discovered by correlation analysis and conditional averaging. Because no poloidal gradient $\partial_y \phi$ is associated with these structures, they do not lead to $\mathbf{E} \times \mathbf{B}$ transport and show not up in the Γ spectrum. Such a peak does not show up in the MHD run.

6.4.2 Phase spectra

The phase of a signal itself is of little use, unless the data analysis has a fixed time scale where $t = 0$ corresponds to a specific event. In turbulence data analysis, this is not the case. However, the relative phase of two fluctuating variables is an important number in plasma dynamics. We refer the reader to sections 2.2.4 and 2.2.5 for a discussion of how the phase relation between density and potential fluctuations can be used to discriminate the different micro-instabilities. The phase φ between two (poloidal) modes $u_1(y)$ and $u_2(y)$ of wavenumber k_0 is called the cross phase. It can be calculated for each time step [60],

$$\begin{aligned} u_1 &= C_1 \exp(ik_0 y) \\ u_2 &= C_2 \exp(ik_0 y) \\ \varphi(k_0) &= \varphi(C_1) - \varphi(C_2) = \ln \frac{\hat{u}_1^0(k)}{\hat{u}_2^0(k)}\,. \end{aligned} \tag{6.18}$$

with $\hat{u}_i^0(k) = \hat{u}_i(k)/|\hat{u}_i(k)| = |C_i|$. The hat denotes the Fourier transform. Expressed in terms of wave numbers k_y in the poloidal direction and for variables n_t and ϕ_t at time step t, we have

$$\varphi_{n,\phi,t}(k_y) = \ln\left(\frac{\hat{n}_t(k_y)}{\hat{\phi}_t(k_y)}\right) , \tag{6.19}$$

where the logarithm of a complex number yields its phase angle. A φ_t can be computed for each wavenumber k_y and each time step t. When averaged over the time, a probability distribution of the phase shift is obtained for each wavenumber. This probability distribution function (PDF) is plotted using a color table. The possible range for the phase shift is $\varphi \in [-\pi, \pi]$; φ is plotted over the wavenumber k_y. The result allows to look at the phase shift between density and potential fluctuations for each given wavenumber. A similar expression can be defined in ω space by exchanging the spatial and temporal directions in the definition (6.19).

Physical interpretation and results Fig. 6.13 shows the k_y resolved phase shift distribution between density and potential fluctuations. The left part shows the result from the drift wave-only model: The cross phase of $\tilde{n}$ and $\tilde{\phi}$ is close to zero for all wave numbers. This is in good agreement with the linear model from chapter 2. The middle part of the figure shows results from the MHD interchange model. Again the result fits well the mechanism of chapter 2: The phase shift is centered around $\pi/2$ as predicted. The different phase shift for the two instabilities allows us to explain the difference in transport that was first discussed in section 6.3.1. It is in good agreement with the findings from the correlation functions (section 6.3.2) and conditional averaging (section 6.3.3), where convective cells have been detected. These cells are very efficient transport mechanisms.

In the right part of Fig. 6.13 the superposition of both instabilities can be observed. The phase shift is closer to the drift wave model than to the MHD model, but with a broader phase distribution. This leads to larger overall transport, as observed in section 6.3.1. For larger wave numbers, a systematic change of the phase shift is observed. This phase shift is in the direction of $\pi/2$ and caused by the curvature driven MHD interchange instability. It is the source of transport at low wave numbers of the k_y spectra shown in Fig. 6.11. However, this phase shift is too low to be observed in the perpendicular cross correlations. In section 6.3.2, convective cell structures could not be observed in the standard run.

6.5 Summary and discussion

Drift wave turbulence From the analysis of the drift wave-only simulation it is learned that the drift instability is enough to drive the system into fully developed turbulence, as it can be seen from the fluctuations in the perpendicular plane.

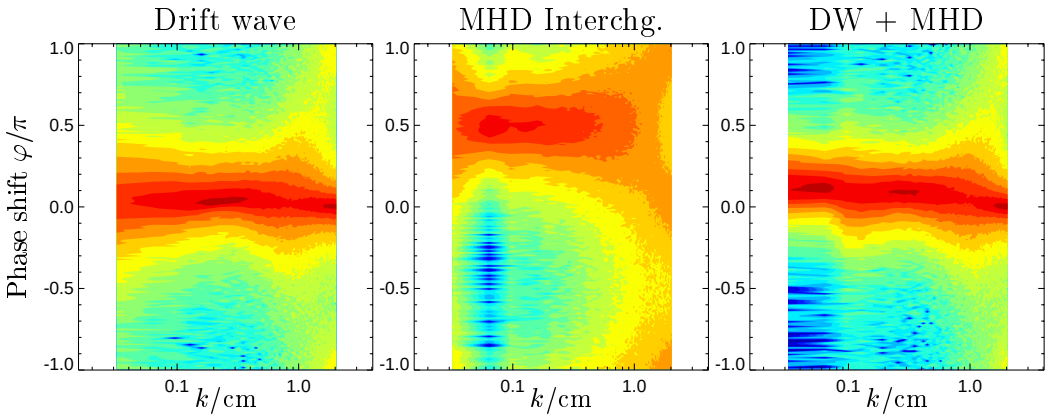

Figure 6.13 Phase shift distribution between density and potential fluctuations MHD and drift wave turbulence.

The power spectrum of the density and the potential fluctuation exhibits a self-similar scaling law with a scaling exponent $\alpha = -5.1$. This is much stronger than the exponents predicted by conventional fluid theory. In section 5.1, a scaling exponent of $-5/3$ is given for a three dimensional system, and -3 is given for 2D fluid turbulence. Density and potential fluctuations follow a Gaussian distribution, the transport fluctuations are intermittent, but close to symmetric. The spatial analysis of structures by conditional averaging yields the picture of a wave-like structure in the density fluctuations with a wavelength of $\lambda = 11\,\mathrm{cm}$. The potential fluctuations are dominated by modes with a poloidal wave number $k_y = 0$, and a low oscillation frequency ω. These large scale potential fluctuations are poloidal flows, excited by Reynolds stress (cf. section 5.4.2). The typical mechanism for their decay into a geodesic acoustic mode should not be present because the drift wave-only situation does not contain curvature. This might be the reason why zonal flows are that clearly developed in this case. A correlation between density and potential fluctuations can be observed in the perpendicular plane. This corresponds to a phase shift close to zero in a wave-picture, a result that is confirmed by the wavenumber-resolved phase shift distribution. It shows that the small phase shift between density and potential fluctuations applies not only to large structures, but to all scales. All these results support the concept of density and potential fluctuations tied together by the fast parallel dynamics.

MHD interchange turbulence Already the raw space-time data for the MHD interchange turbulence in the perpendicular plane show a different behavior. The fluctuating eddies are larger. The amplitude distribution of density and potential fluctuation is Gaussian, similar to the drift wave case. The transport fluctuation PDF is sharply peaked, and has a strong asymetry not observed in the drift wave case. The kurtosis of the transport fluctuation is higher, too, indicating a larger radial extent of the transport events. By conditional averaging and cross

correlation we find much larger structures than in drift wave turbulence, for both density and potential fluctuations. This is probably due to the inverse cascade dynamics which is much more active in interchange than in drift wave turbulence, leading to energy transport to larger scales. The scaling exponent for the energy fluctuations is $\alpha = -3.9$, which is different from Kraichnans prediction for the inverse cascade [35]. It is observed that the potential fluctuations are larger than the density fluctuations. The inverse cascade is mainly acting on the vorticity (and hence the potential). The inspection of the cross correlations between density and potential indicate that the main mechanism in the turbulence are convective cells, with a characteristic phase shift of $\pi/2$ between $\tilde{n}$ and $\tilde{\phi}$. The size of the convective cells can be seen from the size of the density structures. The wave number resolved phase shift distribution reveals that the phase shift is centered around $\pi/2$ for all wave numbers. The effectiveness of convective cells as a mechanism for turbulent transport explains the significantly higher values for $\langle\Gamma\rangle$ as well as the increased kurtosis of the transport PDF.

MHD interchange and drift wave in interaction In the analysis of the standard run, basic properties of the two instabilities can be found. In the scale-separating diagnostics such as the k_y resolved phase shift and the power spectra, the standard system reproduces the properties of the drift wave model for small scales. The scaling exponent of the standard run matches the one of the drift wave run for the small structures. At larger scales $k_y < 0.2\,\mathrm{cm}^{-1}$, the signature of the MHD interchange instability shows up. Contrary to the drift wave case, the scaling in the power spectra continues to lower wave numbers, and MHD like convective cells contribute to the transport. That this transport is indeed due to the MHD interchange instability can be seen from the phase shift distribution, where a systematic, larger phase shift can be observed for these large structures only. Consequently, the diagnostics which are unable to separate scales, such as the correlation functions and conditional averaging, still give results that resemble MHD turbulence, as the large structures obscure the drift dynamics of the small scales.

Throughout all diagnostics, the standard run with the full dynamics exhibits drift wave properties at small scales. In this properties, the predictions of the linear pictures are found. MHD interchange signatures only show up at large scales. How the mix of drift wave and MHD interchange features change with plasma parameters is investigated in the next chapter.

7 Parameter studies

This chapter examines the influence of several quantities on the turbulence. Here, the full model is used throughout all studies. These quantities can be divided into two groups: First the influence of the magnetic field structure is studied. The field line curvature enforces the MHD interchange turbulence, and it is expected the local magnetic shear tames the turbulent fluctuations. In chapter 4.2 it has been shown that the range of the normalized plasma parameters can be varied in TJ-K. The second section of this chapter will investigate the changes in the turbulence micro-structures when the normalized parameters are varied. A sweep in $\hat{\beta}$ and in $\hat{\nu}$ is discussed. The results from this section are especially important to an experiment-simulation comparison.

7.1 Influence of the geometry

The magnetic field geometry influences the turbulence by two effects. The field line curvature couples the fluctuations to the background density gradient, leading to the MHD interchange instability. Because the curvature has opposite signs on the high and low field side, differences are expected between the fluctuations at different poloidal locations. Furthermore, the local shearing of the magnetic field is expected to damp the turbulence. Both effects are investigated in the next sections using a simulation run with $\hat{\beta} = 0.75$, $\hat{\nu} = 4.0$ and $\hat{\mu} = 0.3$. In physical units, this is TJ-K operated with Helium gas at $n = 2.5 \times 10^{18}\,\mathrm{m}^{-3}$, $T_e = 21\,\mathrm{eV}$ and $B = 0.2\,\mathrm{T}$. The resulting drift scale is $\varrho_s = 0.5\,\mathrm{cm}$. The metric coefficients used for the runs in this chapter can be found in Tab. 4.3.

7.1.1 Curvature effects

The magnetic field line curvature drives the MHD interchange instability. Its signatures, as observed in the previous chapter, are large, radially elongated structures, high fluctuation amplitudes in the low-k_y regime of the power spectrum and a characteristic phase shift between density and potential fluctuations of $\pi/2$. In section 4.4, it has been shown that in a flux tube coordinate system the magnetic curvature varies along the z axis. Where the flux tube passes the low field side, the curvature is unfavorable, i. e. the MHD interchange modes are unstable. On the high field side, these modes are stable. The fast parallel Alfvén dynamics connects the two locations in the direction of the magnetic field. The subsequent data

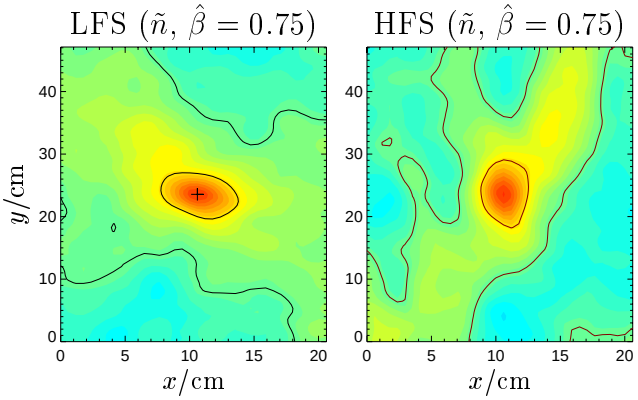

Figure 7.1 Perpendicular cross correlations at the high field side (HFS) and the low field side (LFS) for the density fluctuations.

analysis investigates the interplay between the varying curvature and the parallel dynamics. Two perpendicular planes, as described in section 6.2, are analyzed. One of them is placed at the high field side (HFS) of the flux tube, the other one at the low field side (LFS). Fluctuating variables from the HFS are marked by a subscript H, the low field side is indicated by a L. The discussion of the turbulence is organized as in chapter 6.

The amplitudes of the density fluctuations, in units of $\tilde{n}/n_0$ are $\sigma_{n,H} = 0.15$ and $\sigma_{n,L} = 0.21$. The ratio of the fluctuation amplitudes on the high and low field side will be referred to as the ballooning factor $\mathcal{B}$ in the further.

$$\mathcal{B}_u = \frac{u_L}{u_H} \tag{7.1}$$

Its value is 1.4 for the density fluctuations. The potential fluctuations are $\sigma_{\phi,H} = 0.43$ and $\sigma_{n,L} = 0.42$, with a ballooning factor of almost one. The transport fluctuations are $\sigma_{\Gamma,H} = 0.0046$ and $\sigma_{\Gamma,L} = 0.010$, with a ballooning factor $\mathcal{B} = 2.17$. The average transport is $\langle \Gamma_H \rangle = 0.00122$ and $\langle \Gamma_L \rangle = 0.00032$, with $\mathcal{B} = 3.76$. This is larger than the product of density and potential ballooning factors, indicating that a parameter other than the fluctuation amplitudes enters the transport, namely the phases.

The poloidal cross correlation functions for the high and low field side of the plasma are shown in Fig. 7.1. The correlation lengths are of the order of several centimeters, and the events are not radially elongated. This is the signature of the drift instability. The MHD interchange instability is not expected to be dominant at $\hat{\beta} = 0.75$. The radial correlation of the structures decays somewhat faster on the high field side, but the poloidal correlation length is enlarged.

At a higher values of $\hat{\beta} = 2.75$, large radial events are observed on the low field side. Results from such a run are shown in Fig. 7.2; the large radial structures on the low field side are one of the signatures of the MHD interchange instability.

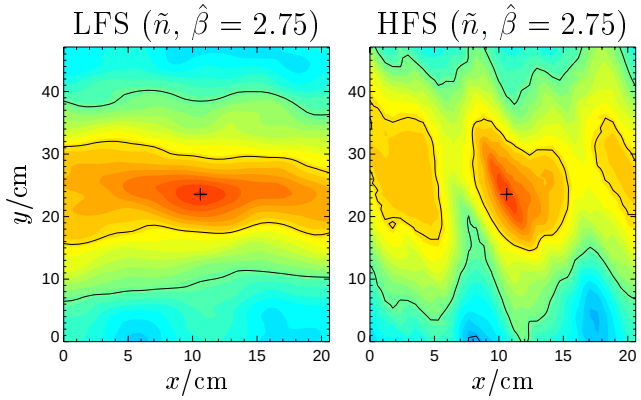

Figure 7.2 Perpendicular density cross correlations at the high field side (HFS) and the low field side (LFS) at $\hat{\beta} = 275$.

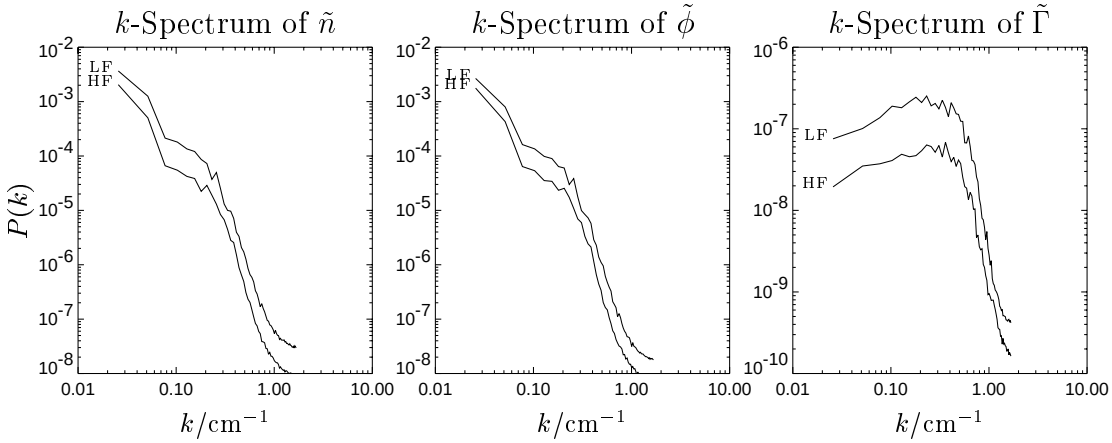

Figure 7.3 Power spectra for the density, potential and transport fluctuations for the high and low field side of the plasma, obtained at $\hat{\beta} = 0.75$.

The difference between high and low field side becomes stronger, and the structures on the high field side are much smaller in the radial direction, but therefore smeared out in poloidal direction. As the cross correlation is normalized to the standard deviations of the fluctuations, it does not reflect the different fluctuation amplitudes. On the low-field side the fluctuation amplitude are 1.4 times higher than on the high-field side.

Fig. 7.3 shows the power spectra for density, potential and transport fluctuations at the high and low field side. Since $\hat{\beta}$ is low, the drift instability is dominant. Although the MHD interchange instability is active, as it can be observed from the ballooning structure, it does not result in a qualitative change in the spectra. All wave numbers are equally ballooned. At a higher value of $\hat{\beta}$, shown in Fig. 7.4, this behavior does not change.

Looking at the phase shift distribution $\varphi_{\tilde{n},\tilde{\phi}}$ shown in Fig. 7.5, one finds that

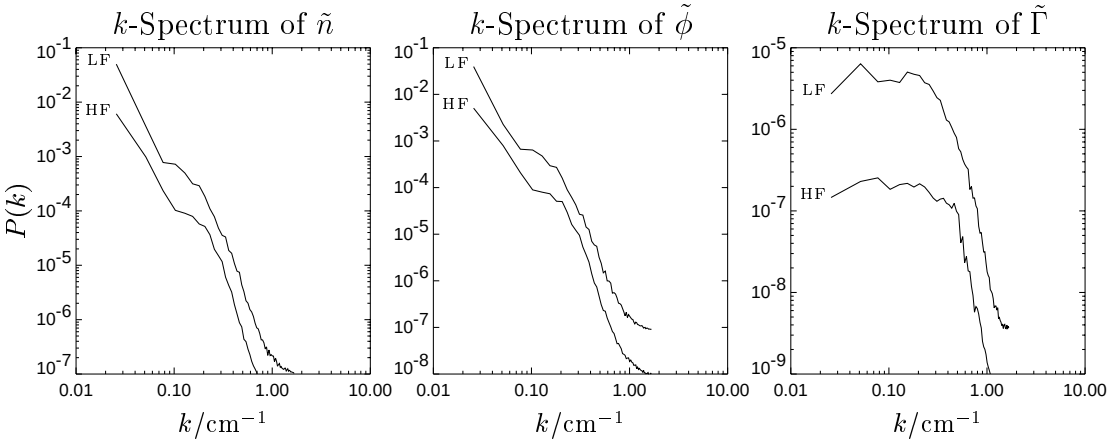

Figure 7.4 Power spectra for the density, potential and transport fluctuations for the high and low field side of the plasma, obtained at $\hat{\beta} = 2.25$.

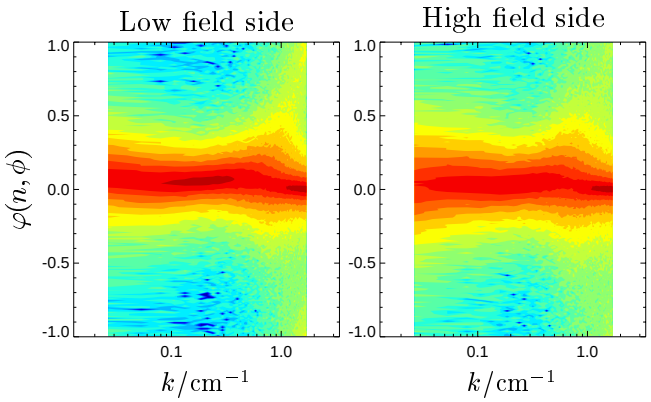

Figure 7.5 Phase shift distributions at the high field side (HFS) and the low field side (LFS) at $\hat{\beta} = 0.75$.

the phase shift between density and potential fluctuations does not vary between the high and low field side. This is not surprising for drift wave turbulence. Going to higher values of $\hat{\beta} = 2.75$, one finds that this effect is persistent. A figure is not shown here. To further drive the MHD interchange instability into a regime where it dominates the turbulence, the value for the field line curvature is enhanced to $\mathcal{K} = 0.5$, which is four times the value of TJ-K. In this run, shown in Fig. 7.6, the phase shift of $\pi/2$ shows up at large scales. Again, a comparison of the high and low field side yields a similar behavior at both poloidal positions. At the high field side, the phase shift distribution cannot be due to the curvature. When a potential perturbation grows into a large convective cell at the low field side, it propagates along the magnetic field line and induces a similar fluctuation on the high field side. The same effect is responsible for the drift-wave like shape of the phase shift distribution in the low beta case: the fast parallel Alfvén dynamics connecting

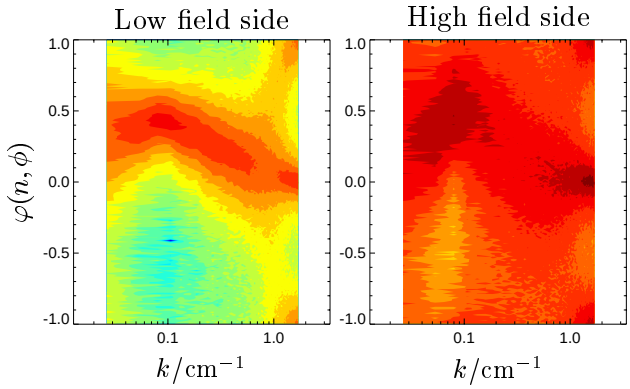

Figure 7.6 Phase shift distributions from a run with higher curvature $\mathcal{K} = 0.5$ and plasma parameters $\hat{\beta} = 2.25$, $\hat{\nu} = 4.0$, $\hat{\mu} = 0.3$.

high and low field side reduces the impact of the curvature driven instability and ties density and potential fluctuations together.

7.1.2 Local shear

In the torsatron TJ-K, the magnetic field geometry is marked by particular high values for the local magnetic shear. A simplified description of local shear has been added to the metric of DALF3 (cf. section 4.5). It is quantified by the parameter $\hat{s}_0$ (4.21). To investigate how a locally sheared magnetic field changes the turbulence, simulation runs were carried out using different values for the $\hat{s}_0$.

Fig. 7.7 shows how the turbulence reacts to weak local shear. A realistic description of TJ-K yields $\hat{s}_0 \approx 5$, leading to numerical instabilities in the code. Therefore, lower values for $\hat{s}_0$ have been used in this study. The first row of the figure shows the fluctuation levels (given by the standard deviation in normalized units) of $\tilde{n}$, Γ and the value of the average transport $\langle\Gamma\rangle$ at the high and low field side of the plasma. These values are plotted as a function of $\hat{s}_0$. On both high and low field side, the amplitudes of the density fluctuations first rise, as $\hat{s}_0$ is increased from zero to 0.75. This is contrary to the expectation that a sheared magnetic field leads to a decreased turbulence level. In Eq. 4.21, the addition of local shear results in an increase of the field line curvature $\mathcal{K}_y$, too. This is an indication for that the interchange instability in the turbulence is driven, leading to the higher fluctuation amplitudes. We will later see that this assumption is also supported by the phase shift distribution. For low values of $\hat{s}$, this effect is not yet compensated by the damping that results from the shear. As this shearing is further increased to $\hat{s}_0 = 1.5$, the decorrelation of the turbulent fluctuations becomes the dominant effect and reduces the fluctuation amplitudes. The transport Γ shows a different behavior: Its fluctuations go down continuously as $\hat{s}_0$ is increased. The average value $\langle\Gamma\rangle$ changes its ballooning structure. At low values

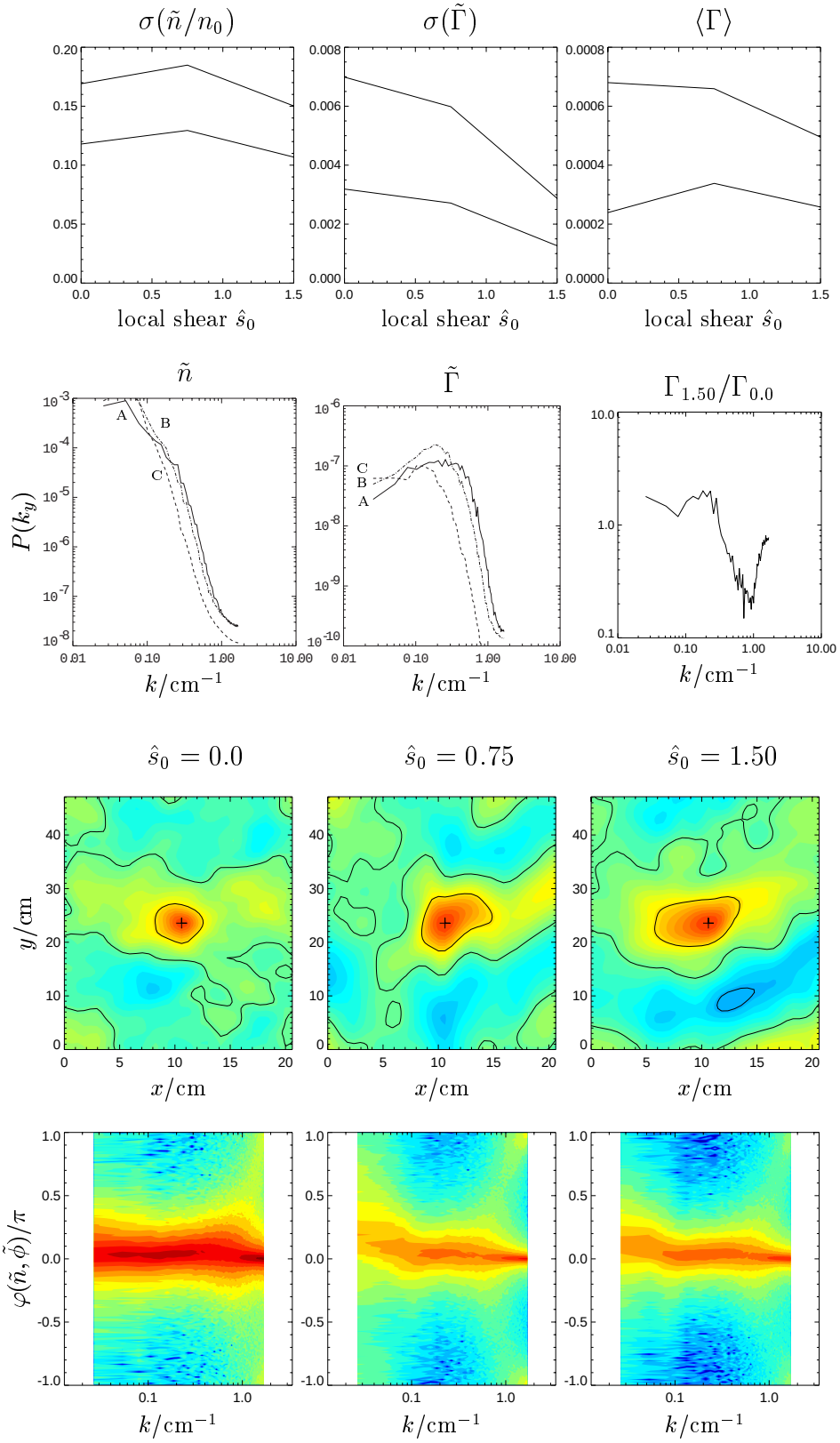

Figure 7.7 Local shear scan. From top to bottom: Fluctuation amplitudes, k_y power spectra, density cross correlations in the perpendicular plane and the phase shift distributions. A: $\hat{s}_0 = 0$, B: $\hat{s}_0 = 0.75$, C: $\hat{s}_0 = 1.50$.

of local shear, the average transport decreases at the low field side and grows at the high field side. The ballooning factor decreases from $\mathcal{B} = 2.8$ to $\mathcal{B} = 2.0$. This seems to be reasonable since with $\hat{s}_0$ an additional element is added to the field line curvature $\mathcal{K}_y$ (4.19) that does not distinguish between high and low field side. Now the data analysis tools developed earlier are used to further investigate the influence of local shear.

From the k_y power spectrum of $\tilde{n}$ it can be seen how the changes in the fluctuation amplitudes are distributed across the scales. The labels A to C are used to indicate the level of local shear in the simulation. Run A is with $\hat{s}_0 = 0.0$, B with 0.75 and C with 1.5. The introduction of local shear reduces the fluctuations on wave numbers larger than $0.25\,\mathrm{cm}^{-1}$, but increases the fluctuation for lower wave numbers. The same effect can be observed for the transport fluctuations: small scales are damped, and large scales are favored. This is quantified in the rightmost plot in the second row of Fig. 7.7, showing the ratio between the fluctuations in a field geometry with and without local shear: It is greater than one for $k_y < 0.25\,\mathrm{cm}^{-1}$, and smaller otherwise. Although the transport in the small scales is damped, the large structures experience the curvature and the interchange instability drives them stronger. It is important to keep in mind that the spectra have been obtained in the drift direction (poloidal in the experiment). A decorrelation and the reduction of structure sizes is expected in the *radial* direction. The effect competes with the radial elongation that results from the MHD interchange instability, therefore a slight overall increase in the radial structure size is observed.

The cross-correlations in the perpendicular plane (Fig. 7.7) reflect the growth in low poloidal wave numbers by growing structures. Although the curvature is the reason for the increase in the fluctuation amplitudes, the characteristic radially elongated transport events that have been detected in the previous sections do not show up. As the effect of the shearing is strongest for a structure which is radially elongated, this is probably due to the decorrelation in the magnetic field.

An analysis of the phase shift distribution shows a decrease in width for higher wave numbers. Due to this decrease the turbulent fluctuations can contribute less to transport. Only at the largest scales the phase distribution is broader and a systematic phase shift in the direction of $\pi/2$ is observed. This has been observed as a signature of the curvature drift in the previous chapter and is consistent with the change in the transport spectra.

7.1.3 Summary

It is commonly expected that the addition of local shear reduces the turbulence dynamics by radial decorrelation. A reduction of the fluctuations was indeed observed for the small scales of the fluctuations where the drift dynamics is dominant. At these scales, the transport reduction is attributed to the decreased

average phase shift. When density and potential fluctuations are in phase, it is the result of the parallel dynamics. Hence it seems that a change in this parallel dynamics is responsible for the decreased transport level, which is not yet understood. The diagnostics give the impression that local shear leads to a stronger coupling between density and potential fluctuations, and that its effects on the drift wave dynamics is comparable to an enhanced parallel conductivity. As an additional effect at low local shear a rise in the curvature driven MHD interchange instability was observed. It is open to investigation if this effect is an artifact of our definition for the model metric.

In an unsheared field geometry, neighboring field lines remain neighbors for the whole connection length. Local shear perturbs the "neighborhood relations" of field lines on a scale that is much shorter than the parallel length scale of the fluctuations. This connection blurs the structures in the poloidal direction, as it is observed in a poloidal enlargement of the perpendicular cross correlation functions.

7.2 Variation of plasma parameters

The main objective of this study is the investigation of characteristic turbulence properties that can be compared to experimental measurements. Absolute numerical values can serve as a guide, but are of limited precision due to the inaccuracy in determining the experimental plasma parameters. Since the plasma parameters in TJ-K can be varied in a vast range (cf. section 4.2), *scaling properties* in the statistical properties of the turbulence due to parameter variation provide a better starting point. This chapter discusses how two different parameter variations affect the turbulent fluctuations in TJ-K. The parameters are the normalized plasma beta, $\hat{\beta}$, and the normalized parallel resistivity, $\hat{\nu}$. The former increases the MHD interchange instability, and the latter destabilizes the drift waves. Results from parameter sweeps are presented, starting from $\hat{\nu} = 4.0$, $\hat{\beta} = 0.75$ at a value $\hat{\mu} = 0.3$ (Helium gas). Two series of simulation runs are discussed, one sweeping $\hat{\beta}$ from 0.75 up to 3.25, and the other ranging $\hat{\nu}$ from 2 to 12. The other plasma parameters are kept constant in the sweep. Both parameter ranges exceed the accessible range in TJ-K in order to make the changes in the turbulence more visible. Throughout this chapter, the simple tokamak metric is used. The results from this section are published in Ref. [42, 50, 49].

7.2.1 Variation of $\hat{\beta}$

The (normalized) ratio of kinetic to magnetic energy is described by the parameter $\hat{\beta}$ (3.27). When $\hat{\beta}$ increases, it is expected from the theoretical description that MHD interchange instabilities become more violent. The signatures of this

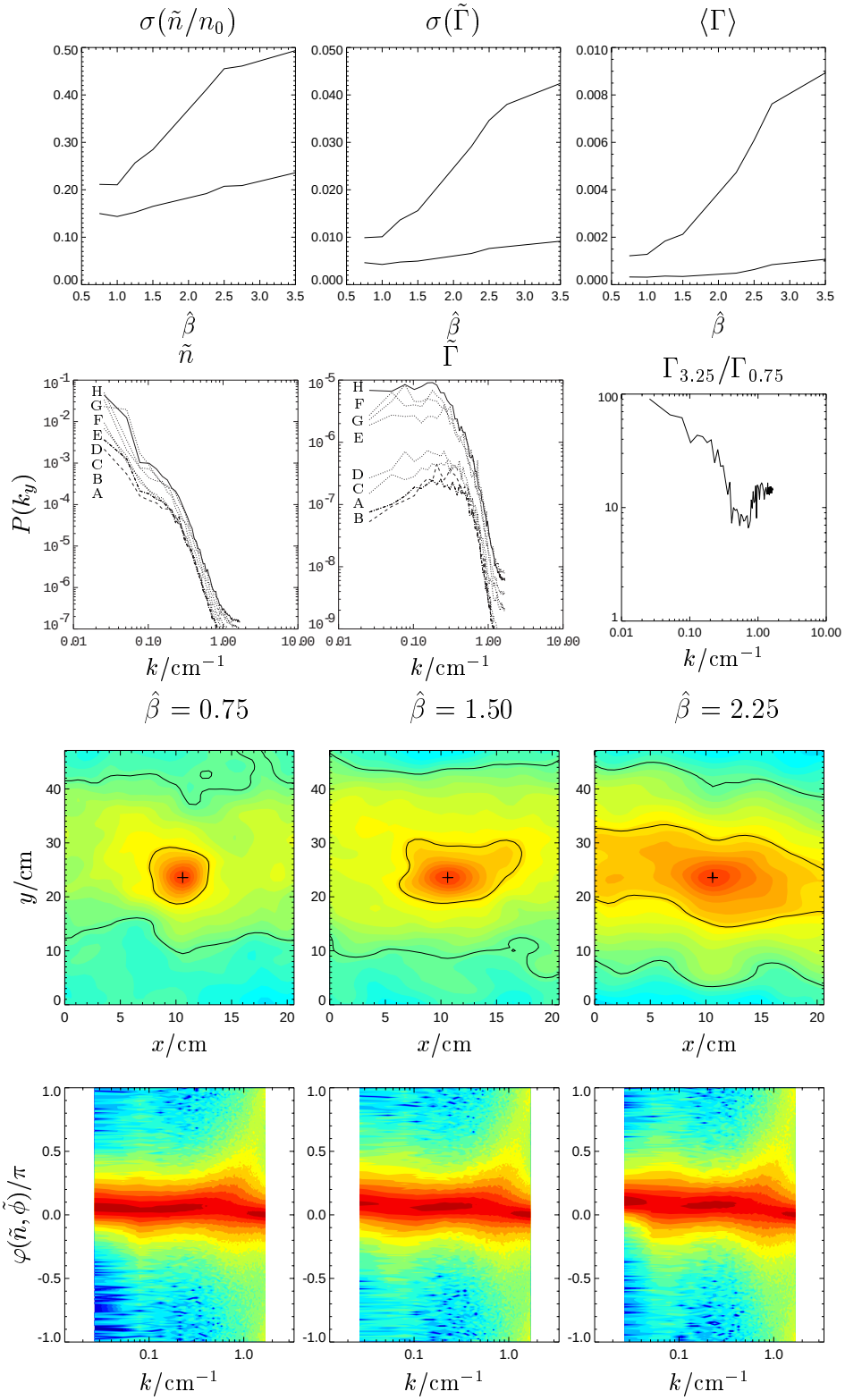

Figure 7.8 Results from the $\hat{\beta}$ sweep. From top to bottom: Fluctuation amplitudes, k_y power spectra, density cross correlations in the perpendicular plane and the phase shift distributions. A: $\hat{\beta} = 0.75$, B: $\hat{\beta} = 1.00$, C: $\hat{\beta} = 1.25$, D: $\hat{\beta} = 1.5$, E: $\hat{\beta} = 2.25$,F: $\hat{\beta} = 2.5$,G: $\hat{\beta} = 2.75$, H: $\hat{\beta} = 3.5$.

instability have been discussed in chapter 6; in this section the scaling of these signatures ins studied.

Results from the $\hat{\beta}$ sweep are shown in Fig. 7.8. The first line of the figure shows the statistical properties describing the fluctuation strength for $\tilde{n}$ and $\tilde{\Gamma}$, as well as the mean transport $\langle\Gamma\rangle$. With increasing $\hat{\beta}$, the density fluctuations become stronger at both high and low field side. The amplitudes range from $\tilde{n}/n_0 = 0.16$ and 0.21 for low $\hat{\beta}$ to 0.23 and 0.49 for high $\hat{\beta}$. The ballooning factor is $\mathcal{B}_n = 1.5$ for $\hat{\beta} = 0.75$, and $\mathcal{B}_n = 2.25$ for $\hat{\beta} = 3.25$. For the transport fluctuations, the ratios are $\mathcal{B}_\Gamma = 2.5$ and $\mathcal{B}_\Gamma = 4.6$, respectively; for $\langle\Gamma\rangle$, the ratio is 2.4 at low beta and 15 at high beta. The ballooning is most pronounced in the average transport and weakest for the density fluctuations. It increases with increasing $\hat{\beta}$, showing that the curvature as a coupling mechanism gains importance in the transition from drift wave to MHD interchange turbulence.

The density fluctuation power spectra shown in the second line of the figure show a cascade over all scales at all values of $\hat{\beta}$. At the low wave numbers, a stronger than proportional increase in the fluctuation amplitudes can be observed as $\hat{\beta}$ rises. The transport spectra show a cascade only for structures smaller than $0.2\,\mathrm{cm}^{-1}$. The amplitudes of the larger scales rise with increasing $\hat{\beta}$ and also show a qualitative change: at low $\hat{\beta}$, the intermediate scales at $k_y \approx 0.2\,\mathrm{cm}^{-1}$ dominate the transport. When $\hat{\beta}$ rises, the larger structures become more important, and the spectrum is constant for the low wave numbers at $\hat{\beta} = 3.25$. The rightmost figure in the second line of Fig. 7.8 shows the ratio of the transport fluctuations at $\hat{\beta} = 0.75$ and $\hat{\beta} = 3.25$. It confirms the observation that the increase in transport fluctuation amplitudes is most important for the large structures. Consequently, an significant enlargement of the structures is expected in the perpendicular cross correlations in the third row of the figure. In addition to an enlargement of the structures in the poloidal direction, the structures become radially elongated. This has already been observed in the MHD run in chapter 6, where it was named as one of the signatures of MHD interchange turbulence. The radial elongation grows stronger than the poloidal one. The events correspond to convective cells in which a large amount of plasma (measured by the increased density fluctuation amplitude) is transported over a long distance. This leads to the drastic increase in transport, and to a higher kurtosis in the density PDF.

The average phase shift (last row of Fig. 7.8) shows only little variation, even for high values of $\hat{\beta}$. This indicates that the parallel drift wave dynamics is still very strong in the parameter regime under observation. Only for the largest structures a slight increase of $\varphi(\tilde{n}, \tilde{\phi})$ is observed. This is a signature of the insetting MHD instability and one of the reasons for the increase of the transport at low wave numbers.

Over all the numerical diagnostics, a consistent picture of insetting MHD interchange instability can be drawn: The rise of the normalized plasma beta leads

to an increasing turbulence level on all scales. A closer look at the power spectra shows that the largest scales are affected most by the increased instability induced by $\hat{\beta}$. A result from chapter 6 was that MHD interchange turbulence goes to large scales due to the inverse cascade dynamics. This effect becomes stronger and leads to increased fluctuation amplitudes for large structures. This can also be observed in the perpendicular plane, where the cross correlations indicate growing structures. The radial elongation of these structures is linked to convective cell dynamics. The (slight) increase in the average phase shift is also a signature of this. Since the coupling mechanism in MHD interchange turbulence is magnetic field curvature, the ballooning structure of the fluctuations becomes stronger as $\hat{\beta}$ goes up and MHD interchange dynamics becomes more important. Although all diagnostics clearly show the signs of MHD interchange turbulence as they where observed in the MHD run of the previous chapter, the k_y resolved phase shifts reveal that the parallel drift dynamics still provides a strong coupling between density and potential fluctuations.

7.2.2 Variation of $\hat{\nu}$

Fig. 7.9 shows the results from a sweep in $\hat{\nu}$. The data layout is identical to the layout of the beta sweep in Fig. 7.8. Increasing fluctuation amplitudes for $\tilde{n}$ are observed as $\hat{\nu}$ is increased (first row of the figure). The increase is not as drastically as in the $\hat{\beta}$ scan: At low $\hat{\nu}$, the fluctuations are $\tilde{n}/n_0 = 0.11 - 0.16$ of the background density, ranging up to 0.22 and 0.30 for $\hat{\nu} = 12$. Both transport fluctuations and mean transport go up as well. The ballooning coefficient decreases only slightly from $\mathcal{B}_n = 1.4$ to $\mathcal{B}_n = 1.36$ as $\hat{\nu}$ increases. A similar behavior is observed in the transport fluctuations, where $\mathcal{B}$ changes from 2.6 to 2.23. For the average transport, the numbers are $\mathcal{B}_{\langle\Gamma\rangle} = 6.0$ and $\mathcal{B}_{\langle\Gamma=3.5\rangle}$. As the increase of $\hat{\nu}$ is expected to destabilize the drift wave, this effect can easily be explained. This instability does not rely on the curvature, and its growth is therefore constant along the parallel direction. The drift instability has $\mathcal{B} = 1$ and consequently, the overall ballooning factor goes down as a constant fluctuation amplitude adds to ballooned one.

The power spectra in the second row of Fig. 7.9 give insight how the rise in the fluctuations in distributed across the scales. For the density fluctuations, the increase is weak and comparable for all wave numbers, the turbulence becomes stronger on all scales. The transport fluctuations also grow, but the spectra change their shape. The intermediate and small wave numbers $k_y > 0.2\,\mathrm{cm}^{-1}$ experience the strongest increase and lead to a maximum in the $\tilde{\Gamma}$ spectrum. The ratio of the fluctuations for $\hat{\nu} = 0.75$ and $\hat{\nu} = 12.0$ shown in the right column of the second row of Fig. 7.9 confirms this: The transport increases by a factor of 10 at $k_y > 0.15\,\mathrm{cm}^{-1}$, in contrast to five for the larger structures.

The perpendicular density cross-correlations *shrink* with $\hat{\nu}$. The extent of a

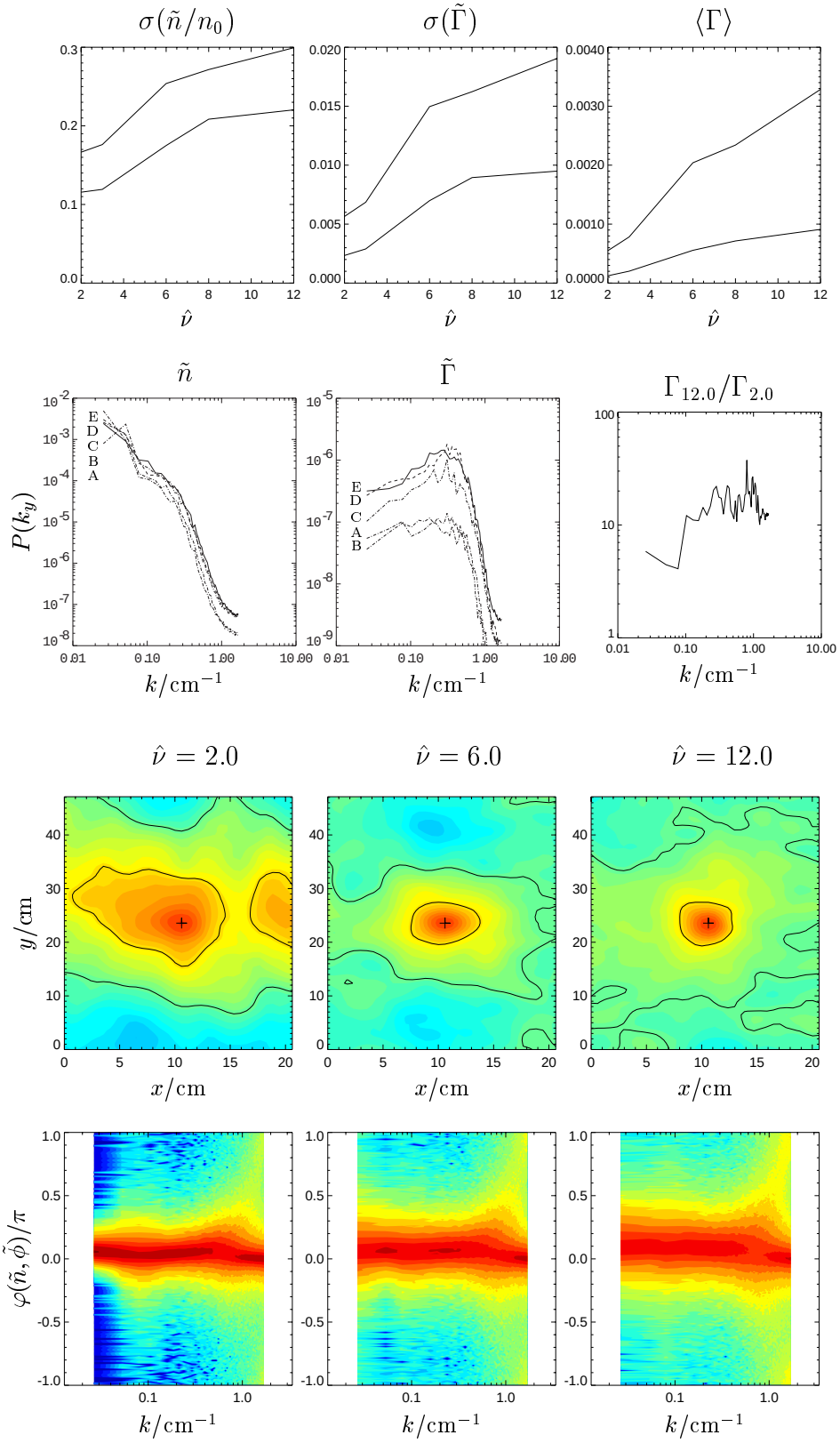

Figure 7.9 From top to bottom: Fluctuation amplitudes, k_y power spectra, density cross correlations in the perpendicular plane and the phase shift distributions. A: $\hat{\nu} = 2$, B: $\hat{\nu} = 3$, C: $\hat{\nu} = 6$, D: $\hat{\nu} = 8$, E: $\hat{\nu} = 12$.

typical turbulence event decreases in both the poloidal and radial direction. It is counterintuitive that a rise in transport is accompanied by a shrinking of the structures, as one would expect larger transport events. The reason for the increase in transport is found in a broadening of the phase shift distribution [50]. Furthermore, the cross correlation functions are normalized to the fluctuation amplitudes, so that a direct comparison of the structure sizes is misleading. A higher collision rates, the fluctuation amplitude is much higher, and an increased kurtosis, from $K = 0.16$ at $\hat{\nu} = 2$ to 0.37 for $\hat{\nu} = 12.0$, consistently indicates that the relative frequency of large amplitudes has grown. The phase shift distribution in the lowest row perfectly reproduces the expectations from the linear model: The linear theory predicts a larger phase shift when the parallel mobility decreases. In the figure, this results in a broadening of the phase shift distributions, indicating that the deviations from the stable $\varphi = 0$ become larger with increasing resistivity. This increase affects all wavelengths similarly.

The results from the statistical analysis of the $\hat{\nu}$ sweep show that the drift instability triggered by increasing $\hat{\nu}$ favors the small scales. Drift wave turbulence has its transport maximum at the intermediate and small scales. As these scales gain importance, it is observed that the perpendicular correlation length decreases.

7.2.3 Conclusions

The linear theory predicts that both the normalized plasma beta $\hat{\beta}$ and the normalized parallel resistivity $\hat{\nu}$ drive the turbulence. This is verified in the simulation. Under the $\hat{\beta}$ scan, the density fluctuation amplitudes grow by a factor of two, and the average transport grow by a factor of 4.3. The MHD interchange instability relies on the field curvature to extract energy from the background gradient. Consequently, the ballooning factor $\mathcal{B}$ increases as $\hat{\beta}$ goes up.

An increase in the normalized parameter $\hat{\nu}$ drives the drift wave stronger. This instability is evenly distributed along the field line. The density fluctuations increase by a factor of 3.2, the average transport increases by a factor of 3.5 in the $\hat{\nu}$ scan. As the drift wave induced fluctuations grow, the ballooning factor decreases.

The fluctuation power spectra show that the two instabilities act on different scales. The augmenting MHD interchange instability drives the large scales most. This is the reason for the drastic increase in the transport, as it can be seen from the transport spectrum. By choosing a parameter set with a higher curvature, it has been shown that this is due to an increasing average phase shift. The poloidal structure of the turbulence changes from almost circular blobs to radially elongated transport events. Under strong curvature, these structures have been identified as convective cells with the according density and potential structures. In the parameter regime that is relevant for TJ-K, the average phase shift never becomes high enough for these structures to show up in the correlations. However, a systematic shift in φ is observed, which is sufficient for a significant increase in

the flux-surface averaged transport $\langle \Gamma \rangle$.

When the drift wave is destabilized by increasing $\hat{\nu}$, the small and intermediate scales grow most. As the correlation functions are linked to the power spectrum by the Wiener-Khinchine theorem, this results in smaller correlation lengths. At the same time the average fluctuation amplitudes increase. Destabilizing the drift wave leads to the appearance of small and localized turbulence events. Compared to the convective cells driven by the interchange dynamics, these structures are not as efficient with respect to the density transport.

8 Summary and Conclusions

The goal of this work was to asses the possibilities of an experiment–simulation comparison of turbulence in the torsatron TJ-K and to find parameters that distinguish between different micro-instabilities. Furthermore, data analysis techniques have been developed, and experimental measurements at TJ-K have been suggested.

Simulations were carried out using the two-fluid turbulence simulation code DALF3. The two most important instabilities for the TJ-K plasma, the drift instability and the MHD interchange instability, are included in the model. The equation set is numerically solved in three-dimensional flux tube geometry. It was shown that the conditions for a successful simulation of the TJ-K plasma by DALF3 are fulfilled in a fairly large parameter space. As the normalized parameter set in TJ-K is similar to the parameters in the edge of a fusion experiment, the results from this work and the experiment–simulation comparison are of relevance for the understanding of plasma edge turbulence in fusion devices as well.

In order to identify relevant quantities and features of turbulence, results from fluid theory where revisited and important findings from previous studies where discussed. From the numerical results of the simulation it was concluded that a self-similar scaling is present in the plasma turbulence. A detailed study of the inner mechanisms of the turbulent fluctuations requires an investigation of the turbulence micro-structure. Therefore the utility of various data analysis tools was assessed with respect to their ability to discriminate the signatures of the instabilities.

- The *probability distribution function (PDF)* of the fluctuating variables showed that the fluctuations of density and potential follow a Gaussian distribution. The high kurtosis of the transport indicates that large fluctuation events are more frequent than to be expected from a standard distribution. No significant difference was observed between drift wave and MHD interchange turbulence.

- A special computation of the *cross correlation* function was introduced to analyze the spatial structure of the turbulent fluctuations. In the analysis of density fluctuations, drift waves produce almost circular vortices of small size. The interchange instability leads to large, radially elongated fluctuation events. The potential fluctuations always appeared on larger spatial scales than the density fluctuations.

- An advanced method for the detection of structures frequently used by experimentalists is *conditional averaging*. For the plasma turbulence, the results obtained from conditional averaging are consistent with those from the cross correlations.

- A quantity that is easily accessible in the experiment are *power spectra* of the fluctuations. They are similar for potential and density fluctuations. For the k spectra, self-similar scaling exponents can be observed in all situations. They are significantly stronger than the analytical predictions from fluid turbulence theory. Differences where found in the transport spectra, showing a maximum at intermediate wave numbers in drift wave turbulence and at large scales in MHD interchange turbulence.

- The *cross phase distribution* between density and potential fluctuations investigates a property which is predicted to be different by the linear models of the instabilities. It is a sensitive tool for the detection of either instability.

From the analysis of idealized cases it has been learned that the MHD interchange instability results in radially elongated density and potential fluctuations which can be described as convective cells. In the absence of parallel drift dynamics the phase shift between density and potential fluctuations attains the characteristic value of $\pi/2$ at all scales. Drift wave turbulence results in small and localized fluctuations, and the coupling between density and potential leads to a zero phase shift between the two fluctuating variables. In the power spectra, both instabilities exhibit similar scaling exponents. The complete model, including both instabilities, shows structure sizes similar to MHD interchange turbulence and has a phase shift distribution centered around zero. This is due to the fast parallel drift dynamics and parallel Alfvén waves.

Finally it was investigated what the characteristics of the TJ-K plasma would be and how they scale with plasma parameter variations. To this end, parameter scans where carried out in the local shear, the normalized plasma beta and the parallel collision frequency. It was found that the local shear of the magnetic field leads to a decrease in transport and fluctuation strength. This indicates a decorrelation of large radial structures. In the poloidal direction, a damping of the smaller structures is observed. At moderate local shear, signatures of the MHD interchange instability could be observed. This might be attributed to the modified field line curvature resulting from the shear model. It is open to further investigation whether this observation still holds in more realistic geometries.

Increasing the normalized plasma pressure $\hat{\beta}$ leads to rising signatures of the MHD interchange instability. It is mainly observed in the large scales of the turbulent fluctuations and manifested in the formation of radially elongated events. This effect is stronger on the low field side of the plasma, where the unfavorable curvature destabilizes the fluctuations. The average phase shift between density

and potential increases slightly at the largest scales. In the power spectra, significantly larger fluctuations can be observed. As the MHD interchange instability becomes more important, the transport increases. These findings are consistent with the linear picture of this instability.

The parallel collisionality enhances drift wave turbulence. This is mostly visible at the intermediate scales, where the transport fluctuations are strongest. As a result, the turbulence eddies, as observed in the cross correlations, hardly change their size. The increase in transport with rising collisionality can be attributed to both increased fluctuation amplitudes and a broadening of the phase shift distribution. As the drift instability is equally active on the high and low field side, its effects can be observed everywhere along a field line. As a result of the parameter scan, drift wave-like behavior can be expected in TJ-K.

Finally we conclude that the TJ-K plasma is in a parameter regime where it can be simulated by the DALF3 code, yielding valuable insight in the micro-structure of the turbulence. The statistical analysis of the fluctuations provides various means for a comparison of simulation and experiment. Statistical tools are suitable for the discrimination of drift wave and MHD interchange turbulence. The most sensitive diagnostics are obtained from spatially resolved measurement, using a multi probe array in the experiment. The relative importance of the micro-instabilities can be deduced best from the radial structure size, the cross phases and the transport spectra. To confirm these results and therefore the physical models used in the code, experimental measurements should be carried out to verify the numerical predictions. As the study of data analysis tools has underlined the importance of spatially resolved measurements, corresponding diagnostics should be implemented in the experiment. In TJ-K, a poloidal probe array is already available. Its measurements have to be analyzed and to be compared with the simulation results obtained during the course of the present work.

The prediction for TJ-K is drift-wave like turbulence all over the accessible parameter range. Since TJ-K is one of the few devices with full probe access to the plasma, it can provide a valuable contribution to the understanding of plasma turbulence.

A List of symbols

Variable	Section	Signification
$\mathbf{A}$, $A_\parallel$		Vector potential, parallel vector potential
E		Energy
β		Plasma beta
$\mathbf{B}$, B_0		Magnetic field
$C_u(\tau)$, $C_{uv}(\tau)$	6.3.2	Auto-/Cross correlation of variable u for delay τ
δ	3.4	Drift parameter, $\varrho_s/L_\perp$
ε, η	5.1	Energy dissipation per unit mass, vorticity flow
$\mathbf{E}$		Electric field
Γ		Radial density transport
$\mathbf{J}$, $J_\parallel$		Current, parallel current
Ω		Vorticity
n, $\tilde{n}$, n_0		Density, density fluctuation, background density
p, $\tilde{p}$		pressure, pressure fluctuation
T, T_e		Electron temperature
$L_\parallel$, $L_\perp$	3	Connection length, gradient length
M_i, m_e		Ion mass, electron mass
ν_e		Electron collision rate
ϕ, $\tilde{\phi}$		Potential, potential fluctuation
$\mathbf{k}, k_\parallel, k_\perp$	3	wave vector, wave numbers
q, ι	2.1	Safety factor, rotational transform
(x, y, z)	4.4.2	Flux tube coordinates
(ϕ, θ, ζ)	4.4.2	Hamada coordinates
(ϕ, θ, ξ)	4.4.2	Field aligned coordinates
(R, Z, Φ)	4.4.2	Cylinder coordinates
$g^{\mu\nu}$, $g_{\mu\nu}$	4.4.2	Co- and contravariant elements $\mu\nu$ of the metric tensor
$\hat{\beta}, \hat{\mu}, \hat{\nu}, \varepsilon_s$	3.4	Normalized plasma parameters
ϱ_s	3.1	Drift scale
c_s	3.4	Sound speed
v_A	3.4	Alven speed
ω_{ci}, ω_{ce}		Ion cyclotron frequency, electron cyclotron frequency
$\mathbf{v}_E$, $\mathbf{v}_*$, $\mathbf{v}_{pol.}$	3.2.1	$\mathbf{E} \times \mathbf{B}$-, diamagnetic and polarization velocity
Π_k, Ω_k	5.1	Engery flux, viscous dissipation at scale k
$S_n(l)$	5.1	Structure function of order n

Variable	Section	Signification
$\xi(t)$	6.3.1	Random variable
σ	6.3.1	Standard deviation
$\hat{s}, \hat{S}$	4.4.2	local shear, total global shear
Σ	4.4.2	total local shear
$u(x)$, $\hat{u}(k)$	6.4.1	Variable u, Fourier transform of u
$\varphi_{n,\phi}$	6.4.2	Cross phase of n and ϕ

B Denormalization of plasma parameters

This section describes how a set of experimental parameters describing the plasma (namely, electron density n_e, electron temperature T_e and magnetic field B) can be obtained from the set of normalized parameters $(\hat{\nu}, \hat{\beta}, \hat{\mu})$ used in the simulation. We will find that $\hat{\mu}$ is irrelevant for the computation of the physical parameters. It is independent from T_e, n_e and B. The normalized parameter $\hat{\nu}$ is defined as

$$\hat{\nu} = \nu_e \frac{L_\perp}{c_s} \tag{B.1}$$

$$\nu_e = 8\pi e^2 n_e c \ln\Lambda \frac{1}{3\sqrt{3m_e}T_e^{3/2}} \tag{B.2}$$

$$c_s = \sqrt{\frac{T_e}{m_i}}\,. \tag{B.3}$$

With $\nu_e[\mathrm{s}^{-1}]$ being the electron collision rate, $L_\perp[\mathrm{m}]$ is the scale length of the pressure gradient, $c_s[\mathrm{m/s}]$ the sound speed, $n_e[\mathrm{m}^{-3}]$ is the plasma density, and $T_e[\mathrm{eV}]$. The following constants are used: Electron charge $e = 1$, electron mass $m_e = 5.11 \times 10^5\,\mathrm{eV/c}^2$, ion mass $m_i = 9.38 \times 10^8\,\mathrm{eV/c}^2$ for hydrogen, the light speed $c = 2.99 \times 10^8\,\mathrm{m/s}$ and $\ln\Lambda \approx 17$ (the Coulomb logarithm). In a contracted form, $\hat{\nu}$ can be written as:

$$\hat{\nu} = \left(\frac{8\pi}{3\sqrt{3m_e m_i}}\ln\Lambda\right) n_e T_e^{-2} \tag{B.4}$$

$$\tag{B.5}$$

The normalized parameter $\hat{\beta}$ is defined as

$$\hat{\beta} = \beta_e \left(\frac{qR}{L_\perp}\right) \tag{B.6}$$

$$\beta_e = \frac{4\pi n_e T_e}{B^2}\,, \tag{B.7}$$

where (qR) is the product of rotational transform and the major radius. In a contracted form, the definitions read:

$$\hat{\beta} = \left(4\pi q^2 R^2 L_\perp^{-2}\right) n_e T_e B^{-2} \tag{B.8}$$

To close the equation set, we use the drift scale ϱ_s[m], defined as:

$$\varrho_s = \frac{c_s}{\omega_{ci}} \tag{B.9}$$

$$\omega_{ci} = \frac{qB}{m} \tag{B.10}$$

with B[Vs/m^2][T] being the magnetic field strength. Written in the contracted form,

$$\varrho_s = \frac{c}{e}\sqrt{m_i}\, T_e^{1/2} B^{-1}\,. \tag{B.11}$$

With the definition of the constants

$$C_\nu = \frac{8\pi}{3\sqrt{3m_e m_i}} \ln\Lambda \tag{B.12}$$

$$C_\beta = 2\mu_0 q^2 R^2 L_\perp^{-2} \tag{B.13}$$

$$C_\varrho = \frac{c}{e}\sqrt{m_i}\,, \tag{B.14}$$

the equations can be rewritten in the form

$$\hat{\nu} = C_\nu\, n_e T_e^{-2} \tag{B.15}$$

$$\hat{\beta} = C_\beta\, n_e T_e B^{-2} \tag{B.16}$$

$$\varrho_s = C_\varrho\, T_e^{1/2} B^{-1}\,. \tag{B.17}$$

Squaring Eq. [B.17] and dividing Eq. [B.16] by the result yields

$$\frac{\hat{\beta}}{\varrho_s^2} = \frac{C_\beta}{C_\varrho^2} n_e \tag{B.18}$$

$$n_e = C_\varrho^2\, C_\beta^{-1}\, \hat{\beta}\, \varrho_s^{-2} \tag{B.19}$$

From Eq. [B.15] we obtain an expression for T_e^2, and by inserting the result for n_e it can be reduced to contain only normalized parameters,

$$T_e^2 = \frac{C_\nu n_e}{\hat{\nu}} \tag{B.20}$$

$$= C_\nu\, C_\varrho^2\, C_\beta^{-1}\, \hat{\beta}\, \hat{\nu}^{-1}\, \varrho_s^{-2} \tag{B.21}$$

$$T_e = C_\nu^{1/2}\, C_\varrho\, C_\beta^{-1/2}\, \hat{\beta}^{1/2}\, \hat{\nu}^{-1/2}\, \varrho_s^{-1} \tag{B.22}$$

By dividing Eq. [B.16] by Eq. [B.15] and rising the result to the power of $-\frac{1}{2}$, we get

$$\left(\frac{\hat{\beta}}{\hat{\nu}}\right)^{1/2} = \left(\frac{C_\beta}{C_\nu}\right)^{1/2} T_e^{3/2}\, B^{-1} \tag{B.23}$$

$$B = C_\nu^{-1/2}\, C_\beta^{1/2}\, \hat{\beta}^{-1/2}\, \hat{\nu}^{+1/2}\, T_e^{3/2} \tag{B.24}$$

We now insert the value for T_e as it was obtained before,

$$\begin{aligned} B &= C_\nu^{-1/2}\, C_\beta^{1/2}\, \hat{\beta}^{-1/2}\, \hat{\nu}^{+1/2}\, \left(C_\nu^{1/2}\, C_\varrho\, C_\beta^{-1/2}\, \hat{\beta}^{1/2}\, \hat{\nu}^{-1/2}\, \varrho_s^{-1}\right)^{3/2} && \text{(B.25)} \\ &= C_\nu^{-1/2}\, C_\beta^{1/2}\, \hat{\beta}^{-1/2}\, \hat{\nu}^{1/2}\, \left(C_\nu^{3/4}\, C_\varrho^{3/2}\, C_\beta^{-3/4}\, \hat{\beta}^{3/4}\, \hat{\nu}^{-3/4}\, \varrho_s^{-3/2}\right) && \text{(B.26)} \\ &= C_\nu^{1/4}\, C_\varrho^{3/2}\, C_\beta^{-1/4}\, \hat{\beta}^{1/4}\, \hat{\nu}^{-1/4}\, \varrho_s^{-3/2} && \text{(B.27)} \end{aligned}$$

To summarize, we have obtained the following formulas

$$\begin{aligned} n_e &= C_\varrho^2\, C_\beta^{-1}\, \hat{\beta}\, \varrho_s^{-2} && \text{(B.28)} \\ T_e &= C_\nu^{1/2}\, C_\varrho\, C_\beta^{-1/2}\, \hat{\beta}^{1/2}\, \hat{\nu}^{-1/2}\, \varrho_s^{-1} && \text{(B.29)} \\ B &= C_\nu^{1/4}\, C_\varrho^{3/2}\, C_\beta^{-1/4}\, \hat{\beta}^{1/4}\, \hat{\nu}^{-1/4}\, \varrho_s^{-3/2} && \text{(B.30)} \end{aligned}$$

with the units as described at the beginning of this section.

Acknowledgements

Many people and organizations supported me during this work. I thank Ulrich Stroth for accepting me as an PhD student and defining the scope of the present work; in numerous discussions, he lead me towards completeteness and targeted omissions and hidden assumptions. Bruce Scott gave me the opportunity to use his excellent DALF3 simulation code, and patiently answered my questions on the model equations and the implementation. His experience and knowledge of plasma physics was of great help, and he taught me to understand the turbulence from the equations. Alexander Kendl introduced me to the geometry of the stellarator and discussed the first simulation results with me. I thank Thomas Klinger with whom I had the first contact to plasma physics during my diploma thesis. He encouraged me to a PhD thesis in that domain, a decision that I did not regret.

The Max-Planck-Institut für Plasmaphysik (IPP Garching) gave me financial support during the project, including the possibility to visit conferences and discuss my results with other scientists. The positive feedback I received there was an important source of motivation. The IPP also gave me access to the computational resources on the CRAY T3E parallel computer; without this powerful machine, the work would still be in the first steps. Many students and scientists from the Institut für Experimentelle und Angewandte Physik (CAU Kiel) listened to my ideas and discussed the concepts of the present work with me. I am also grateful to Jens-Christian Claussen from the Institut für Theoretische Physik for discussions on statistics and selfsimilarity.

This thesis would have been much harder without the software I used; so a big "thank you" to all developers of Free and Open Source Software all over the world. Latex, GNU/Linux, KDE and the internet have saved me a lot of work and let me efficiently use my computational resources.

My private life did not remain unaffected during this work, and a lot of things have changed in the last three years. I did not have much time for Anja Tolkmitt, Kim and Maj; I thank them for their understanding. It had not always been easy.

Most of all I thank my "Gegenstück" Julia Frangipani for the motivation she gave to me during the last year and for all the support during the last weeks; although our "competition" is over as I hand in this work, it is still unclear who has won.

Bibliography

[1] E. Ascasibar, C. Alejaldre, J. Alonso, F. De Aragon, R. Balbin, et al., *Initial Operation of the TJ-1U Torsatron and Theoretical Studies for the Flexible Heliac TJ-II*, Plasma Physics and Controlled Fusion Research (Proc. 15^{th} Int. Conf., Seville, 1994), IAEA, Vienna (Vienna), IAEA, 1994, p. 749.

[2] E. Ascasibar, J. Quin, A.L. Fraguas, I. Pastor, and J. Herranz, *Measurements of Magnetic Surfaces on the TJ-I U torsatron*, Nucl. Fusion **37** (1997), no. 2, 851.

[3] P. Bak, *How nature works. The science of self-organized criticality*, Copernicus/Springer-Verlag, New York, 1996.

[4] M. A. Beer and G. W. Hammet, *Toroidal gyrofluid equations for simulations of tokamak turbulence*, Phys. Plasmas **3** (1996), no. 11, 4046.

[5] J. Bleuel, *Elektrostatische Turbulenz am Plasmarand des Stellarators Wendelstein 7AS*, Dissertation, Max-Planck-Insitut für Plasmaphysik (IPP Report 3-235), Garching, 1998.

[6] J. Bleuel, M. Endler, H. Niedermeyer, M. Schubert, Thomsen H., et al., *The spatial structure of edge fluctuations in the Wendelstein 7-AS stellarator*, New J. Phys. **4** (2002), no. 38.

[7] F. H. Busse, *Convection driven zonal flows and vortices in the major planets*, Chaos **4** (1994), no. 2, 123.

[8] S. J. Camargo, B. D. Scott, and D. Biskamp, *The influence of magnetic fluctuations on collisional drift wave turbulence*, Phys. Plasmas **3** (1994), no. 11, 3912.

[9] B. A. Carreras, R. Balbin, B. van Milligen, J. Bleuel, M. Endler, A. Chankin, et al., *Characterization of teh Frequency Ranges of the Plasma Edge Fluctuation Spectra*, Phys. Plasmas **6** (1999), no. 12, 4615.

[10] B. A. Carreras, C. Hidalgo, E. Sanchez, M. A. Pedrosa, R. Balbín, I. Garcia-Cortes, B. van Milligen, D. E. Newman, and V. E. Lynch, *Fluctuation-induced flux at the plasma edge in toroidal devices*, Phys. Plasmas **83** (1999), no. 18, 3653.

[11] B. A. Carreras, B. van Milligen, B. C. Hidalgo, R. Balbin, E. Sanchez, I. Garcia-Cortes, M. A. Pedrosa, J. Bleuel, and M. Endler, *Self-Similarity Properties of the Probability Distribution Function of Turbulence-Induced Particle Fluxes at the Plasma Edge*, Phys. Rev. Lett. **83** (1999), no. 18, 3653.

[12] B. A. Carreras, B. van Milligen, D. E. Newman, E. Sanchez, J. Bleuel, et al., *Self-similarity of the plasma edge fluctuations*, Phys. Plasmas **4** (1998), no. 10, 3632.

[13] F. F. Chen, *Plasma Physics and Controlled Fusion*, Plenum Press, New York, 1984.

[14] R. L. Dewar, D. A. Monticello, and W. N.-C. Sy, *Magnetic coordinates for equilibria with continuous symmetry*, Phys. Fluids **27** (1984), no. 7, 1723.

[15] W. D. D'Haeseleer, W. N. G. Hitchon, J. D. Callen, and J. L. Shohet, *Flux coordinates and magnetic field structure*, Springer, Berlin, 1990.

[16] P. H. Diamond and T. S. Hahm, *In Search of the Elusive Zonal Flow Using Cross-Bicoherence Analysis*, Phys. Rev. Lett. **84** (2000), no. 21, 4842.

[17] A. Dimits and *et al.*, *Comparisons and physics basis of tokamak transport models and turbulence simulations*, Phys. Plasmas **7** (2000), no. 3, 969.

[18] W. Dorland and G. W. Hammett, *Gyrofluid models with kinetic effects*, Phys. Fluids B **5** (1992), no. 3, 812.

[19] M. Endler, H. Niedermeyer, L. Giannone, E. Holzhauer, A. Rudyj, et al., *Measurements and Modelling of the Electrostatic Fluctuations in the Scrape-Off Layer of ASDEX*, Nucl. Fusion **35** (1995), no. 11, 1307.

[20] U. Frisch, *Turbulence*, Cambridge University Press, New York, 1995.

[21] U. Frisch and S. A. Orzag, *Turbulence: Challenges for theory and experiment*, Physics Today (1990), no. 1, 24.

[22] X. Garbet, *Turbulence in fusion plasmas: key issues and impact on transport modelling.*, Plasma Phys. Controlled Fusion **43** (2001), A251.

[23] F. Greiner, O. Grulke, C. Lechte, U. Stroth, and A. Piel, *RF-plasma in a simple magnetised torus*, Proc. 2000 Int. Congress on Plasma Physics (Quebec City, Canada), vol. 1, APS, 2000, p. 140.

[24] O. Grulke, *Investigation of large-scale spatio-temporal fluctuation structures in magnetized plasmas*, Dissertation, Max-Planck-Institut für Plasmaphysik, Garching, 1998.

[25] P. N. Guzdar, J. F. Drake, D. McCarthy, A. B. Hassam, and C. S. Liu, *Three-dimensional fluid-simulations of the nonlinear drift-resistive ballooning modes in tokamak edge plasmas*, Phys. Fluids, B **5** (1993), no. 11, 3712.

[26] K. Hallatschek and D. Biskamp, *Transport control by coherent zonal flows in the core–edge transitional regime*, Phys. Rev. Lett. **86** (2000), no. 7, 1223.

[27] A. Hasegawa and K. Mima, *Pseudo-three-dimensional turbulence in magnetized nonuniform plasmas*, Phys. Fluids **21** (1978), no. 1, 87.

[28] A. Hasegawa and M. Wakatani, *Plasma edge turbulence*, Phys. Rev. Lett. **50** (1983), no. 9, 682.

[29] F. Jenko, *Numerische Modellierung stoßfreier Driftwellenturbulenz*, Dissertation, Max-Planck-Insitut für Plasmaphysik (IPP Report 5-82), Garching, 1998.

[30] F. Jenko, W. Dorland, M. Kotschenreuter, and B. N. Rogers, *Electron temperature driver turbulence*, Phys. Plasmas **7** (2000), no. 5, 1904.

[31] A. Kendl, *Drift wave instability and turbulence in advanced stellarator configurations*, Dissertation, Max-Planck-Insitut für Plasmaphysik (IPP Report 5-95), Garching, 2001.

[32] A. Kendl, B. D. Scott, and Wobig H., *Transition from tokamak to stellarator turbulence*, Plasma Phys. Controlled Fusion **42** (2000), L23.

[33] A. Kendl and H. Wobig, *Geometric effects on Drift Wave Stability in Advanced Stellarators*, Phys. Plasmas **6** (1999), no. 11, 4714.

[34] J. Kisslinger and H. Wobig, Europhys. Conf. Abstracts **9F** (1985), no. I, 453.

[35] R. H. Kraichnan, *Inertial Ranges in Two-Dimensional Turbulence*, Phys. Fluids **10** (1967), 1417.

[36] R. H. Kraichnan, *Turbulent cascade and intermittency growth*, Proc. R. Soc. London **A** (1991), no. 434, 65.

[37] N. Krause, C. Lechte, S. Niedner, and U. Stroth, *Low-Temperature Plasma Turbulence in the Torsatron TJ-K*, Proc. of the 27^{th} Europ. Conf. on Controlled Fusion and Plasma Physics, Budapast, The European Physical Society, 2000.

[38] N. Krause, C. Lechte, U. Stroth, S. Niedner, E. Ascasibar, and J. Alonso, *The Torsatron TJ-K, a toroidal plasma experiment for low-temperature plasma research*, Rev. Sci. Instrum. **73** (2002), 3474.

[39] J. A. Krommes and M. Ottaviani, *Long-time tails do not necessarily imply self-organized criticality or the breakdown of the standard transport paradigm*, Phys. Plasmas **6** (1999), no. 10, 3731.

[40] C. Lechte, *Dissertation*, Institut für Experimentelle und Angewandte Physik, Kiel, 2002.

[41] C. Lechte, S. Niedner, and U. Stroth, *Comparison of Turbulence Measurements and Simulations of the Low-Temperature Plasma in the Torsatron TJ-K*, New J. Phys. **4** (2002), no. 34.

[42] C. Lechte, S. Niedner, and U. Stroth, *Comparison of Turbulence Measurements and Simulations of the Low-Temperature Plasma in the Torsatron TJ-K*, New Journal of Physics (2002), accepted for publication.

[43] C. Lechte, J. Stöber, and U. Stroth, *Plasma parameter limits of magnetically confined low temperature plasmas from a combined particle and power balance*, Phys. Plasmas **9** (2002), no. 6, 2839.

[44] C. Liewer, *Measurement of Microturbulence in Tokamaks and Comparisons with Theories of Turbulence and Anomalous Transport*, Phys. Fluids **25** (1985), no. 5, 543–621.

[45] Z. Lin, T. S. Hahm, W. W. Lee, W. M. Tang, and R. B. White, *Turbulent Transport Reduction by Zonal Flow: Massively Parallel Simulations*, Nature **281** (1998), 1835.

[46] M. V. Medvedev and P. H. Diamond, *On the statistical mechanics of self-organized profiles*, Phys. Plasmas **3** (1996), no. 11, 3912.

[47] R. A. Moyer, G. R. Tynan, C. Holland, and M. J. Burinand, *Increased Nonlinear Coupling between Turbulence and Low-Frequency Fluctuations at the L-H Transition*, Phys. Rev. Lett. **87** (2001), no. 13, 135001.

[48] D. E. Newland, *An introduction to random vibrations, spectral and wavelet analysis*, Longman Singapore Publishers, Singapore, 1977.

[49] S. Niedner, C. Lechte, U. Stroth, N. Krause, B. Scott, and J. Stöber, *Experiments on turbulence in toroidal plasmas and comparison with simulations*, Proc. of the ISSS-6, Garching (Katlenburg-Lindau, Germany) (M. Scholer J. Büchner, C.T. Dumm, ed.), Copernicus Gesellschaft, 2001, p. 202.

[50] S. Niedner, B. D. Scott, and U. Stroth, *Statistical properties of drift wave turbulence in low-temperature plasmas*, Plasma Phys. Controlled Fusion **44** (2002), 397.

[51] J. Nührenberg, W. Lotz, P. Merkel, C. Nührenberg, U. Schwenn, M. Strumberger, E., et al., *Overview of Wendelstein 7-X Theory*, Proc. of the 6^{th} Int. Toki Conf. on Plasma Phys. and Contr. Nuclear Fusion, Toki, 1995, p. 71.

[52] W. H. Press, S. A. Teukolky, W. T. Vetterling, and B. P. Flannery, *Numerical recipes in FORTRAN, second edition*, Cambridge University Press, New York, 1999.

[53] B. N. Rogers, W. Dorland, and M. Kotschenreuter, *Generation and stability of zonal flows in ion-temperature-gradient mode turbulence*, Phys. Rev. Lett. **85** (2000), 5336.

[54] Y. Sarazin and Ph. Ghendrih, *Intermittent particle transport in two-dimensional edge turbulence*, Phys. Plasmas **5** (1998), no. 12, 4214.

[55] H. G. Schuster, *Deterministic Chaos. An introduction.*, VCH Verlagsgesellschaft, Weinheim, 1984.

[56] B. D. Scott, *private communication.*

[57] B. D. Scott, *Drift-Alfvén waves*, `http://www.rzg.mpg.de/~bds` (1997).

[58] B. D. Scott, *Modelling toroidal curvature in slab coordinates*, `http://www.rzg.mpg.de/~bds` (1997).

[59] B. D. Scott, *Shifted metric procedure for flux tube treatments of toroidal geometry: Avoiding grid deformation*, `http://www.rzg.mpg.de/~bds` (1997).

[60] B. D. Scott, *Three Dimensional Computation of Collisional Drift Wave Turbulence in Tokamak Geometry*, Plasma Phys. Controlled Fusion **39** (1997), 471.

[61] B. D. Scott, *Global Consistency for thin flux tube treatments of toroidal geometry*, Phys. Plasmas **5** (1998), no. 6, 2334.

[62] B. D. Scott, *Low frequency fluid drift turbulence in magnetised plasmas*, Habilitationsschrift, Max-Planck-Insitut für Plasmaphysik (IPP Report 5-92), Garching, 2000.

[63] L. Spitzer, US Atomic energy Commission Report **NYO-993** (1951), no. PM-S-1.

[64] L. Spitzer, Phys. Fluids **1** (1958), 253.

[65] U. Stroth, *A Comparative Study of Stellarator and Tokamak Transport*, Plasma Phys. Controlled Fusion **40** (1998), no. 1, 9.

[66] U. Stroth, *Einführung in die Plasmaphysik (Vorlesungsskript)*, Institut für Experimentelle und Angewandte Physik, Kiel, 2000.

[67] U. Stroth, E. Ascasibar, N. Krause, C. Lechte, N. Niedner, S. Krause, B. Scott, J. Stöber, and R. Westphal, *Low-Temperature Plasma Turbulence in the Torsatron TJ-K*, Proc. of the 28^{th} Europ. Conf. on Controlled Fusion and Plasma Physics, Funchal, no. P4.071, 2001.

[68] F. Wagner and U. Stroth, *Transport in Toroidal Devices - the Experimentalist's View*, Plasma Phys. Controlled Fusion **35** (1993), 1321.

[69] Masahiro Wakatani, *Stellarator and Heliotron Devices*, Oxford University Press, Oxford, 1998.

[70] R. E. Waltz and A. H. Boozer, *Local Shear in General Magnetic Stellarator Geometry*, Phys. Fluids, B **5** (1993), no. 7, 2201.

[71] J. Wesson, *Tokamaks*, Clarendon Press, Oxford, 1987.

[72] R. Westphal, *Flussflächenmessungen am Torsatron TJ-K, diploma thesis*, Kiel, 2001.

[73] A. Winder and C. J. Loda, *Space-time information processing*, Peninsula Publishing, Los Altos, 1981.

[74] A. J. Wooton, B. A. Carreras, H. Matsumoto, K. McGuire, W. A. Peebles, et al., *Fluctuations and Anomalous Transport in Tokamaks*, Phys. Fluids, B **2** (1990), no. 12, 2879.

[75] A. Yoshizawa, S.-I. Itoh, K. Itoh, and Y. Nobumitsu, *Turbulence Theories and Modelling of Fluids and Plasmas*, Plasma Phys. Controlled Fusion **43** (2001), R1.

[76] A. Zeiler, *Tokamak edge turbulence*, Habilitationsschrift, Max-Planck-Institut für Plasmaphysik (IPP Report 5-88), Garching, 1999.

[77] A. Zeiler, D. Biskamp, and J. F. Drake, *Three dimensional fluid simulations of tokamak edge turbulence*, Phys. Plasmas **3** (1996), no. 8, 2951.